Faculdade de Ciências e Tecnologia

Universidade de Coimbra

DEVELOPMENT OF AN OPTICAL COHERENCE TOMOGRAPHY FOR SMALL ANIMAL RETINAL IMAGING

João Miguel Guedes de Oliveira

Coimbra, September 2012

Faculdade de Ciências e Tecnologia

Universidade de Coimbra

DEVELOPMENT OF AN OPTICAL COHERENCE TOMOGRAPHY FOR SMALL ANIMAL RETINAL IMAGING

Thesis submitted for the degree of Master in Biomedical Engineering

Supervisors: Prof. Dr. António Miguel Morgado (IBILI-UC)

Prof. Dr. José Paulo Domingues (IBILI-UC)

João Miguel Guedes de Oliveira

Coimbra, September 2012

Abstract

Currently, animal models represent an important tool in biomedical research. Not only to understand the physiological processes involved in various diseases, but also for developing new instrumentation and techniques helpful in the diagnostic and treatment of those diseases.

The objective of the project is to develop an optical coherence tomography for small animal retinal imaging. The development was based on the integration of different optical and electronic components.

This report describes the equipment, tests and architecture of several optical bench setups. An OCT computer simulation was also developed.

Although at the end of this work, it was already possible to acquired OCT images, the system still requires a lot of improvement, namely the inclusion of the galvanometer mirrors and the control of the acquired data by the DAQ board.

Resumo

Actualmente, os modelos animais representam uma ferramenta importante na investigação biomédica. Não só para compreender os processos fisiológicos envolvidos em várias doenças, mas também para o desenvolvimento de novos instrumentos e técnicas úteis no diagnóstico e tratamento dessas doenças.

O objetivo do projeto é desenvolver uma tomografia de coerência óptica para imagens da retina de pequenos animais. O desenvolvimento baseou-se na integração de diversos componentes ópticos e electrónicos.

Este relatório descreve os equipamentos, testes e arquitetura de várias configurações ópticas. Também foi realizada uma simulação de OCT em computador.

Embora no final deste trabalho, já fosse possível adquirir imagens de OCT, o sistema ainda requer uma série de melhorias, como a inclusão dos espelhos galvanômetro e o controle dos dados adquiridos por placa DAQ.

Acknowledgements

First, I would like to thank my family, especially to my mother, who made possible for me to be here and always encouraged my decisions.

To my supervisors, Prof. Dr. António Miguel Morgado, Prof. Dr. José Paulo Domingues for their guidance, help and encouragement throughout this year. I also would like to mention a particular acknowledgment to Prof. Dr. Custódio Loureiro, who kindly helped us with some issues during the project, despite not being a team member.

Finally, a special thanks to all my friends for their unconditional support and enjoying life together with me.

Thank you all.

Index

Abstract III

Resumo V

Acknowledgements VII

List of Figures XI

List of Graphics XIII

List of Tables XV

Introduction 1

Chapter One 3

- 1.1 Optical Coherence Tomography 3
    - 1.1.1 Time Domain OCT 3
    - 1.1.2 Resolution 6
    - 1.1.3 Fourier Domain OCT 8
    - 1.1.4 Sources for OCT 10
    - 1.1.5 Scanning Modes 12
    - 1.1.6 Image Distortions 13
    - 1.1.7 Time Domain versus Fourier Domain 14
- 1.2 Other Techniques Based on OCT 18
    - 1.2.1 Full-Field OCT 18
    - 1.2.2 Doppler OCT 19
    - 1.2.3 Polarization sensitive OCT 20

Chapter Two 23

- 2.1 State of the art 23

Chapter Three 29

- 3.1 Simulation 29

Chapter Four 35

- 4.1 OCT Setup 35
    - *4.1.1 Axsun* Swept Source 37
    - *4.1.2 Thorlabs* Balanced Detector 38
    - 4.1.3 *Innovative Integration* DAQ Board 40
    - *4.1.4 Thorlabs* Interferometer 41
    - *4.1.5 Thorlabs* OCT Lenses, Gold Mirror and Collimator 43

4.2 Thorlabs Scanning System 44
Chapter Five 47
5.1 Results and Discussion 47
5.1.1 Equipment tests and acquired signals........ 47
5.1.2 Galvo System tests 55
Chapter Six........ 59
6.1 Future Work 59
6.1.1 Instrument Optimization........ 59
6.1.2 Acquisition board programming and data processing 59
References........ 63
Appendix A 69
Appendix B 83
Appendix C 85

List of Figures

FIGURE 1 – MICHELSON INTERFEROMETER 5
FIGURE 2 – INTERFERENCE PATTERN FOR LONG AND SHORT COHERENCE LENGTH 6
FIGURE 3 – RELATION BETWEEN INTERFERENCE PEAK AND COHERENT LENGTH 6
FIGURE 4 – COMPARISON OF RESOLUTION AND PENETRATION DEPTH OF OCT AND OTHER IMAGING TECHNIQUES 7
FIGURE 5 – FREQUENCY DOMAIN OCT SCHEMATICS 8
FIGURE 6 – RELATION BETWEEN WAVELENGTH AND ABSORPTION COEFFICIENT FOR DIFFERENT BIOLOGICAL TISSUES 11
FIGURE 7 – DIAGRAM OF DIFFERENT OCT SCAN TYPES 13
FIGURE 8 – DIAGRAM OF FAN DISTORTION 14
FIGURE 9 – SCHEMATICS OF WIDE FIELD OCT AND FULL FIELD OCT 19
FIGURE 10 – DIAGRAM OF DOPPLER OCT SAMPLE ARM 20
FIGURE 11 – SCHEMATICS OF POLARIZATION SENSITIVE OCT 21
FIGURE 12 – RETINAL LAYERS 24
FIGURE 13 – BENCH CONFIGURATION OF OUR OCT SYSTEM 35
FIGURE 14 – FINAL OCT DIAGRAM 36
FIGURE 15 – WARNING LABEL FOR CLASS 1M LASER 37
FIGURE 16 – *AXSUN* SWEPT SOURCE OCT BENCH VERSION 38
FIGURE 17 – FRONT AND REAR PANELS OF *AXSUN* SOURCE. 38
FIGURE 18 – *THORLABS* BALANCED DETECTOR 39
FIGURE 19 – FUNCTIONAL BLOCK DIAGRAM OF BALANCED DETECTOR 40
FIGURE 20 – *INNOVATIVE INTEGRATION* DAQ BOARD 40
FIGURE 21 – X5-400M BLOCK DIAGRAM 41
FIGURE 22 – *THORLABS* INT-MZI INTERFEROMETER 42
FIGURE 23 – FUNCTIONAL DIAGRAM OF THE MZI 1050 INTERFEROMETER 42
FIGURE 24 – *THORLABS* GALVO SYSTEM 45
FIGURE 25 – SERVO BOARD DIAGRAM 46
FIGURE 26 – J7- COMMAND INPUT CONNECTOR PIN- CONNECTION DIAGRAM 46
FIGURE 27 – DIAGRAM OF REFERENCE AND SAMPLE ARMS 50
FIGURE 28 – *AXSUN* CLOCK SIGNAL AT THE END OF THE PERIOD 52
FIGURE 29 – *AXSUN* CLOCK SIGNAL WHERE THE LASER IS TURNED ON 53
FIGURE 30 – *AXSUN* CLOCK SIGNAL WHERE THE LASER IS TURNED OFF 53
FIGURE 31 – DETAILED OF THE SCANNING LINE IN THE Y DIRECTION 55
FIGURE 32 – SCANNING LINE FOR AN AMPLITUDE OF 10 V 56
FIGURE 33 – SCANNING LINE FOR AN AMPLITUDE OF 5 V 56
FIGURE 34 – GALVO SYSTEM SCHEMATICS 57
FIGURE 35 – ACQUISITION CYCLE OF DAQ BOARD 60
FIGURE 36 – FINAL OCT CONFIGURATION 61
FIGURE 37 – SERVO BOARD 73
FIGURE 38 – X5-400M MODULE 78
FIGURE 39 – HOST BOARD 78
FIGURE 40 – 2X2 COUPLER SCHEMATIC 79
FIGURE 41 – CABLE CONSTRUCTION AND CONNECTOR FINISH 82

List of Graphics

GRAPHIC 1 – RELATION BETWEEN LATERAL RESOLUTION AND DEPTH OF FIELD 8
GRAPHIC 2 –THE SPECTRAL INTENSITY DETECTED IN FD-OCT AND THE CORRESPONDING FFT. 9
GRAPHIC 3 – SIMULATED SPECTRUM OF GAUSSIAN SOURCE 29
GRAPHIC 4 – SIMULATED TIME DOMAIN INTERFEROGRAM OF SAMPLE 1 30
GRAPHIC 5 – SIMULATED SPECTRAL INTENSITY (FD-OCT) SIGNAL OF SAMPLE 1 31
GRAPHIC 6 – FOURIER TRANSFORM OF SPECTRAL INTENSITY 31
GRAPHIC 7 – SIMULATED TIME DOMAIN INTERFEROGRAM OF SAMPLE 2, USING A SOURCE WITH CENTER WAVELENGTH AT 800 NM AND A LINEWIDTH OF 50 NM 32
GRAPHIC 8 – SIMULATED TIME DOMAIN INTERFEROGRAM OF SAMPLE 2, USING A SOURCE WITH CENTER WAVELENGTH AT 400 NM AND A LINEWIDTH OF 50 NM 32
GRAPHIC 9 – SIMULATED TIME DOMAIN INTERFEROGRAM OF SAMPLE 2, USING A SOURCE WITH CENTER WAVELENGTH AT 800 NM AND A LINEWIDTH OF 150 NM 33
GRAPHIC 10 – MIRROR REFLECTANCE FOR DIFFERENT WAVELENGTHS 44
GRAPHIC 11 – ACQUIRED *AXSUN* CLOCK SIGNAL, USING DAQ BOARD 47
GRAPHIC 12 – ACQUIRED *AXSUN* TRIGGER SIGNAL, USING DAQ BOARD 48
GRAPHIC 13 – ACQUIRED POWER OUTPUT SIGNAL FROM MZI INTERFEROMETER, USING DAQ BOARD 48
GRAPHIC 14 – ACQUIRED MZI OUTPUT SIGNAL, USING DAQ BOARD 48
GRAPHIC 15 – ACQUIRED REFLECTANCE SIGNAL FROM REFERENCE ARM, USING DAQ BOARD 49
GRAPHIC 16 – ACQUIRED REFLECTANCE FROM REFERENCE ARM AND POWER OUTPUT FROM MZI INTERFEROMETER SIGNALS, USING DAQ BOARD 49
GRAPHIC 17 – ACQUIRED SIGNAL 1 FROM REFLECTANCE OF BOTH, REFERENCE AND SAMPLE, MIRRORS, USING DAQ BOARD 50
GRAPHIC 18 – ACQUIRED SIGNAL 2 FROM REFLECTANCE OF BOTH, REFERENCE AND SAMPLE, MIRRORS, USING DAQ BOARD 50
GRAPHIC 19 – ACQUIRED A-SCAN OF THE SPECTRALIS TARGET, USING DAQ BARD, AND ITS CORRESPONDING DEPTH PROFILE 51
GRAPHIC 20 - THREE INTERFEROGRAMS FOR DIFFERENT POSITION WITHIN THE TARGET ACQUIRED USING DAQ BOARD. 51
GRAPHIC 21 – ACQUIRED *AXSUN* CLOCK SIGNAL AND INTERFERENCE SIGNAL, USING DAQ BOARD 52
GRAPHIC 22 – B-SCAN OBTAINED USING THE SPECTRALIS TEST TARGET 54
GRAPHIC 23 – SINUSOIDAL AND SQUARE WAVES 55
GRAPHIC 24 – POWER SPECTRUM OF THE ENGINE 70
GRAPHIC 25 – CLOCK OUTPUT SIGNAL 70
GRAPHIC 26 - TRIGGER OUTPUT SIGNAL 70
GRAPHIC 27 – OPTICAL POWER SIGNAL 70
GRAPHIC 28 – DETECTOR RESPONSITIVITY 72
GRAPHIC 29 – DETECTOR FREQUENCY RESPONSE 72
GRAPHIC 30 – DETECTOR SPECTRAL NOISE 72
GRAPHIC 31 – REFLECTANCE OF DISPERSION COMPENSATORS 81

List of Tables

TABLE 1 – CHARACTERISTICS OF OCT LOW COHERENCE LIGHT SOURCES 12
TABLE 2 – SAMPLE 1 PROPERTIES 30
TABLE 3 – SAMPLE 2 PROPERTIES. 31
TABLE 4 – LENSES FEATURES 43
TABLE 5 – COLLIMATOR FEATURES 44
TABLE 6 – SCANNING RANGE 57
TABLE 7 - *AXSUN* ENGINE FEATURES: 69
TABLE 8 – PDB145C PARAMETERS 71
TABLE 9 – GVS002 SPECIFICATIONS 75
TABLE 10 – INTERFEROMETER SPECIFICATIONS 76
TABLE 11 – A/D AND D/A CONVERTER FEATURES 77
TABLE 12 – COUPLERS FEATURES 79
TABLE 13 – MIRROR SPECIFICATIONS 80
TABLE 14 – DISPERSION COMPENSATORS FEATURES 81
TABLE 15 – FIBER OPTIC PATCH CORD PARAMETERS 82

Introduction

Optical Coherence Tomography (OCT) is a widely used imaging technique in medicine, mostly in ophthalmology. In biomedical research small animals are often used in order to develop, validate, or test new techniques. Imaging animals also offers the means to understand physiology, pathology, and phenotypes in an intact living system, similar to human beings.

The objective of our project is to develop a Swept Source OCT (SS-OCT) for retinal imaging in small animals. This will be a fundamental tool for research on retinal physiology and for the improvement of new instrumentation and methods for OCT based morphological and functional retinal images.

It was decided to assemble the overall system from separate blocks, including the electronics, a light source, several optical components, a detector and a data acquisition board. Thereby, instead of spending a large amount of money acquiring an available OCT system, we can save some resources and also get a better understanding on the technologies and on the difficulties and limitations involved in developing a complex system like this.

Axsun

- AXP50125-3 1060 nm – Swept Source Engine in enclosure

Thorlabs

- INT-MZI-1050 – Interferometer
- PDB145C – Fixed Gain Balance Detector, InGaAs, 800-1700 nm
- FC1064-50B-APC – 2x2 SM Coupler, 1064 nm, 50:50 Split, FC/APC
- FC1064-90B-APC – 2x2 SM Coupler, 1064 nm, 90:10 Split, FC/APC
- GVSM002/M - 2D – Galvo System
- LSM02 BB and LSM03 BB – OCT Scan Lenses
- LSM02 DC and LSM03 DC - Dispersion Compensators
- PF10-03-M01 – Protected Gold Mirror

Innovative Integration

- X5-400M – Acquisition Module

OZ Optics

- SMJ-3A3A-1060 -3.6/125-3-2 – Fiber Optic

Our project was developed in IBILI and the research team was composed by João Miguel Guedes de Oliveira master degree student, Prof. Dr. António Miguel Morgado and Prof. Dr. José Paulo Domingues, both supervisors and assistant professors from Physics Department of University of Coimbra. Prof. Dr. Custódio Loureiro also from Physics Department gave a great help in simulating the OCT signal, mostly on Fourier Transforms.

Chapter One

1.1 Optical Coherence Tomography

Nowadays, there are a great number of techniques for medical imaging. With recent advances and research on new materials and signal processing, it is expected that more, better and cheaper imaging systems will appear in the next years.

For each clinical situation, professionals have to choose between these techniques, according to the desired information, either anatomical or functional. In most cases, only with a combination of two or more techniques it is possible to assess the required information. Indeed it has to be a wise decision, because each equipment as its own risks and complications.

Optical Coherence Tomography (OCT) is a recent imaging method based on an optical interferometer of low coherence, which produces images similar to ultrasound. However it uses a light source, instead of mechanical waves. Due to the high value of speed of the light it is impossible to measure directly, with an adequate resolution, the time of flight. So, to obtain the depth information it is necessary to use an interferometric technique.

Thereby, it uses non ionizing radiation, is non invasive and the acquisition time is reduced comparing with other imaging techniques. Another advantage is the higher resolution, sub micrometer, compared to other devices. It collects cross sectional bidimensional or tridimensional images, as well as depth profile of heterogenic materials, such as biological tissues.

Currently, OCT can be applied in a large variety of fields, like material analysis for studying mechanical defects and properties; art conservation. In medicine it has been used for diagnostic, mostly in ophthalmology, but in recent years some studies demonstrate that it is also useful in dermatology, dentistry and cardiology.

1.1.1 Time Domain OCT

Electromagnetic radiation is a form of energy, which travels through waves, with both electric and magnetic fields. Waves are characterized by their frequency, amplitude, velocity and phase.

The interference phenomenon occurs when two or more waves combine. The interference pattern can be constructive, if the relative phase between superimposed waves is multiple of 2π. Otherwise, if they are shifted by a factor of π, 3π, 5π, etc. the interference is destructive. In case of phase differences within these extremes, the emergent wave magnitude is a combination of the initial waves.

For example, two waves defined, in function of time and space, by:

$$E_1(t,x) = A_1 sen(\omega t - kx + \varepsilon) \qquad E_2(t,x) = A_2 sen(\omega t - kx + \varepsilon)$$

with A the wave amplitude; ω waves' angular frequency; k the wavenumber; and ε the phase in origin

If they have the same angular frequency and velocity, but different phase in origin:

$$\theta = wt - kx$$

$$E_1 = A_1 sen(\theta + \varepsilon) \qquad E_2 = A_2 sen(\theta)$$

From trigonometry if $\varepsilon = 0{,}2\pi$ ...

$$sen(\theta + \varepsilon) = sen(\theta)$$

Otherwise, if $\varepsilon = \pi, 3\pi$ ...

$$sen(\theta + \varepsilon) = -sen(\theta)$$

Therefore, combine the two waves for both situation, we get:

$$E = A_1 sen(\theta) + A_2 sen(\theta) = (A_1 + A_2) sen(\theta)$$

$$E = A_1 sen(\theta + \pi) + A_2 sen(\theta) = (A_1 - A_2) sen(\theta)$$

There are different types of interferometers employed in OCT, such as Michelson, Mach-Zehnder, Fizeau. Michelson is the one most frequently used. Figure 1 shows a simple diagram of the interferometer operation.

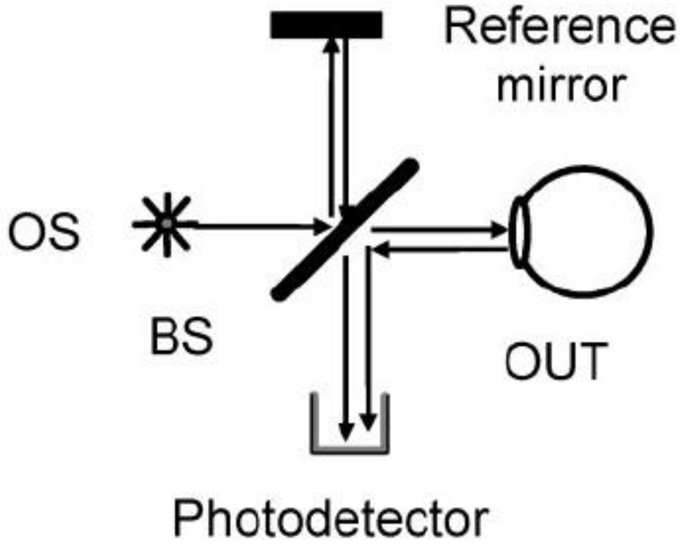

Figure 1 – Michelson Interferometer. Reproduced from **[1]**

A light source (OS) illuminates a beam splitter (BS) and the new beams travel along a reference and a sample arm. A mirror is placed at the end of the reference arm, while the sample is located on the other one. After reflection, the two beams recombine and interfere in the beam splitter. Thus the resulting output measured at a photodetector, is given by [**1**]:

$$I_{ph} = \alpha \frac{P_0}{2}\left[O + R + 2\sqrt{OR}\prod \cos\left(\frac{2\pi}{\lambda}d\right)\right]$$

where α is the photodetector responsivity; P_0 is the incident power on the object; O and R are target and reference reflectance, respectively; λ is the central wavelength of the source; d is the optical path difference between both arms; Π correlation degree among the two waves. The first terms describe the noise component and are constants, while the last one is responsible for the interference pattern.

The light source applied on interferometers performs an important role, mainly through its coherence length (l_c) which is the distance from the source to the point where the wave maintains a certain degree of correlation. For example a monochromatic light, like an ideal laser, has an infinite coherence length. Consequently, its interference profile is a continuous sinusoidal (Figure 2-a), thus it is impractical to make any depth measure using this method.

However if the source spectrum is not monochromatic, in other words if the source has a large bandwidth, by controlling the optical path difference (OPD) to be within the coherence length of source, interference will occur and has a shape similar to Figure 2-b. Therefore, by scanning the mirror position we can obtain the interference depth and reconstruct sample's structure. In short, the path difference between both arms and the light sources are the key to ensure a suitable interference [**2**][**3**].

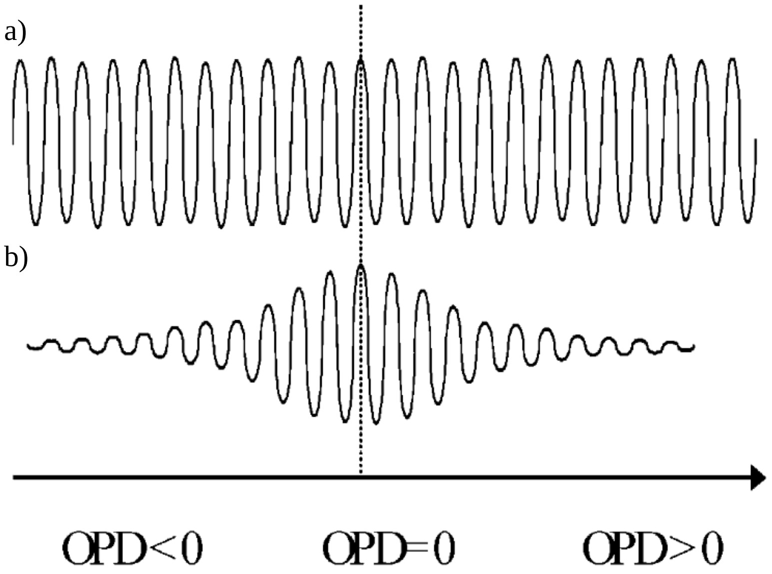

Figure 2 – Interference pattern for long (a) and short (b) coherence length, according to optical path difference. Reproduced from [1]

1.1.2 Resolution

In Figure 3 it is clear that interference peaks' width is strictly related to coherence length, so the axial OCT resolution (R_{OCT}) is half of coherence length, because of the beams trajectory.

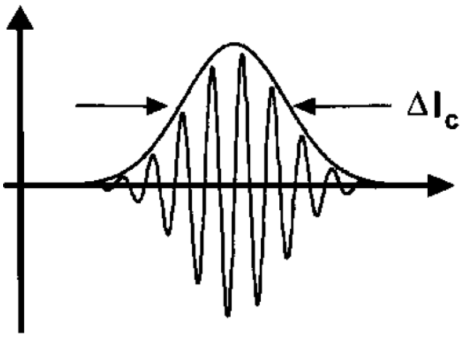

Figure 3 – Relation between interference peak and coherent length. Reproduced from [3]

$$l_c = \frac{4\ln 2}{\pi}\frac{\lambda_0^2}{\Delta\lambda}$$

$$R_{OCT} = \frac{2\ln 2}{\pi}\frac{\lambda_0^2}{\Delta\lambda}$$

For this reason and because that in OCT applications it is important to measure biological structures with micrometer dimensions, low coherence light sources are commonly employed. Figure 4 shows spatial resolutions and penetration depth for typical imaging techniques.

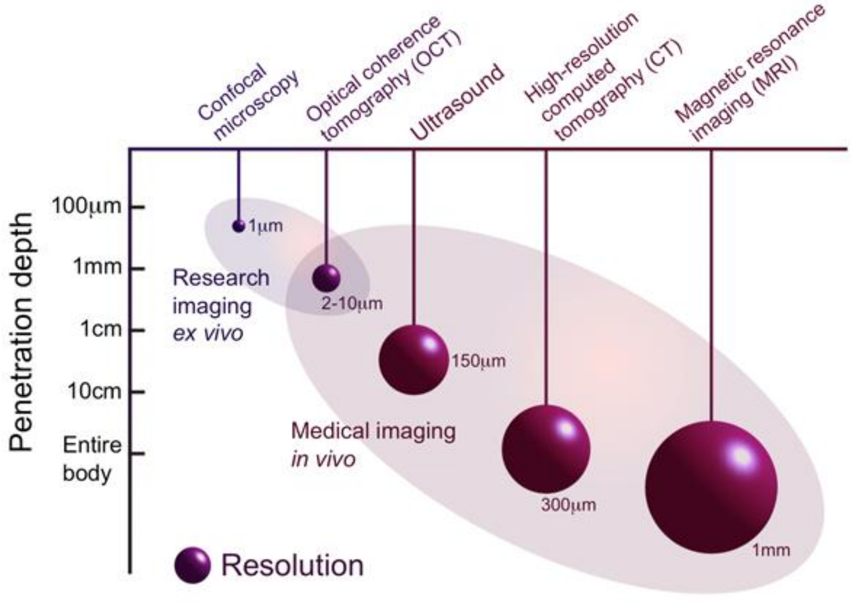

Figure 4 – Comparison of resolution and penetration depth of OCT and other imaging techniques. Reproduced from **[**54**]**

Furthermore, when comparing with other optic systems, like microscopy, axial and lateral resolution are independent. While the axial resolution is associated to coherence length, the lateral resolution only depends on the focusing properties of the OCT objective lens. Therefore, high axial and transversal resolution can be achieved.

According to Abbé, Born and Wolf, as mention in [**4**], improving transversal resolution compromises depth of field (Graphic 1), because both related to the objectives' numerical aperture (NA). Thus there is compromise between lateral resolution (L_{OCT}) and depth of field (DOF). An ideal OCT would have good lateral resolution and depth of field, but since it is impossible the optical system has to be optimized [**4**][**5**][**6**].

$$L_{OCT} = 1.22\frac{\lambda}{2NA_{obj}} \qquad\qquad DOF = 2\frac{\lambda n}{NA_{obj}^2}$$

After some algebric manipulation:

$$L_{OCT} = 1.22\frac{NA_{obj}}{4n}DOF$$

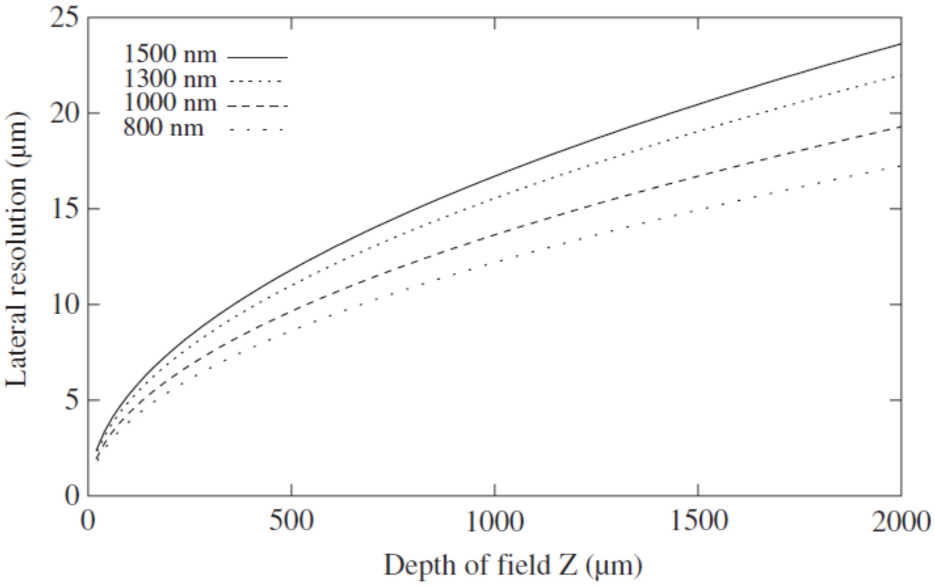

Graphic 1 – Relation between lateral resolution and depth of field, for different central wavelengths. Reproduced from **[4]**

1.1.3 Fourier Domain OCT

Frequency Domain Optical Coherence Tomography (FD-OCT),represented in Figure 5, is based on the same interferometry principles, only differing in the depth scanning process. Unlike Time Domain OCT, where the output beam is measured with the help of a photodetector, in FD-OCT the detection system is replaced by a spectrometer.

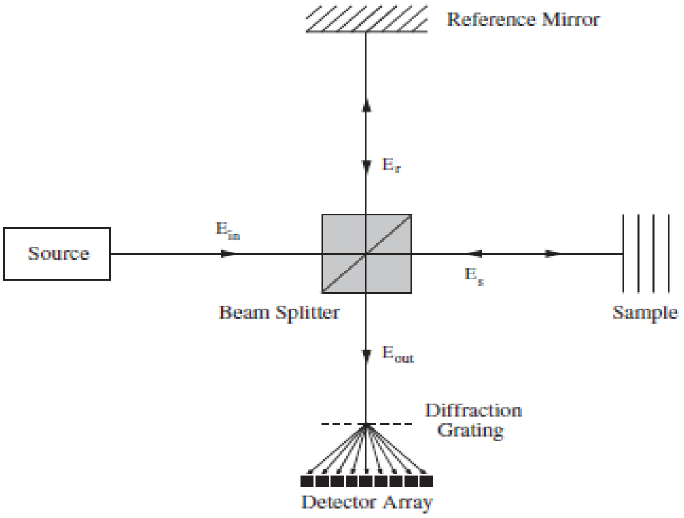

Figure 5 – Frequency Domain OCT schematics Reproduced from **[4]**

After the beam splitter, the beam passes through a dispersive element, such as a diffraction grating, and the light is decomposed on its fundamental wavelengths. The detector comprises an array of photodiodes which measures the intensity at each wavelength.

The general OCT signal is given by:

$$I(\omega, \Delta z) = T_r T_s S(\omega)|H(\omega)|^2 + T_r T_s S(\omega) + T_r T_s \Re\left(S(\omega)H(\omega)e^{-i\phi(\Delta z)}\right)$$

with T_r and T_s the transmission on beam splitter to the reference and sample arm; S (ω) and H (ω) the source intensity spectrum and samples' frequency response; and $\phi(\Delta z)$ the phase accumulation on moving the mirror [**4**].

In FD-OCT the mirror is stationary, thus the exponential term equals one $(\Delta z = 0)$. Considering an ideal beam splitter (T_r=T_s=0.5), we get:

$$I(\omega) = \frac{1}{4} S(\omega\{H(\omega) + 1\}^2)$$

After analyzing this equation it becomes clear that the samples function can be easily de-convolved dividing the output signal by the spectrum of the source The depth profile of the sample is achieved after applying a Fourier Transform which transforms signal from the frequency into the time domain and some scaling. Graphic 2 shows the detected spectrum and the corresponding Fast Fourier transform (FFT), where it is visible the interference within the sample [**4**].

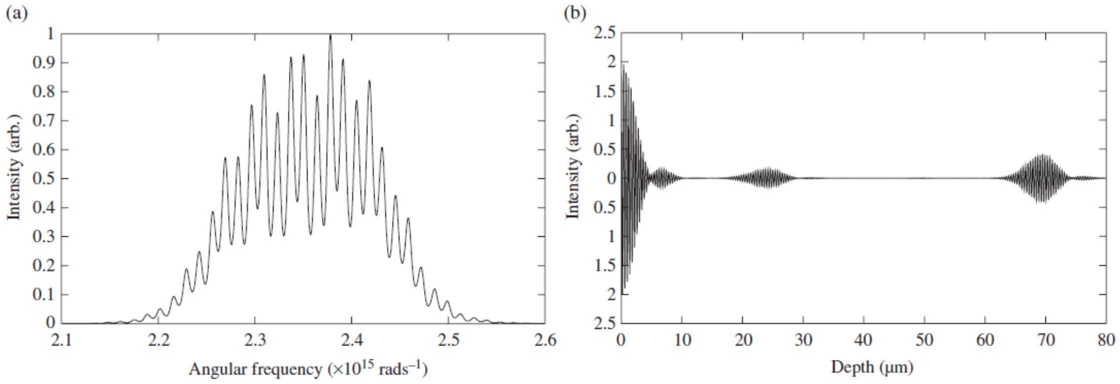

Graphic 2 –The spectral intensity detected in FD-OCT (a) and the corresponding FFT (b), clearly shows the interference peaks at sample's layers. Reproduced from **[4]**.

The measured signal is composed by N discrete points corresponding to the intensity detected by the N photodiodes of the detector array. Therefore, using the Fourier Transform properties, the maximum possible depth on FD-OCT is [**4**]:

$$z_{max} = \frac{1}{4n_{ave}} \frac{\lambda_0^2}{\Delta\lambda} N$$

where n_{ave} is the average refractive index of sample; $\lambda_0$and $\Delta\lambda$ the center wavelength and bandwidth of source, respectively. So it is clear that maximum depth increases with the number of photodiodes.

In Fourier Domain it is also possible to use a single photodetector instead of a spectrometer, but in this case it is necessary to scan independently the entire source frequencies. This is called Swept Source OCT (SS-OCT). The sweep can be extremely fast, and the output signal is equivalent to the FD-OCT

1.1.4 Sources for OCT

Light sources play an important role on OCT properties, such as axial resolution and sensitivity, and therefore must be chosen carefully.

Undoubtedly, light power is the characteristic that most affects the signal. However, high power sources increase noise levels without providing better sensitivity and in most applications, like ophthalmology, the samples do not tolerate high beam power [**7**].

The absorption on materials depends on the source wavelength. In Figure 6 are represented the absorption coefficient of some biological molecules according to the wavelength. Typically, using radiation between 600-1300nm, soft tissues have absorption coefficients within 0,1-1 mm. Although biological tissues are heterogeneous, typically the depth penetration increases with the wavelength. The red end of the visible spectrum and the Near Infra-Red (NIR) represents the therapeutic window, in spite of the increased light absorption by water on those longer wavelengths [**7**].

As already seen, the source bandwidth is the variable which most affects OCT resolution. A laser source has a very small bandwidth, in the range of 0,01nm. On the other side a tungsten bulb could reach a 300 nm bandwidth. We could consider that tungsten bulbs are adequate for use in OCT applications, but it is extremely difficult to confine the lamp emission into an optical fiber [**1**].

For this reason, Light Emitting Diodes (LED) and Super Luminescent Diodes (SLD) have been used as source devices. Modern OCT equipments already use Kerrlens mode-locked lasers and photonics crystal fibers to achieve submicron coherence length. Table 1 resumes some of the light sources used in OCT [**1**][**7**].

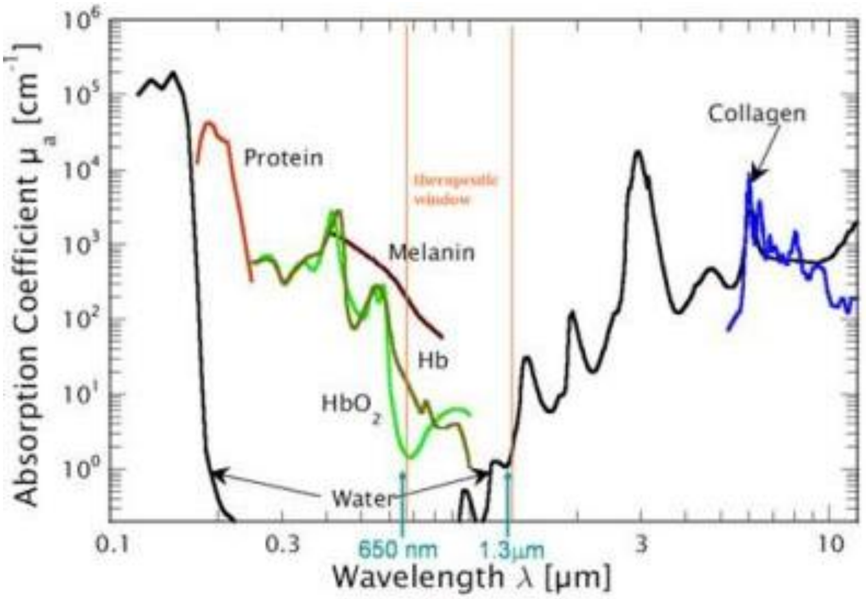

Figure 6 – Relation between wavelength and absorption coefficient for different biological tissues. Reproduced from **[**55**]**

Table 1 – Characteristics of OCT low coherence light sources. Reproduced from **[7]**

Light Sources	λ_0 (nm)*	$\Delta\lambda$ nm	l_c (µm)	Coherent Power (mW)*
SLD				
	675	10	20	40
	820	20	15	50
	820	50	6	6
	930	70	6	30
	1300	35	21	10
	1550	70	15	5
Kerr Lens				
Ti:Sapphite laser	*0,81 µm	260	1,5	400
Cr:forsterite	1280	120	6	100
LED				
	1240	40	17	0,1
	1300			
ASE fiber sources				
	1300	40	19	60
	1550	80	13	40
Superfluorescence				
Yb-doped	1064	30	17	40
Er-doped	1550	80-100	16	100
Tm-doped	1800	80	18	7
Photonic crystal fiber				
	*1,3 µm	370	2,5	6
	725	370	0,75	
Thermal Tungsten Halogen				
	880	320	1,1	*0,2 µm

1.1.5 Scanning Modes

Depending on the direction and how the scanners handle the backreflected light, different information is obtained.

A depth profile (A-scan) is performed by doing a single axial scan that detects changes on the refractive index of structures. Since there is only information from one direction, data is visualized in a plot (Amplitude vs Depth).

The common method of scanning is to simply acquire successive A-scans, by shifting the laser beam incident position longitudinally on the sample (B-scan).

However, transverse images could be useful for visualization or comparison of a specific structure with other imaging techniques. Here the sample is scanned perpendicularly to the optical axis for a specific depth (T-scan). T-scans could generate either B-scan or C-scan (En-face OCT), by changing the depth after each scan or by changing the y-scanner position after the scan for a fixed depth. Figure 7 clarifies the scanning modes employed in OCT [**1**][**8**][**9**]

For both scanning architectures two-dimensional cross-sectional in grey or false color scale images are obtained. Volume scans, which are composed by consecutive images, can be obtained using any of the techniques described before [**1**][**3**].

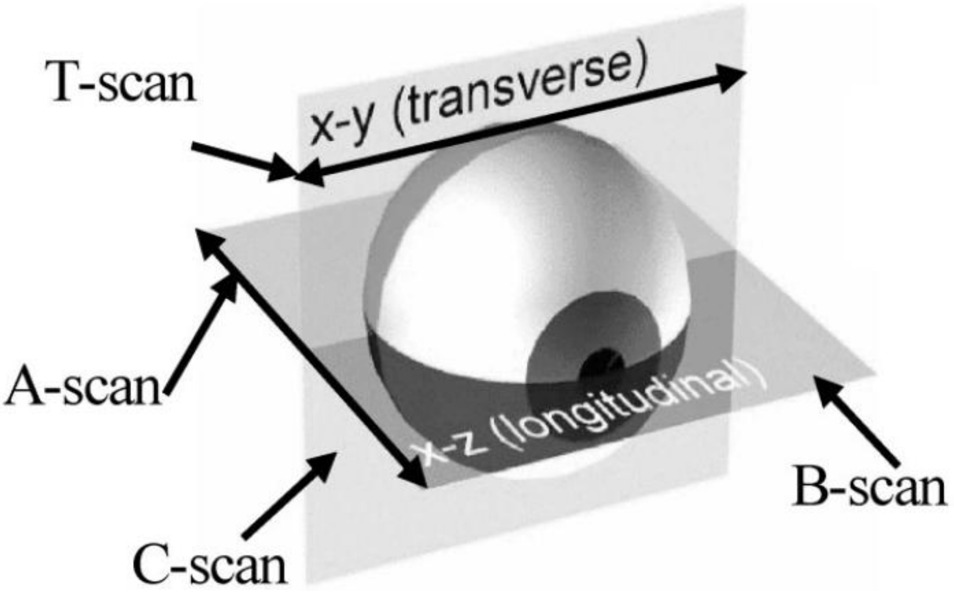

Figure 7 – Diagram of different OCT scan types. A-scan is an axial scan, B-scan is an axial image, T-scan is a transversal scan and C-scan is transversal image. Reproduced from **[**1**]**

1.1.6 Image Distortions

OCT has the potential to become vital for biometry and topography of ocular surfaces, due to its significant advantages over conventional imaging techniques, such as resolution and acquisition speed. However, there are issues regarding image distortions which limit its applications.

Fan distortion, Figure 8, is related to the scanners architecture, which is commonly implemented by two mirrors mounted in different axes. It generates field distortion and astigmatism. If the main ray is not perfectly aligned with the mirror's optical axis, then the first surface it is not well reproduced and even a linear surface becomes curve. Other contributions result from the space between both mirrors and its surface [**9**][**10**].

Optical distortion leads to significant degradation of geometrical parameters of the sample under analysis, like curvature and thickness. It occurs when imaging in a medium different from vacuum (air), due to the refractive indices of diverse layers [**10**].

Therefore, when imaging inner structures of the eye, both distortions are present as each layer has its unique opical properties. These effects can be minimized by a proper calibration of the scanning system and by processing the signal using numerical models and algorithms based on ray propagation [**10**][**11**].

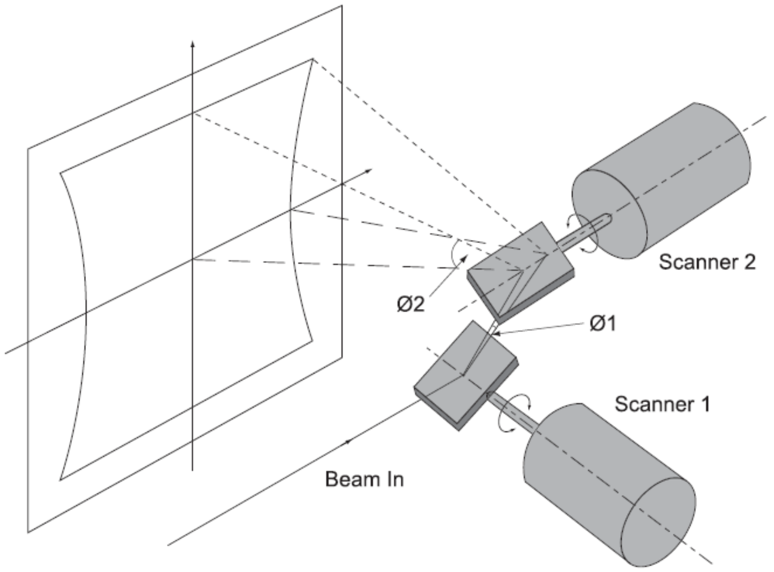

Figure 8 – Diagram of fan distortion produced by the scanning mirrors. $\boldsymbol{\theta 1}$ and $\boldsymbol{\theta 2}$ are the angle between the main ray and the mirror’s optical axis. Reproduced from [**57**]

1.1.7 Time Domain versus Fourier Domain

Although both time and frequency domain OCTs are based in the same interferometric principle, the distinct detection methods yield significant differences on the detected signal.

In contrast to time domain, where it is necessary to perform a depth sweep in order to obtain each axial scan, in frequency domain the reflectance from the entire sample’s structure is obtained simultaneously with a single exposure. As there are no moving parts, the acquisition speed and sensitivity of frequency domain are very high compared to time domain OCT. The improvement on speed acquisition leads to a superior image density which is a desired feature on OCT applications [**12**].

One important issue concerning OCT images, commonly ophthalmologic, is the motion artifacts induced by eye movements, which might cause image distortion or blurring effects, decreasing the image quality. This problem can be negligible when acquiring an A-scan, but not for generating images (B- or C-scans) which require consistency on successive scans. Once more, the frequency domain can smooth this problem, due to higher acquisition time allowing the capture of images faster than the sample motions[**12**][**13**].

In theory, a SS-OCT allows imaging speeds 10 times faster than a FD-OCT which in turn are 400 times faster than TD-OCT. However this advantage in frequency domain, it is limited by the CCD frame rate in FD-OCT and by the tuning speed of the light source in SS-OCT. The higher price of this technology is also a limitation [**12**].

Although frequency domain is a superior tool regarding image quality it also has some disadvantages. For example, in FD-OCT there is a drop-off in sensitivity and dynamic range with increasing depth. This may occur due to the finite wavelength resolution of the detector, crosstalk between pixels and rescaling errors during signal processing. In Swept Source OCT, the SNR decrease is almost undetectable because the bandwidth for each wavelength is very small [**12**] [**13**].

Another problem is the “mirror image”. The OCT signal is a complex function, but conventional detectors only measure the real part of it (square law). Therefore there is a loss of phase information and the detector cannot distinguish between positive and negative delays. This complex deterioration can be overcome using a 3x3 coupler or an electro-optic phase modulator [**12**][**13**][**14**].

Finally, the Fourier Transform, necessary to get the sample’s structure, also reduces the number of axial pixels in the image by a factor of two[**12**].

1.1.4.1 Signal to noise ratio

Even in the signal-to-noise ratio (SNR), which is an important parameter to measure the sensitivity of equipments, there are differences between TD-OCT and Fourier domain OCT. Once more Fourier domain OCT is better than time domain, typically with a sensitivity advantage of 20-30 dB [**15**].

The detector output signal given by [**16**]:

$$S_{signal} = \frac{2\eta^2 e^2 \lambda^2}{(hc)^2} P_{ref} P_{sample}$$

With η being the detector quantum efficiency; e is the electron charge; hc/λ is the photon energy, h is Planck's constant, λ photon's wavelength and c is the speed of light. Considering that the reference spectral density is equal to source spectral density (S (ω)), while sample's is attenuated by a factor of α, the reference and sample radiant power are given by:

$$P_{ref} = \int S(\omega)\partial\omega \qquad\qquad P_{sample} = \alpha \int S(\omega)\partial\omega$$

Therefore the TD-OCT signal can be rewritten as:

$$S_{signal} = \frac{2\eta^2 e^2 \lambda^2 \alpha}{(hc)^2}\left[\int S(\omega)\partial\omega\right]^2$$

In the OCT signal there are, mainly, three sources of noise. Below we find the general equation for noise [**4**][**16**]:

$$N_{noise} \propto i_{noise}^2 = i_{thermal}^2 + i_{shot}^2 + i_{optical}^2$$

$$N_{noise} = \left(\sqrt{\frac{4kTBW}{R_{fb}}}\right)^2 + \left(\sqrt{2ei_{dc}BW}\right)^2 + \left(i_{dc}\sqrt{\frac{BW}{2\pi\Delta\omega}}\right)^2$$

i_{dc} corresponds to the dc current, from the reference arm power; and $\Delta\omega$ is the source bandwidth; they are given by:

$$i_{dc} = \frac{\eta e\lambda P_{ref}}{hc} \qquad\qquad \Delta\omega = \frac{1}{\tau_{coh}}$$

The final noise equation is given by:

$$N_{noise} = \frac{4kT}{R_{fb}} BW + \frac{2\eta e^2 \lambda P_{ref}}{hc} BW + \left(\frac{\eta e \lambda P_{ref}}{hc}\right)^2 BW \frac{\tau_{coh}}{2\pi}$$

where k is Boltzmann's constant; T is the temperature in Kelvin; $R_{fb}$is the transimpedance amplifier feedback resistor; BW is the signal passband; and τ_{coh} is the source's coherence time.

Assuming that shot noise is predominant over the other noise sources, the relation between signal and noise becomes [**17**][**16**]:

$$SNR_{TDOCT} = \frac{Signal}{Noise} = \frac{\eta\lambda\alpha\left[\int_{-\Delta\omega/2}^{\Delta\omega/2} S(\omega)\partial\omega\right]^2}{hcBW \int_{-\Delta\omega/2}^{\Delta\omega/2} S(\omega)\partial\omega}$$

If the detection components of an hypothetic system is composed by two photodetectors, instead of a single one used in time domain, with each one receiving half of the source spectrum, the SNR is given by [**16**]:

$$SNR = \frac{\eta\lambda\alpha\left[\int_{-\Delta\omega/2}^{0} S(\omega)\partial\omega + \int_{0}^{\Delta\omega/2} S(\omega)\partial\omega\right]^2}{hcBW\left[0{,}5\int_{-\Delta\omega/2}^{0} S(\omega)\partial\omega + 0{,}5\int_{0}^{\Delta\omega/2} S(\omega)\partial\omega\right]}$$

It is clearly visible that the hypothetic system with two detectors has an improvement in sensitivity by a factor of two. If this relation is extrapolated to a system with M detectors, the SNR obtain is:

$$SNR = \frac{\eta\lambda P_{sample} M}{hcBW}$$

Increasing the number of detectors leads to higher optical intensity noise In order to overcome this problem a balanced detection is required [**16**].

The sensitivity for a Fourier domain OCT can be achieved using the same analysis, but is important to remember that according to Nyquist's theorem the bandwidth per detector becomes $1/2\tau_i$. It is also important to refer that the phase information is lost in the detection, so the final result is reduced by a factor of two. Therefore the signal-to-noise ratio for a FD-OCT is [**4**][**16**]:

$$SNR_{FDOCT} = \frac{\eta\lambda P_{sample}\tau_i}{hc}$$

where τ_i represents the integration time of the detector's array.

1.2 Other Techniques Based on OCT

1.2.1 Full-Field OCT

In order to get three-dimensional images, TD-OCT needs to scan across the sample surface and combine every A-scan. The acquisition time required by conventional OCT systems leads to a trade-off in image density. If the acquisition time is too short, few axial scans will be detected and the final image has low detail. On the other hand, for longer scan times the image density increases, but there will be also a higher probability of eye motion artifacts [**18**][**19**].

Full-field OCT (FF-OCT) and Wide-Field OCT (WF-OCT), Figure 9, are two OCT concepts which improve the acquisition speed. For this reason, they are very helpful in biology applications, like subcellular real-time imaging [**4**].

By replacing the photodetctor in TD-OCT, by a CCD or a CMOS camera, it is possible to get a two-dimensional *en-face* image with a single exposure, with no lateral scans. While FF-OCT uses a microscope objective with a high numerical aperture, the WF-OCT is based on optics imaging with a single lens. Although WF-OCT lights a larger sample area, its lateral resolution is worse than other OCT systems [**20**].

Besides the improvements in acquisition speed, the slow frame rates of available cameras jeopardizes the depth scan acquisition speed [**19**].

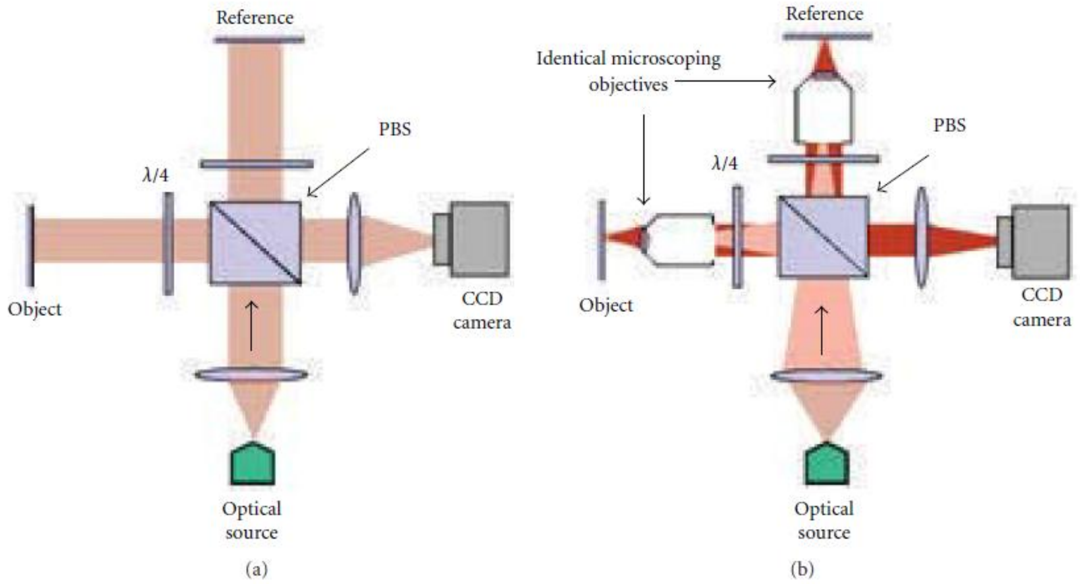

Figure 9 – Schematics of Wide Field OCT (a) and Full Field OCT (b). Reproduced from **[**19**]**

1.2.2 Doppler OCT

Doppler Effect, proposed in 1842, allows determining the velocity of an object, by analyzing the change in frequency of a reflected wave.

Doppler OCT (DOCT), also known as Optical Doppler Tomography (ODT), provides *in vivo* flow velocity measurements. It is a combination of OCT with a Laser Doppler Flowmetry (LDF). The most common applications are the study of vascular pathologies, embryo cardiac dynamics and blood flow measurements under the skin [**21**].

DOTC can use a time or a frequency domain schema, but requires the sample arm to be angled relatively to the flow direction, as illustrated in Figure 10, and the reference mirror to be adjusted to match the capillary depth. Then, it is necessary to analyze the frequency of the detected signal to evaluate the scattering particle velocity. The velocity resolution only depends on the detection electronics and the scanning angle [**4**][**21**].

The Doppler frequency shifted (f_d) and object velocity (v) can be written as [**21**]:

$$f_d = \frac{2n_t v \cos\theta}{c} f_0 \qquad\qquad v = \frac{\lambda}{2n_t \cos\theta} f_d$$

with f_0 and λ the source frequency and wavelength; n_t the refractive index of the tissue; and θ the angle between the sample arm and the sample.

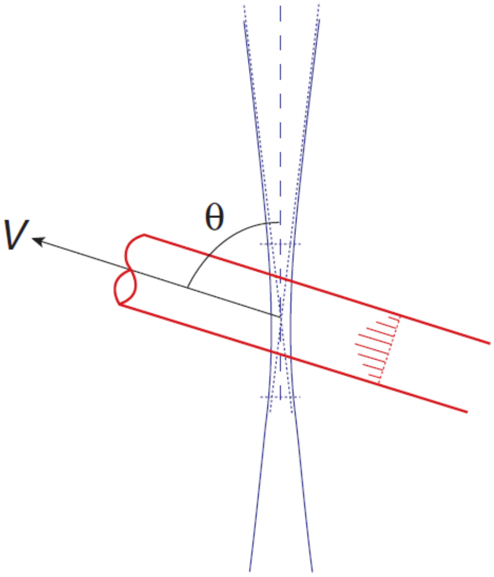

Figure 10 – Diagram of Doppler OCT sample arm. The laser beam (blue) is angled relative to the blood vessel (red). Reproduced from **[**21**]**

1.2.3 Polarization sensitive OCT

Although TD and FD are the most applied OCT configurations, they treat electromagnetic waves as scalar quantities without concern about polarization state and birefringence within the sample. Anisotropic tissues, such as tendons, muscles, teeth, bones, blood vessels, and skin, act as having different refractive indexes for the two polarization states, resulting in an optical delay between those states, in the reflected light in two polarization states with an optical delay between both states. Polarization information can be very useful in retinal imaging particularly in the assessment of optic nerve, an important feature when studying glaucoma. [**4**] [**22**].

For those birrefringent tissues, Polarization Sensitive OCT (PS-OCT), schematized in Figure 11, enhances the image contrast and allows the analysis of both structure and polarization properties of samples [**22**][**23**].

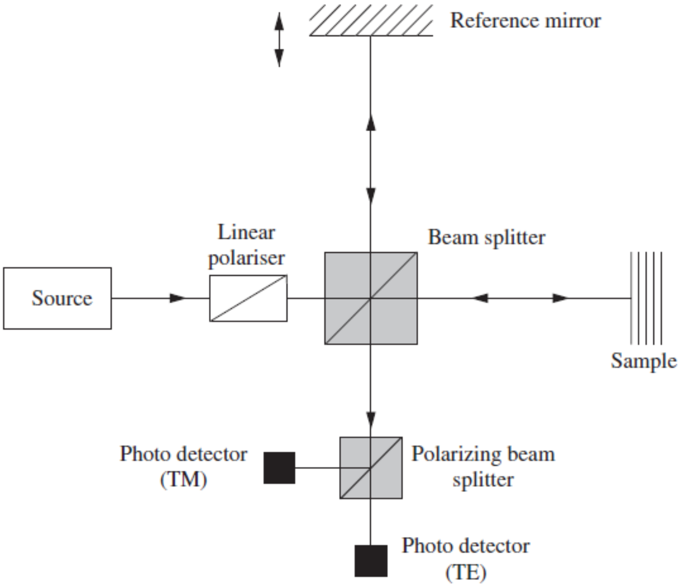

Figure 11 – Schematics of Polarization Sensitive OCT. Reproduced from **[**4**]**

The configuration is similar to TD-OCT or FD-OCT, but between the source and the interferometer, the light beam passes through a linear polarizer and at the end, instead of a single phtodetector or a spectrometer, there is a polarizing beam splitter and two photodetectors. The linear polarizer sets a reference polarization state before the sample. Then, the polarizing beam splitter divides the reflected beam into two orthogonal linearly polarized components (TM and TE), which are detected independently by the two photodetectors. This way, it is possible to measure the beam polarization state [**4**][**24**].

Chapter Two

2.1 State of the art

Nowadays, OCT is well accepted as a fundamental tool for ophthalmology, but this was not always the case. Only after roughly ten years since its invention (in 1991) did it become established in clinical practice. The year of 1996 was marked for the commercialization of the first OCT equipment (Zeiss OCT), with an axial resolution of 10 µm and an acquisition speed of 100 A-scans/s. However, it was not until 2004 that OCT became usual among clinicians [**12**].

The new millennium brought an increasing worldwide interest on this field. OCT improvements were only possible due to simultaneous advances of new broadband light sources emitting at different wavelengths, new tunable light sources, as well as new high-speed Fourier detection techniques. This progress is clearly visible by the large number of publications from 2000 to the present day. The impact caused by OCT is also notorious in clinical applications. After just twelve years since its first commercialization, many companies have released a fourth generation of equipments. This chapter lists some of the most important events about OCT, either in academic studies as in clinical applications [**12**].

The whole theory behind OCT, including Fresnel's laws and Michelson interferometer, was already well studied since the end of 19th Century. In the 1980's several research teams produced axial scans [**25**]. In 1991 Huang et al. obtained a cross-sectional image; and in 1993 two groups, Fercher and Swason, perform the first *in vivo* studies of the human retina, as mention in [**12**].

While many groups were trying to improve time domain systems, in 1995 Fercher [**26**] established the principles of spectral domain detectio. Due to its enormous advantage in acquisition speed, it was adopted in 2004 and became largely used in circumstances which require high speed or ultrahigh resolution, as well as in Doppler OCT [**12**][**27**][**28**][**29**].

In 2002 and 2003, Kowalevicz [**30**] and Unterhuber [**31**] revealed that an ultrahigh resolution OCT (UH-OCT) could be achieved using a solid-state femtosecond Ti:Sapphire laser. In the next two years, Dexter carried out different studies on high resolution OCT images. In 2004, new cost efficient, wide bandwidth SLDs allows resolutions close to the ones obtained with femtosecond lasers, but at center wavelength (>900 nm) superimposed on the range of water absorption[**12**][**32**].

Although UH-OCT has a sub-cellular resolution of 2-3µm which allows the visualization of individual retinal layers, it is only employed in research laboratories due to its high cost. The standard axial resolution for commercial OCT with a SLD source is 10 µm and the newest systems available on the market have an axial resolution of 5-8 µm [**12**].

From 2003 until 2006 many studies demonstrated the visualization of the proximal layers of the retina, including the photoreceptors layer, illustrated in Figure 12. Unfortunately, it has not yet been possible to correlate OCT images of the distal intraretinal layers with histological images. To date, the OCT reaches easily the retinal pigment epithelium (RPE), but beyond that layer, the detected signal is not strong enough to generate an image [**12**][**33**][**34**].

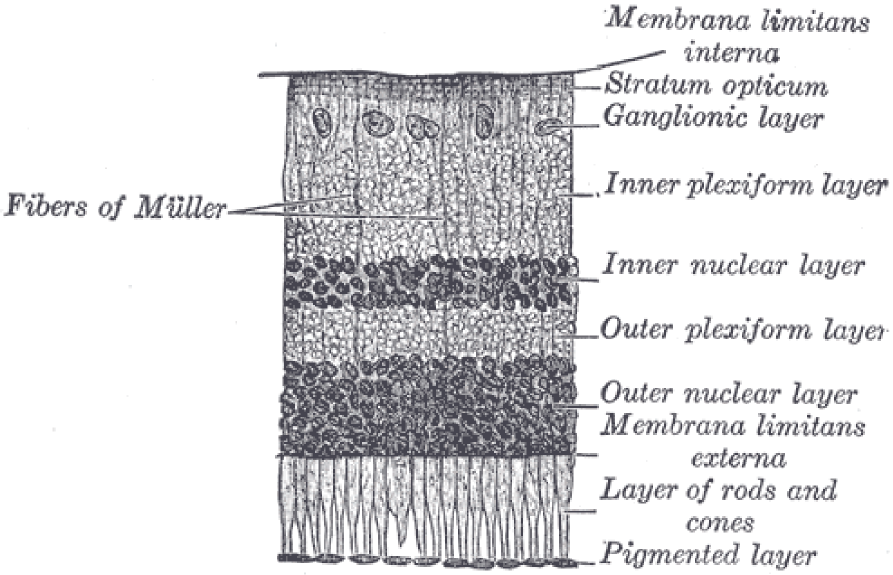

Figure 12 – Retinal Layers. Reproduced from **[**56**]**

Using an OCT source within 800 nm center wavelength is adequate to image the nearest layers of the retina, but higher wavelengths are necessary to achieve deeper tissue penetration and acquire images from distal retina and choroid. It was already known that melanin, a component of RPE, was an extremely scattering and absorbing agent. During OCT studies, it was demonstrated that cataracts and corneal haze also decrease the beam penetration in tissue [**12**].

In 2003 Povazˇay et al. [**35**] [**36**] proved that using a 1050 nm source, layers beneath the RPE as well as choroidal structures could be visualized and delineated, which may be important to an early diagnostic of eye disorders. In 2007, the same team demonstrated the value of imaging at 1050 nm and acquired images with a 7 µm resolution, from patients with cataracts and retinal diseases, as mention in [**12**].

Although 1050 nm allows the imaging of deeper structures it requires the use of InGaAs detectors, because silicon based ones, employed in 800 nm systems, are not sensitive to long wavelengths. This is a disadvantage since InGaAs detectors are more expensive and both pixel density and acquisition speed are slower, which results in images with less quality [**12**].

Another advantage of OCT is the possibility to perform three dimensional images, which are very helpful for quantitative and qualitative measurements in medicine enabling an early and specific diagnostic or the evaluation of disease progress and therapy response. With advanced processing, such as image segmentation, it is also possible to perform virtual biopsy using 3D-OCT images, which is helpful to analyze and identify tissue boundaries and thicknesses. The imaging speed of OCT is essential to acquire the high densities data sets required for 3D images. However, as already stated, there is a trade-off between data rate and sensitivity [**12**].

The first 3D-OCT retinal images used time domain detection with an acquisition time of 64 planes per second in depth, each of them composed by 256×128 pixels, which corresponds to nearly 2 million of voxels per second. The en-faced image had good resolution, but the axial density was limited resulting in poor cross-sectional images [**37**].

Spectral domain OCT contributed significantly to the improvement of acquisition speed, either with FD-OCT or SS-OCT. Although these technologies were already known since 1995 [**26**], they were only implemented several years later, due to limitations in CCD technology. The first clinical researches using an ultrahigh resolution 3D OCT with spectral detection were performed by Schmidt [**38**] and Monson [**39**] in 2005 and 2007, who had successfully got images from patients with retinal pathologies. Currently Fourier domain OCT achieves imaging speeds of 25 million voxels per second which is much faster than time domain OCT [**12**].

From the beginning of spectral OCT, most investigation teams prefer FDOCT rather than SS-OCT, maybe due to the fact that acquisition is limited by tuning speed of laser or the excessive cost of available swept sources. The performance of SS-OCT is related to the swept laser source used which implies some trade-offs between imaging speed, bandwidth, and output power according to laser physics [**12**][**40**].

In 1997, Chinn and Golubovic, as mention in [**12**], developed the first OCT with swept sources of 800 nm and 1300 nm. Several years later, Yun team [**27**] set up a 1300 nm high speed SS-OCT with 14 µm of axial resolution which achieved 16000 A-scans/second. Later, with external cavity tunable semiconductor laser, Srinivasan [**41**] achieved a better resolution, of 7 µm, but worse imaging speed.

Hubert [**40**] discovered in 2006 a new laser technique, Fourier Domain Modelocking (FDML), which overcomes the conventional swept laser limitations and also increases the acquisition speed. Therefore, using their technology, the same team achieved 370000 A-scans per second with an axial resolution of 10 µm, as mention in[**12**].

Although SS-OCT could reach imaging speeds 10 times faster than FD-OCT, to date it is impossible to obtain images with the same resolution. Another disadvantage of FDML is the reduced performance when imaging at 800 nm, due to dispersion in fiber cavity necessary in this process [**12**].

Shortly after the initial development of OCT, several teams investigated the possibility of getting not only structural images but also functional images. Doppler and Polarization Sensitive OCT were the most important developments for functional imaging OCT [**12**].

The early studies about DOCT were performed in 1995 by Wang [**42**]. One advantaged of frequency domain DOCT, demonstrated in 2003 by Leitgeb [**43**] and White [**28**], is that the phase information is immediately obtained from the detected spectrum. The available DOCT can easily achieve blood flow sensitivities of less than some tens of micrometers per second. Since quantitative measurements of retinal perfusion remains complicated, DOCT is used to enhance the image contrast in clinical applications [**12**].

PS-OCT was also demonstrated early by two research groups, in 1997 by Hee et. al. and in 1999 by Boer team [**44**]. In 1997 Zhou and Knighton, as mention in [**12**], proved that by combining both information from thickness and birefringence it is possible to make an accurate diagnostic of glaucoma. A variation of PS-OCT was proposed by Hitzenberger [**45**] in 2001, which acquired reflectivity, retardation and optic axis orientations parameters simultaneous. Although it advantages, it is necessary to perform more studies until PS-OCT become used among clinicians[**12**].

OCT became even more powerful and helpful in research with the possibility to perform studies in animal models, since rodents and monkeys play an important role to better understand eye structure and diseases. As OCT is a non-invasive technique, one animal can be subjected to repeated measures in order to evaluate disease progression or therapy response, in contrast to histology and other imaging methods where the animals have to be sacrified [**12**].

For this reason, several animal studies were performed, in order to get a better knowledge about eye structure. In 2003, Gloesmann's team [**46**] obtained retinal images from pigs, and in 2004 and 2005 Anger group [**47**] and Ahnelt and Drexler [**48**][**49**] used monkeys. They proved that it is possible to visualize important structures and that images could be correlated to the ones obtained through histological preparations. Given that mice and rats eyes are much smaller than human, it is necessary to use high resolution equipment. In 2006 Srinivasan et. al. [**50**], using a high speed frequency domain OCT (24000 A-scans/s) with a resolution of 2,8μm, acquired a three dimensional image composed of 256 B-scans with 512 axial scans each.

OCT will play a crucial role in monitoring and validating novel therapeutic approaches, but it will not replace the 'gold standard' of biopsy and histology or the already used imaging modalities. Its unique features will enable a large range of new research and clinical applications that will complement the available imaging technologies and enlarge the knowledge on retinal biology and function [**12**].

Chapter Three

3.1 Simulation

As stated in chapter one, there are key equations that govern and define the OCT signal. We simulated them in *MATLAB* ®, in order to get a comprehensive knowledge and understanding on how different sources and samples influence the interferogram. Our simulation was based on Tomlins and Wang study [**4**].

$$I(\Delta z) = \frac{1}{4}\int_{-\infty}^{+\infty} S(\omega)(|H(\omega)|^2 + 1)\,\delta\omega + \frac{1}{2}\int_{-\infty}^{+\infty} S(\omega)H(\omega)\cos[\phi(\Delta z)]$$

$$I(\omega) = \frac{1}{4}S(\omega\{H(\omega) + 1\}^2)$$

The time domain signal obeys the equation $I(\Delta z)$, similar to the one presented in Chapter one, and is readily obtained from it. On the other hand, for frequency OCT we need to perform a Fast Fourier Transform (FFT) on the density spectrum given by $I(\omega)$, so we can see the sample's depth profile.

Initially, we define a Gaussian source spectrum, with center wavelength at 800 nm and a spectral linewidth of 50 nm (Graphic 3):

$$S(\omega) = e^{\frac{(\omega - \omega_{center})}{2\sigma}}$$

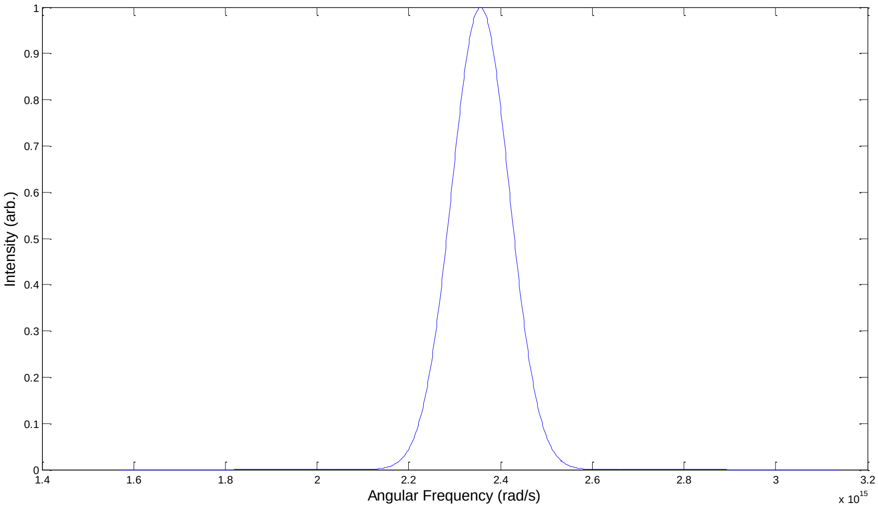

Graphic 3 – Simulated spectrum of Gaussian source

Secondly we had to identify, Table 2, our sample optical and structural features, such as refractive index and thickness, in order to modulate its frequency response function, given by:

$$H(\omega) = \sum_{j=1}^{N} r_j e^{\left(2i\frac{\omega}{c}\sum_{m=1}^{j} n_m z_m\right)}$$

where N is the number of sample's layers; n_m and z_m are the refractive index and thickness of the mth layer; and r_j is the reflectance of each layer given by:

$$r_j = \frac{n_{j+1} - n_j}{n_{j+1} + n_j}$$

Table 2 – Sample 1 properties

Layer	Refractive index (n)	Layer thickness (z)
1	1.00	5.00 µm
2	1.30	15.00 µm
3	1.50	30.00 µm
4	1.00	0.00 µm

Graphic 4 and Graphic 5 represent the detected signals for time and frequency domains, respectively; Graphic 6 corresponds to the FFT from $I(\omega)$ By analyzing these graphics it is clear visible that both detection system achieved the same information

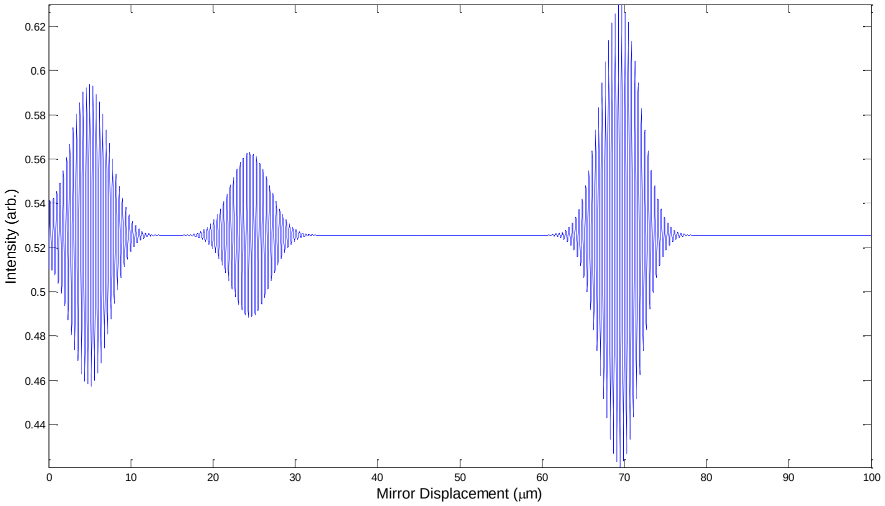

Graphic 4 – Simulated time domain interferogram of Sample 1, $\boldsymbol{I(\Delta z)}$

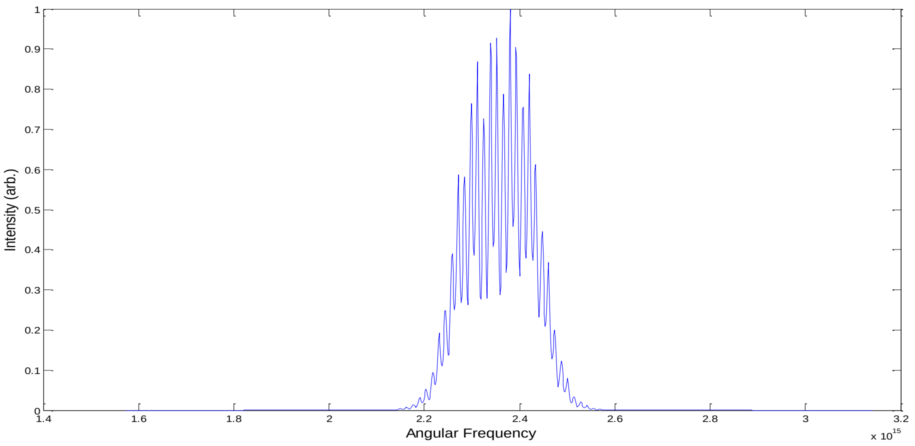

Graphic 5 – Simulated spectral intensity (FD-OCT) signal of Sample 1, $\boldsymbol{I}(\boldsymbol{\omega})$

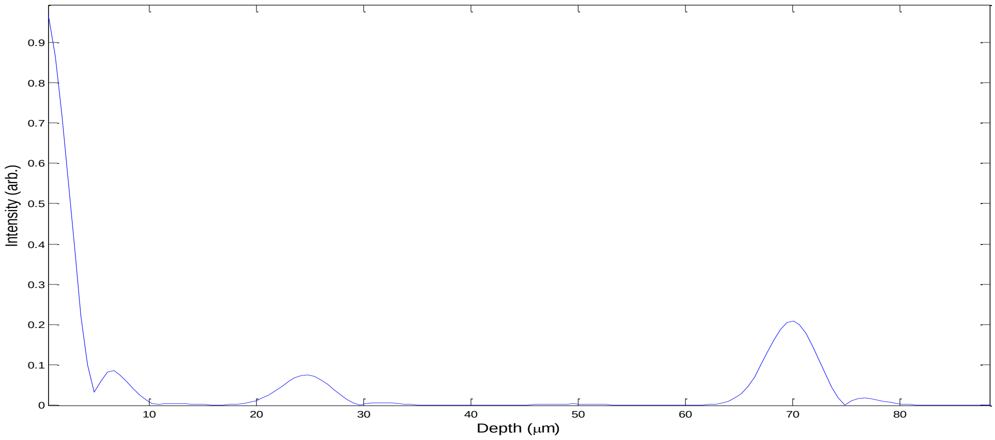

Graphic 6 – Fourier transform of spectral intensity, clearly shows interference at layer interfaces.

In this simulation we not only identify the different OCT signals, but we also get a better comprehension about how the signal behaves when changing the sample and/or source parameters.

For example, maintaining the source and changing the sample to have one layer with 3 μm of thickness (Table 3), it is not expected that our virtual system axial resolution is enough to discriminate between different layers, as seen in Graphic 7.

Table 3 – Sample 2 properties.

Layer	Refractive index (n)	Layer thickness (z)
1	1.00	15.00 μm
2	1.30	3.00 μm
3	1.50	25.00 μm
4	1.00	0.00 μm

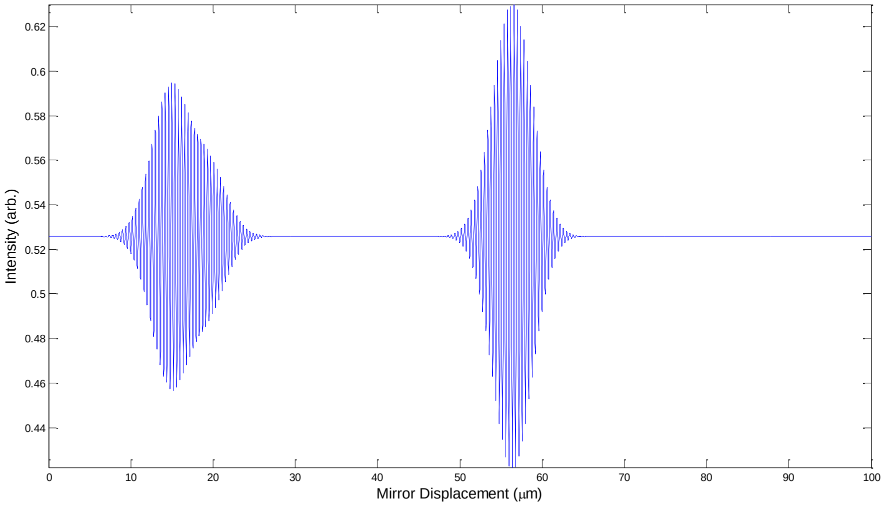

Graphic 7 – Simulated time domain interferogram of Sample 2, using a source with center wavelength at 800 nm and a linewidth of 50 nm. It is visible that layer 1 and layer 2 are superimposed.

Therefore, by lowering the center wavelength and/or increasing the bandwidth, it is possible to improve the axial resolution and clearly differentiate the closest layers. In a real system these features are linked to the light source available on the market.

Graphic 8 and Graphic 9 show the axial resolution enhancement for two situations. The first one using a source with a center wavelength of 400 nm and a linewidth of 50 nm, while for the second one we simulated a source with a center wavelength of 800 nm and a linewidth of 150 nm.

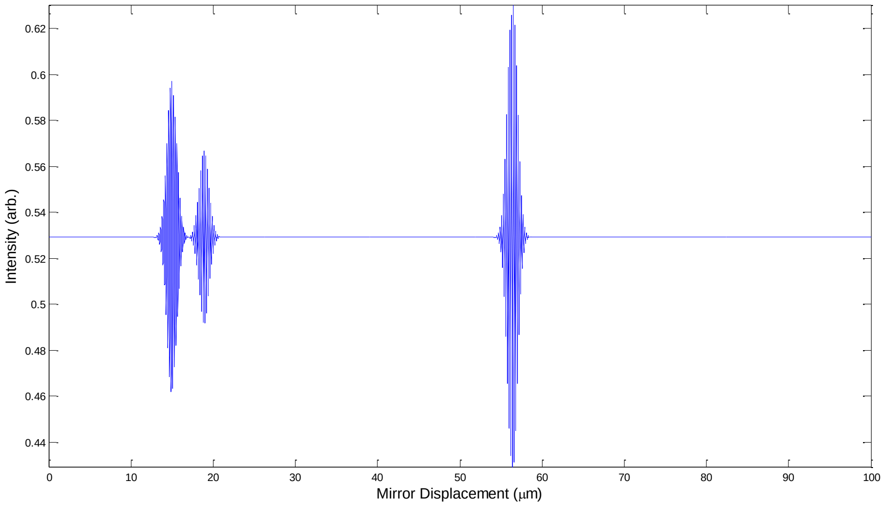

Graphic 8 – Simulated time domain interferogram of sample 2, using a source with center wavelength at 400 nm and a linewidth of 50 nm

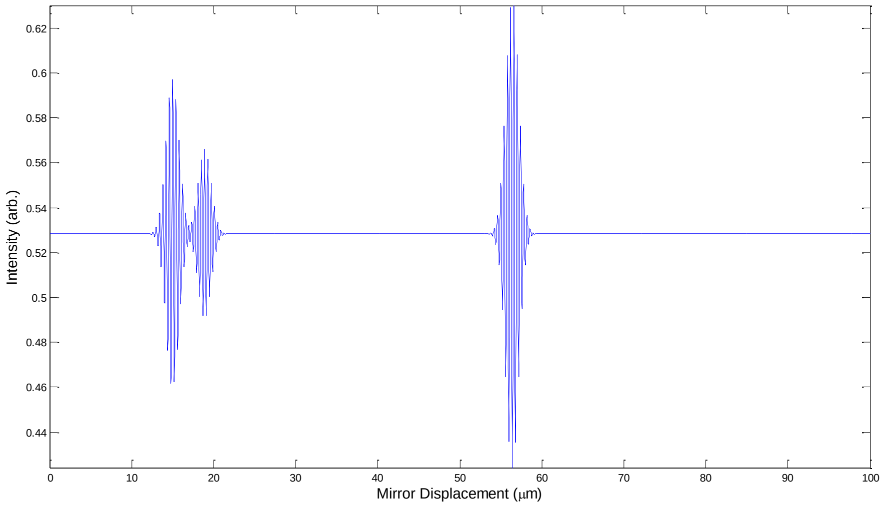

Graphic 9 – Simulated time domain interferogram of sample 2, using a source with center wavelength at 800 nm and a linewidth of 150 nm

Clearly for retinal imaging purposes, a light source with a wavelength centered at 400 nm is not realistic; Graphic 8 merely illustrates how center wavelength influences the signal.

Chapter Four

4.1 OCT Setup

After we installed and performed several tests and modifications on the equipments' set up, we were able to assemble an OCT bench system capable of acquiring an interference signal.

Figure 13 is a photograph of the final bench system, and Figure 14 is a diagram which illustrates how the different equipments are connected.

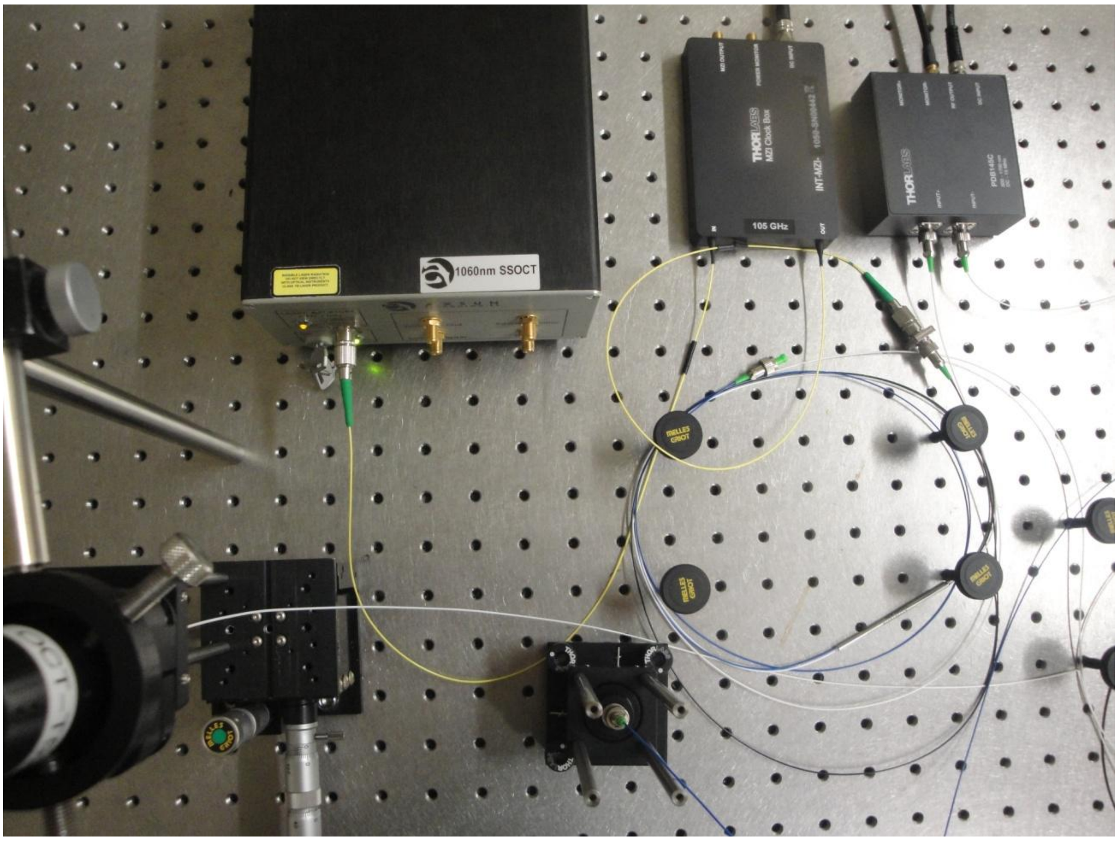

Figure 13 – Bench configuration of our OCT system. Above from left to right are: *Axsun* swept source, MZI interferometer; and balanced detector. Below are the sample (left) and reference (right) arms

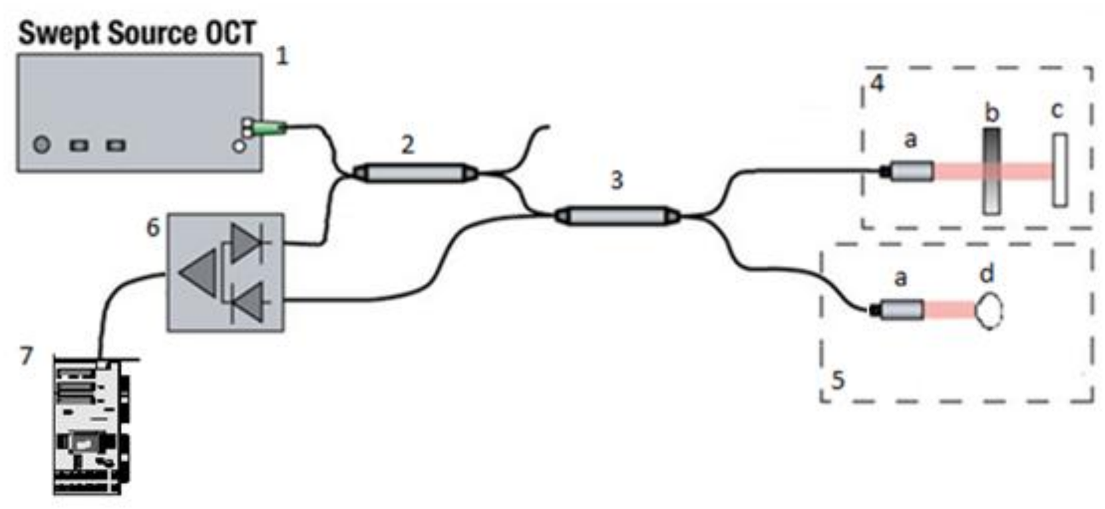

Figure 14 – Final OCT diagram

1. Swept Source
2. 90:10 Coupler
3. 50:50 Coupler
4. Reference Arm:
    a. Collimator
    b. Lens
    c. Gold Mirror
5. Sample Arm:
    a. Collimator
    d. Target
6. Balanced Detector
7. DAQ Board

In our bench system, the *Axsun* swept source generates the laser beam. Connected to the source is a Mach-Zehnder interferometer, not represented in Figure 14 because currently its only function is to attenuate the optical power by a factor of 5%. After exiting the interferometer the beam passes through two couplers, which drive it to the reference and sample arm. The reference arm is composed by a collimator to allow laser alignment and a lens that focuses the beam on a gold mirror. The sample arm is mounted in a moving platform and only has a collimator and a target. After reflection in both arms, the beams interfere in the couplers. The first coupler is attached to the positive monitor of a balanced detector and the second is linked to the negative one. The detector is connected to a DAQ board which transfers the information to a host PC enabling data visualization and processing.

Below, in this chapter, are listed the operation methods of the key components, as well as their main features. In Appendix A, the data sheets from all the equipments are specified. All the information is based on the user's manual provided by manufacture.

4.1.1 *Axsun* Swept Source

The *Axsun* OCT Swept Source Engine (AXSUN Technologies Inc., Billerica, Massachusetts, USA) is classified, according to IEC 60825-1 standard, as a Class 1M LASER Product. It is safe to use in all conditions and usually the Maximum Permissible Exposure (MPE)[1] cannot be exceeded (Figure 15). If the LASER beam passes through optical instruments, such as microscopes and telescopes, the risk of causing injuries increases and the product class may change. Typically, Class 1M lasers produce large-diameter beams or divergent beams.

Figure 15 – Warning Label for Class 1M LASER

When working with the *Axsun* SS-OCT Engine, there are several procedures we need to take into consideration:

- The internal components are sensitive to electric discharges
- The LASER should only be turned on with a cord attached. Otherwise there is a risk of damaging the fiber end inside the unit.

The *Axsun* OCT Swept Source Engine, Model SSOCT-1060 (Figure 16), is based on *Axsun Technologies*' optical integration platform and patented MEMS tunable optical filter. It produces a pulsed laser beam at every 10 µs, although the laser duty cycle, the interval of time where the laser is turned on, is about only 5/6 µs. The laser spectrum is in the Near Infrared (NIR) region, center at 1060 nm with a linewidth of 110 nm.

---

[1] MPE - The maximum power or energy density of a light source which does not cause any damage. It is measured at the cornea or skin for a given wavelength and exposure time.

Figure 16 is a generic vision of *Axsun* swept source and Figure 17 are detailed views of the frontal and rear panels.

Figure 16 – *Axsun* Swept Source OCT bench version

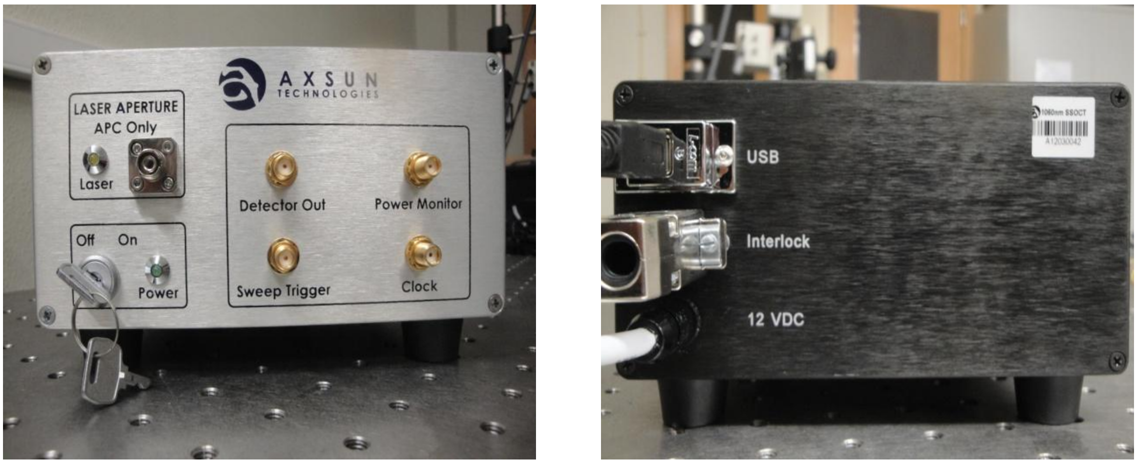

Figure 17 – Front and rear panels of *Axsun* source.

4.1.2 *Thorlabs* Balanced Detector

Thorlabs PDB145C Balanced Amplified Photodetector (Thorlabs GmbH, Munich, Germany), in Figure 18, consists of two well-matched photodiodes and an ultra-low noise, high-speed transimpedance amplifier that generates an output voltage proportional to the difference between the photocurrents in the two photodiodes, i.e. the two optical input signals.

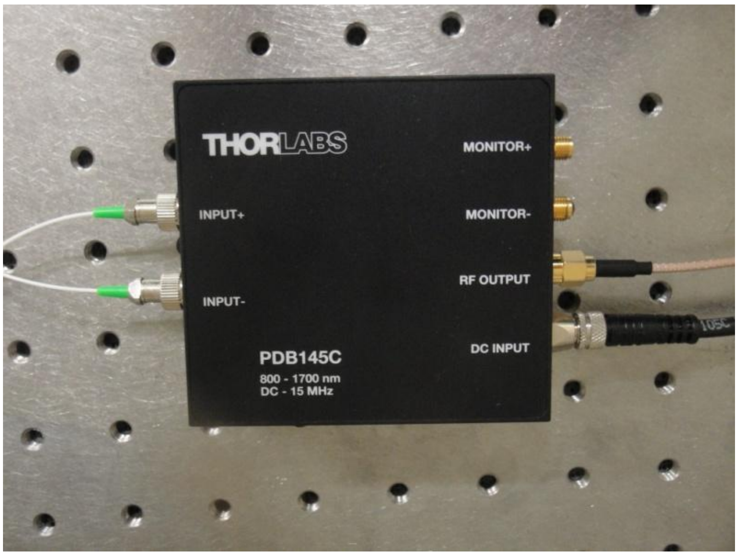

Figure 18 – *Thorlabs* balanced detector

The fiber inputs are coupled to the photodiodes using two removable FC adapters, which can accommodate either single-mode or multi-mode fiber with FC/PC or FC/APC connectors. When using free-space beam applications the FC adapters should be removed in order to get accurate measurements.

The detector can be used in balanced mode (both inputs are illuminated) as well as in single detector mode. In single detector mode, the *RF OUTPUT* swing depends on which input is used, it is positive for *INPUT+* while it is negative for *INPUT-*.

The PDB145C has three SMA output connectors, carrying *INPUT+/INPUT-* monitoring signals (*MONITOR+ / MONITOR-*) and the balanced output signal (*RFOUTPUT*).

RF OUTPUT output voltage is proportional to the difference between the photocurrents in the two photodiodes and its maximum output voltage swing is ±3.6 V for high impedance or ±1.8 V for 50 Ω impedance loads

The signal monitor outputs allow observation of the input power levels and are used as independent power meters for each channel. These outputs are low frequency outputs and cannot be used to measure RF modulation on the signal. The maximum output voltage swing of the MONITOR output is +10 V and saturation will occur at optical input power greater than 100μW. The monitor outputs are designed to drive high-impedance loads.

Figure 19 is a functional diagram of the balanced detector.

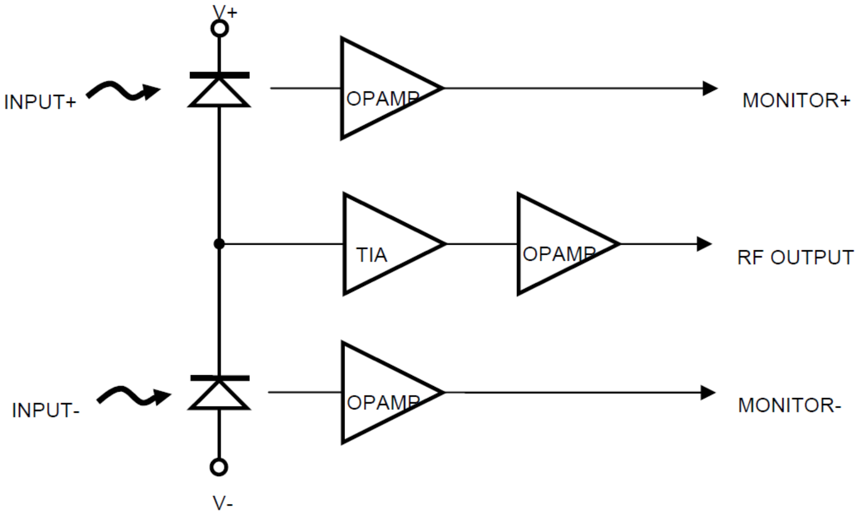

Figure 19 – Functional block diagram of balanced detector

4.1.3 *Innovative Integration* DAQ Board

The X5-400M (Innovative Integration, Simi Valley, California, USA), in Figure 20, is an XMC IO module with a programmable microprocessor (Virtex5 FPGA) which communicates to a host pc by PCI Express. The Virtex5 core has 512 MB DDR2 and 4MB QDR-II memories. The close connection between the analog IO, memory and host interface allows real-time signal processing with high performance and rates.

The X5 an XMC module is attached to a host board with *Innovative's* powerful *Velocia* architecture. It has a 8-lane PCI Express interface that provides over 1 GB/s transfer rates.

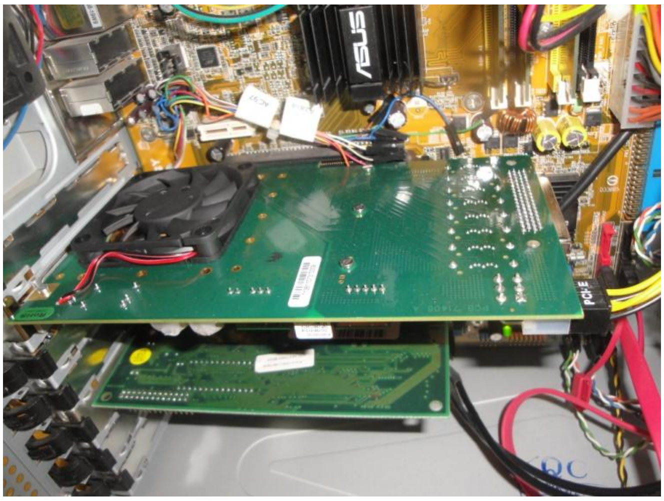

Figure 20 – *Innovative Integration* DAQ board

Figure 21 represents a functional diagram of acquisition board.

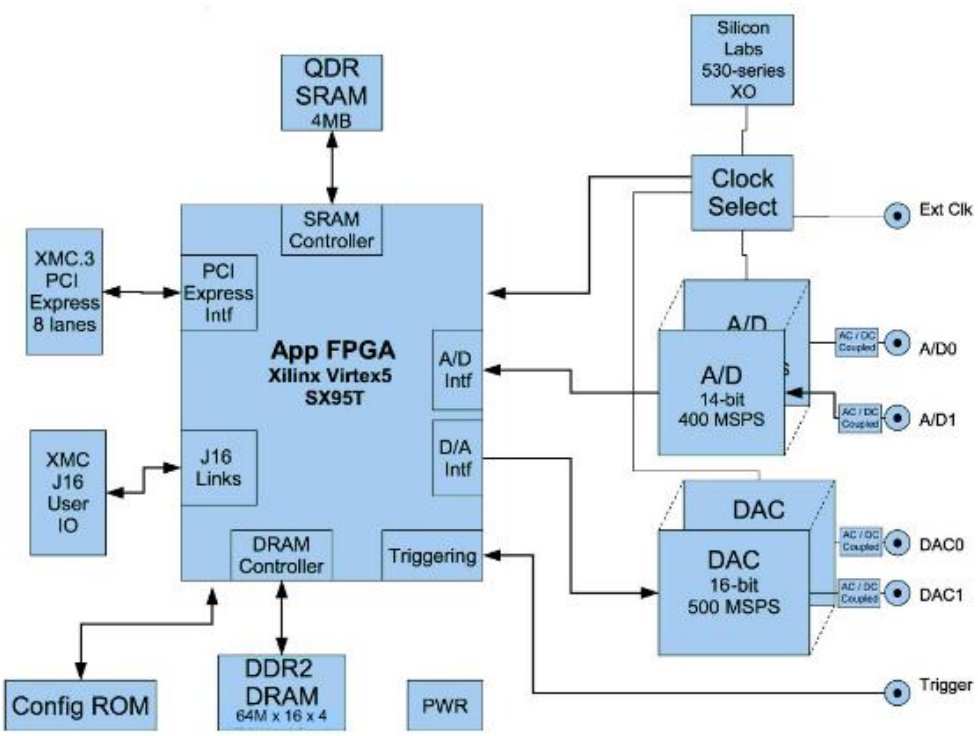

Figure 21 – X5-400M block diagram

The FPGA firmware could be developed or modified using Framework Logic. FrameWork Logic tools are written in *MATLAB* and *Register Transfer Language* (*RTL)*. On one hand, the *MathWork* tools provide a graphical block diagram environment for hardware-in-the-loop and support real-time data generation and analysis. One the other hand, the *RTL* tools complement the *MATLAB* environment and offer the flexibility of a high-level language.

Innovative Integration provides software tools for host development that include *C++* libraries and drivers for *Windows* and *Linux.* The software pack also includes basic applications just to demonstrate the module features and applicability.

4.1.4 Thorlabs Interferometer

Due to its time non linearity, the swept source must be optically clocked or calibrated to achieve equal spaced sampling in k-space (or frequency space). The calibration trace is obtained resorting to an interferometer, either a Michelson or a Mach-Zehnder [**51**].

The *Thorlabs* INT-MZI 1050 Interferometer (Thorlabs GmbH, Munich, Germany), in Figure 22, is very useful in swept source OCT systems. It provides both Power Monitor and k-Clock signals to check the output power and the swept source wavelength.

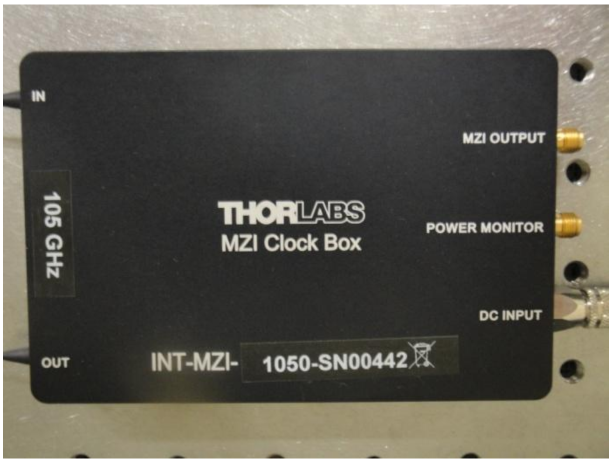

Figure 22 – *Thorlabs* INT-MZI interferometer

Figure 23 shows the operation of the MZI interferometer. Nearly 5% of the input light is captured to produce the Power Monitor and MZI output, while the remaining light goes to the Output connector.

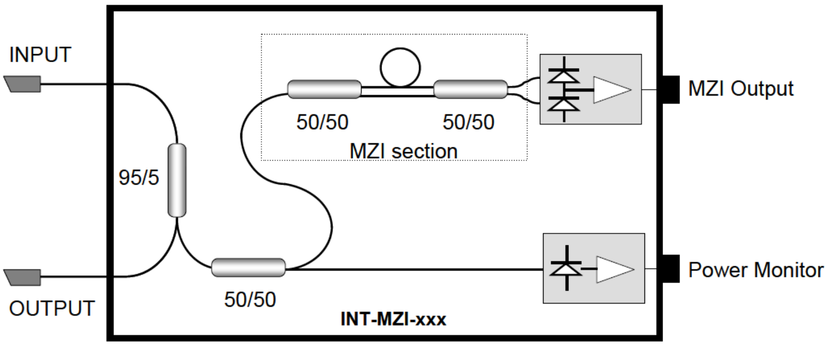

Figure 23 – Functional diagram of the MZI 1050 Interferometer

The *Monitor Output* signal is proportional to the optical input power. The input light is transmitted and detected by a photodiode and amplified.

The k-clock signal is generated by a Mach-Zehnder interferometer, *MZI Output*. The signal has the property to be periodic for every change in the source wavelength. The signal maxima and minima are equally spaced in optical frequency domain. This signal is very helpful, in swept source OCT imaging systems, to trigger the acquisition and guarantee that data points are equidistant in frequency. The interferometer signals are connected into two well-matched photodiodes.

For both signals the maximum output voltage swing is +3,6 V and +1,8 V for high impedance and 50 Ω loads. For this reason the output signal should be below this maximum output voltage to avoid saturation.

4.1.5 *Thorlabs* OCT Lenses, Gold Mirror and Collimator

Thorlabs' scan lenses are objectives used in laser imaging systems since they enable a flat imaging plane thus it is not necessary post processing to correct optical aberrations. Another important advantage of these lenses is that the spot size in the image plane is almost constant over the entire field of view. In table 4 are listed the important features of both types of lenses, LSM02-BB and LSM03-BB (Thorlabs GmbH, Munich, Germany).

Table 4 – Lenses features

	LSM02-BB	**LSM03-BB**
Magnification	10X	5X
Design Wavelength	1050 nm	
Wavelength Range	±50 nm	
Effective Focal Length	17,97 mm	35,88 mm
Lens Working Distance	7,5 mm	25,0 mm
Scanning Distance	16,1 mm	18,9 mm
Pupil Size (1/e^2)	4 mm	
Depth of View	0,12 mm	0,58 mm
Field of View	4,7 mm x 4,7 mm	9,4 mm x 9,4 mm
Parfocal Distance	30,7 mm	50,5 mm
Mean Spot Size	11 µm	21 µm
Scan Angle	±7,5º	

Gold is the most efficient reflective coating over the entire IR range. For this reason we choose a gold mirror, for the reference arm. Graphic 10 shows the mirror's reflectance for different incidence angles, according to the wavelength.

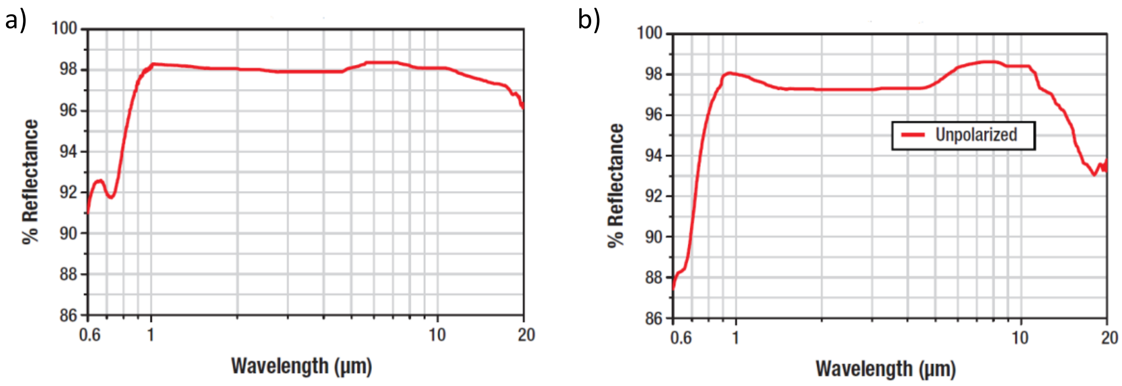

Graphic 10 – Mirror reflectance for different wavelengths and two angles of incidence; a)0º and b)45º

The F260APC-C collimator (Thorlabs GmbH, Munich, Germany) is ideal for systems that are sensitive to back reflections. The end face of the APC connector is angled by 8 degrees, which leads to a return loss greater than 60 dB. Table 5 lists some of the collimator's properties.

Table 5 – Collimator features

Design Wavelength	1310 nm
Wavelength Range	1050 – 1620 nm
Output Waist Diameter	2,7 mm
Divergence	0,035°
Numerical Aperture	0,16 mm
Effective Focal Length	15,30 mm

4.2 Thorlabs Scanning System

In the final month of this year's project, when we were already acquiring interference signals, we received the *Thorlabs* scanning mirrors. Since our time was limited we did not install the scanning system in the OCT bench system. We only checked the equipment and performed the basic tests to understand its operation.

A galvanometer is an instrument which detects and measures small electric currents. It uses a wire wound into a coil and a permanent magnet, when current flows through the wire creates a magnetic field which interacts with the field from the magnet. Due to the fact that Galvo Scanners are easily programmed to achieve different scanning resolutions, frequencies or velocities, they are widely used from commercial to medical applications, such as barcode reading, laser etching, laser measurements and confocal microscopy. [**52**].

The GVS002 system (Thorlabs GmbH, Munich, Germany), represent in Figure 24, consists of two main components: a motor that moves the mirror and a detector that feeds back mirror position information.

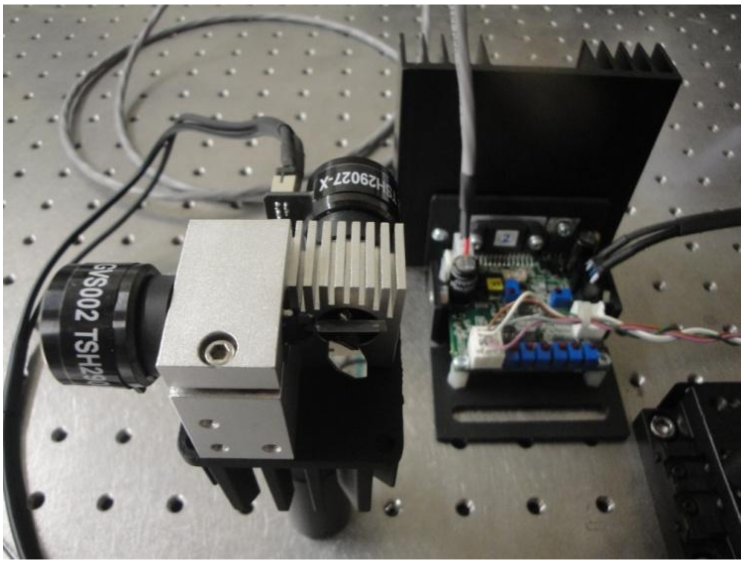

Figure 24 – *Thorlabs* galvo system

The laser beam enters the system and hits the mirror on the X scanner. After reflection, the beam travels to the second mirror, on Y-axis. Thereby, the coordinates of the outgoing ray are determined by the rotation angles of the mirrors [**11**].

The mirror assembly is attached to the end of an actuator, and moves according to the angular range of the motor shaft. The motor has a limited range and its acceleration is proportional to the current that flows through its coils. If there is no current on the actuator, the mirror remains stationary and the laser beam remains at the center of the target, whereas when positive current travels through the coil the motor rotates and the beam is deflected to the right. Otherwise, if there are polarity changes, the mirror moves to the other side [**53**].

The detector is composed of two pairs of photodiodes and a light source. The current produced by the photodiodes changes according to the variations on detected light from mirror movements.

The servo board, represented in Figure 25, interprets the signals from the position detector and the input current to generate an output which controls the actuator position.

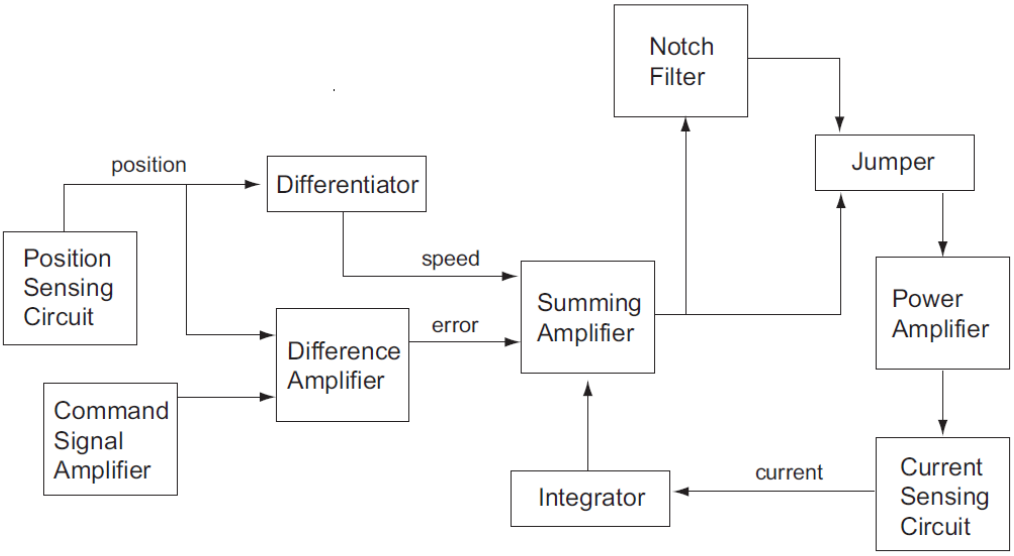

Figure 25 – Servo board diagram

We connected one servo board, with the supplied cable, to the corresponding mirror motor (Y-mirror) to control the scanning system only in one direction. Because the *Axsun* source has a wavelength longer than visible light (NIR), we used a common laser pointer to see the scanning line. To control the scanning range and velocity, by changing wave amplitude, frequency and/or type, we used a signal generator. For this purpose, we needed to wire the J7-command input connector pin (see Appendix A)- from servo board to the function generator, according to Figure 26.

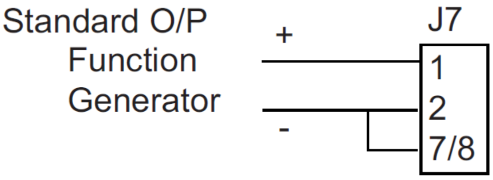

Figure 26 – J7- command input connector pin- connection diagram

Chapter Five

5.1 Results and Discussion

5.1.1 Equipment tests and acquired signals

During this year, we tested and installed the OCT system components. Several instruments setups were tested before the final configuration.

First we installed, on a desktop PC computer, all the hardware and software required to the suitable for data acquisition, namely the Innovative Integration DAQ board.

Afterwards, we start acquiring signals using the swept source outputs, the interferometer and the balanced detector. The signals from the laser source and from the interferometer were consistent with the data sheets and behave as expected. However, we could not perform any measurement with the detector, because it saturated when we connected it directly to the fiber from *Axsun* source. Due to this difficulty, we ordered two couplers, for reducing the optical power at the detector.

Below we present the first signals acquired using the DAQ board. Graphic 11 and Graphic 12 are from the *Axsun* source and represent its clock and trigger signals.

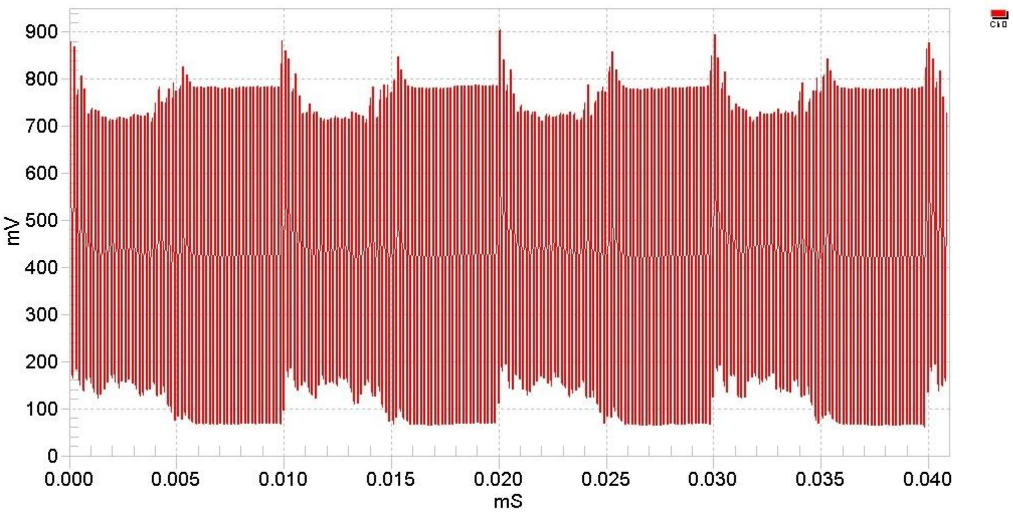

Graphic 11 – Acquired *Axsun* clock signal, using DAQ board

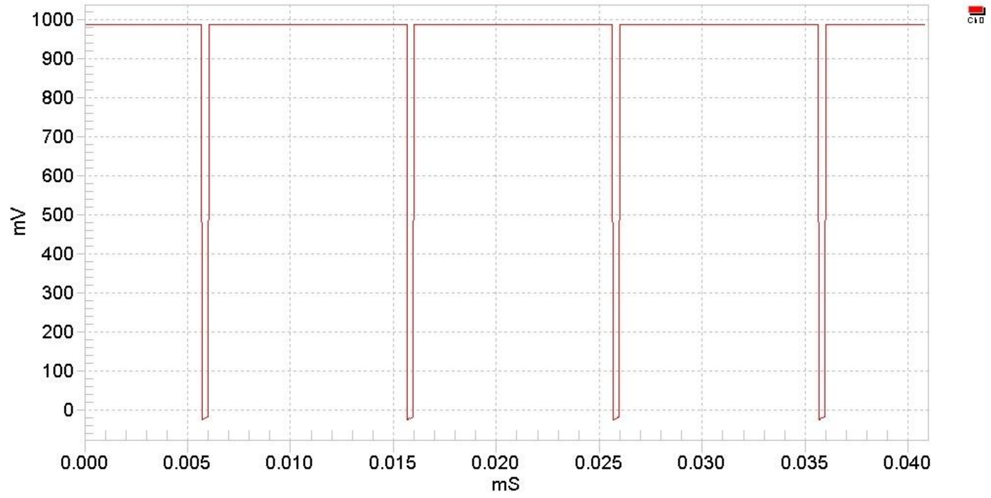

Graphic 12 – Acquired *Axsun* trigger signal, using DAQ board

Graphic 13 and Graphic 14 are obtained by monitoring the POWER MONITOR and MZI OUTPUT outputs from the MZI interferometer. Graphic 13 corresponds to 2.5% of the laser optical power. Graphic 14 is the source's autocorrelation.

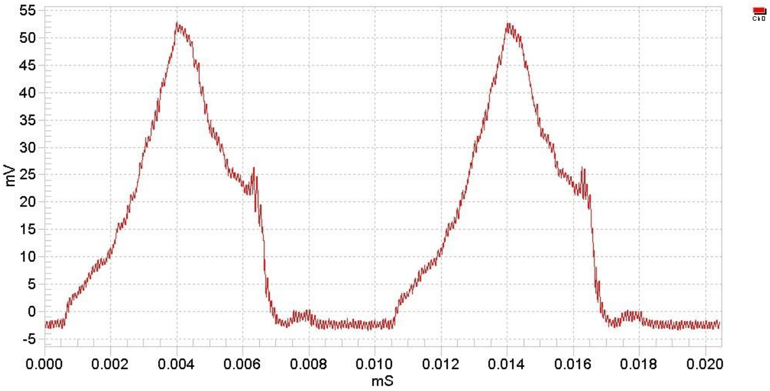

Graphic 13 – Acquired power output signal from MZI interferometer, using DAQ board

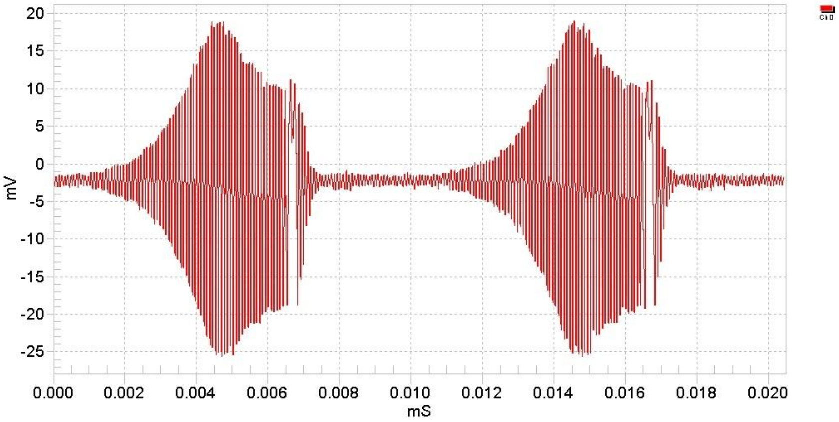

Graphic 14 – Acquired MZI output signal, using DAQ board

Then we started to assemble the reference arm, using a collimator to allow the beam alignment, an available lens and a common mirror. Since we only had one collimator and without it the fiber alignment is impossible, we could not mount the sample arm. Thus the first reflectance signal we acquired, represented in Graphic 15, was not an interference signal.

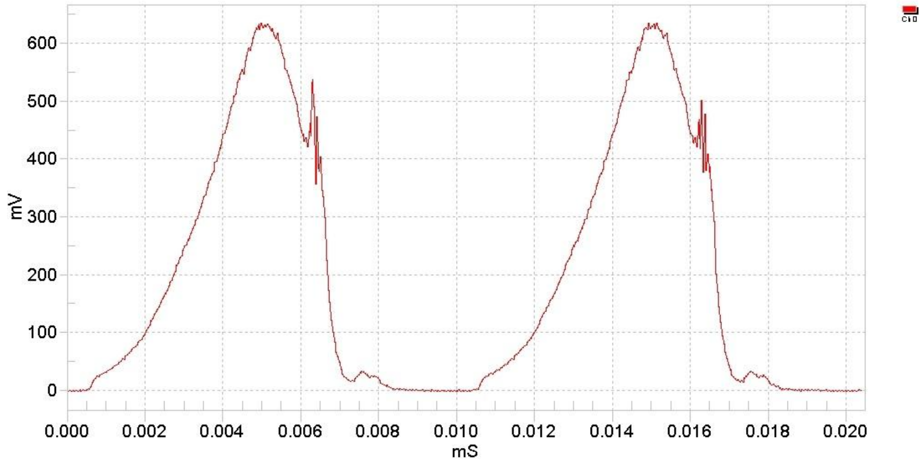

Graphic 15 – Acquired reflectance signal from reference arm, using DAQ board

In Graphic 16 are represented the signal from power output from MZI interferometer (blue; also shown by Graphic 13) and the detected signal from reference reflectance (red; also shown by Graphic 15). The signals do not have the same origin, but they are strictly related. Although they have the same profile, the reflectance signal is smoother because of the not ideal mirror's characteristics. The amplitude difference observed is because the power output from MZI only represents 2,5% of the total optical power.

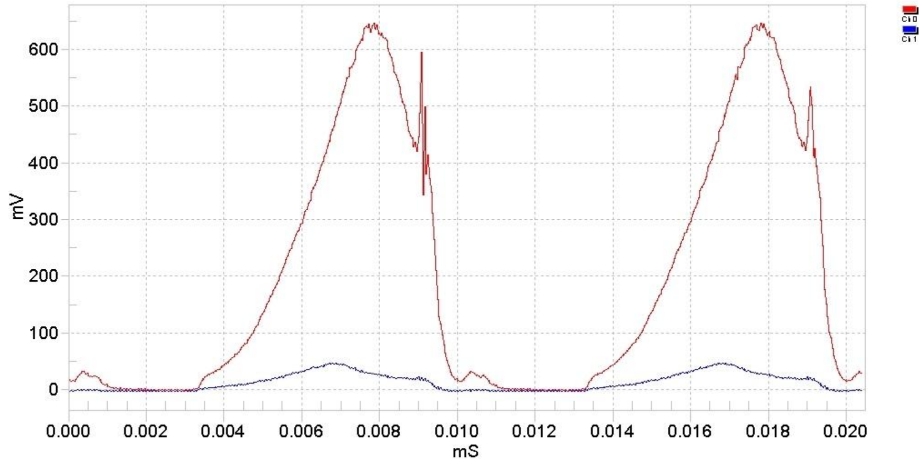

Graphic 16 – Acquired reflectance from reference arm (red) and power output from MZI interferometer (blue) signals, using DAQ board

Afterwards, a gold mirror was bought to replace the mirror initially placed in the reference arm and improve its performance. The sample arm was mounted using the same components of the reference, except the mirror. In Figure 27 are illustrated the optical components used in both arms: collimator (a); OCT scan lenses (b); and the mirror (c).

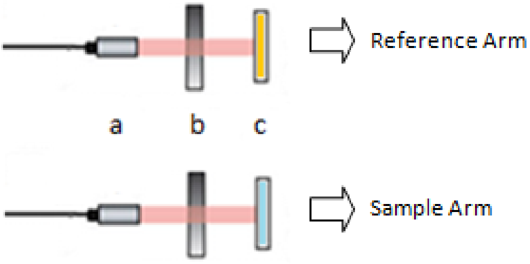

Figure 27 – Diagram of reference and sample arms

Graphic 17 and Graphic 18 are two examples of the signal obtained with the configuration described before. The difference in the amplitude of the detected signal is results from changing the lenses working distance. It is clear that it was not the expected interferogram.

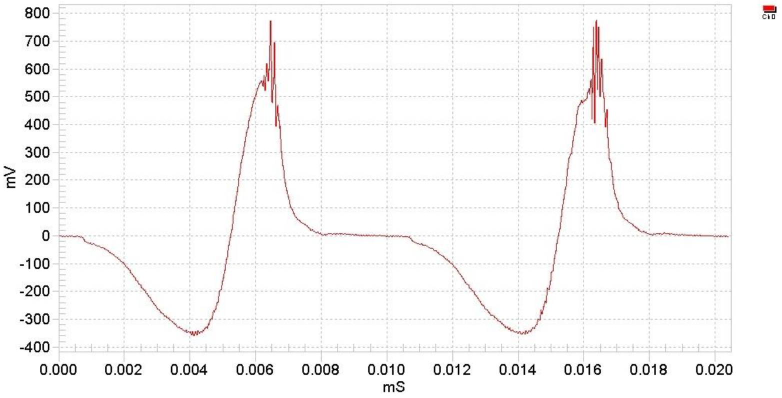

Graphic 17 – Acquired signal 1 from reflectance of both, reference and sample, mirrors, using DAQ board

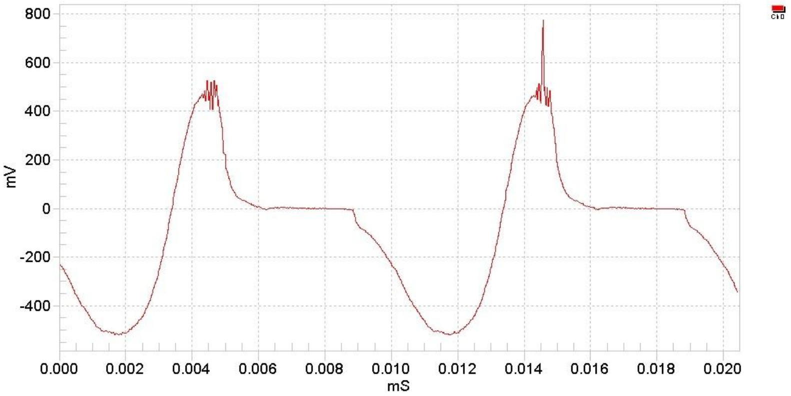

Graphic 18 – Acquired signal 2 from reflectance of both, reference and sample, mirrors, using DAQ board

Finally, we modified the sample arm, replacing the mirror by a target used for servicing the Spectralis ophthalmic imaging system (Heidelberg Engineering, Heidelberg, Germany) in the OCT mode, allowing us to capture an interference signal. After applying the necessary processing, including the Fourier transform and scaling, we recovered the information from each interferogram (A-scan), represented in Graphic 19.

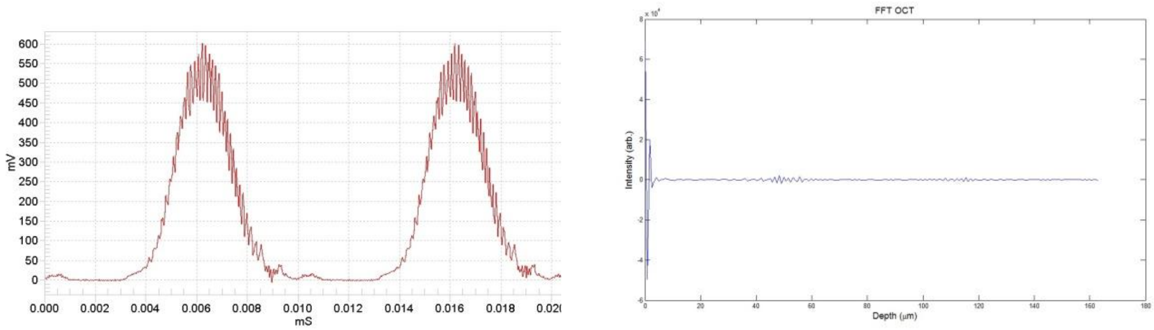

Graphic 19 – Acquired A-scan of the Spectralis target, using DAQ bard, and its corresponding depth profile

It is also essential to mention that the final sample arm was mounted on a platform with three micrometer screws which are important to control the beam position and perform a manual scan of the sample. Below in Graphic 20 are shown three A-scans for different positions within the target.

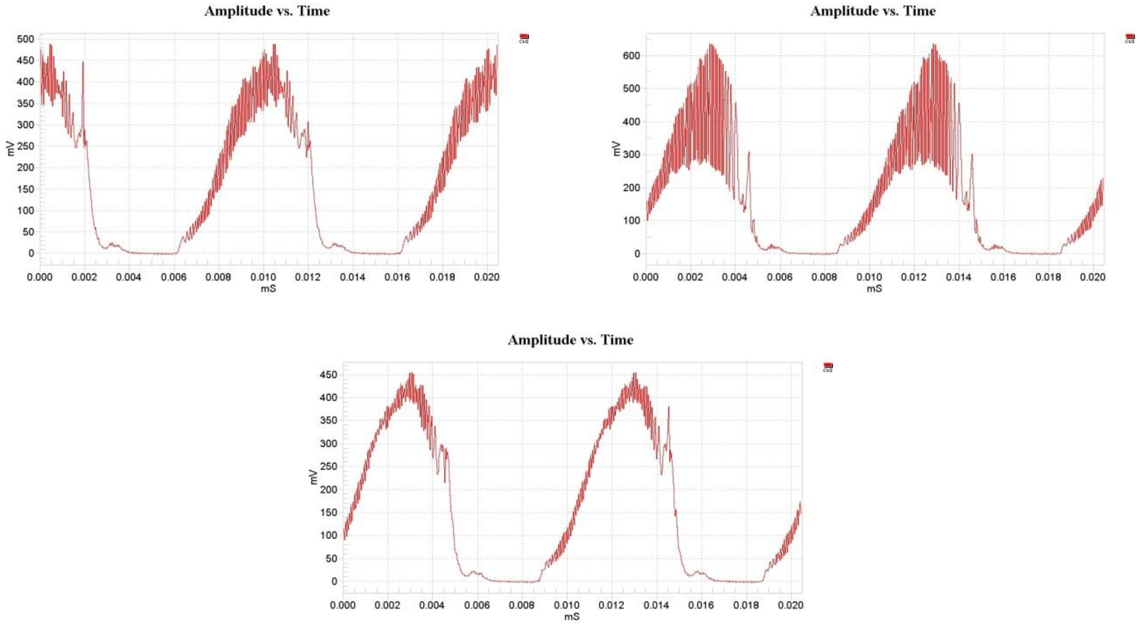

Graphic 20 - Three interferograms for different position within the target acquired using DAQ board.

In all the graphics presented above it is clearly visible that at every 10 microseconds the signal is repeated, which is consistent with the typical 100 KHz swept frequency from *Axsun* engine.

Graphic 21 shows that the laser is turned on for more than 5 microseconds and the clock signal is unstable. The frequency difference within the clock signal is not noticeable, but the next figures are photographs taken from an oscilloscope which clarify the frequency for both regions of the clock.

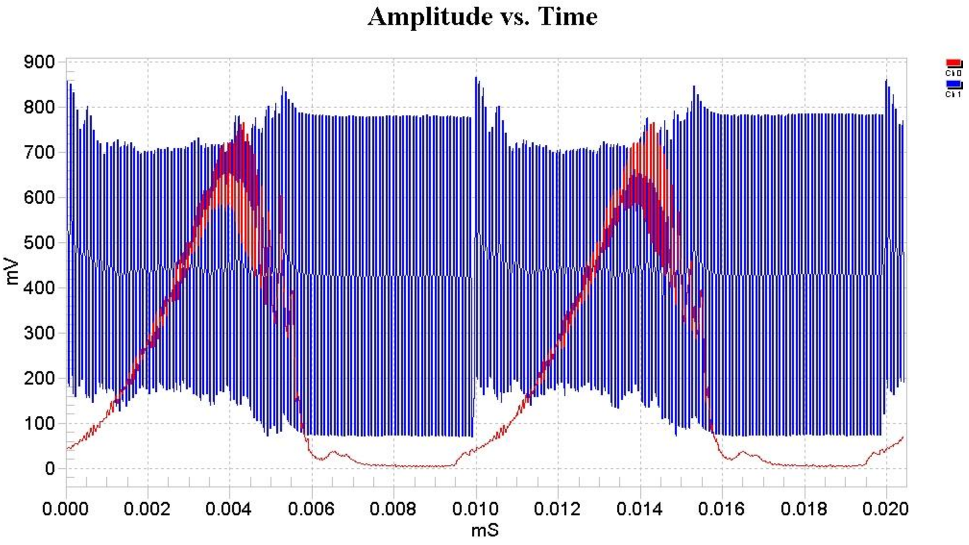

Graphic 21 – Acquired *Axsun* clock signal (blue) and interference signal (red), using DAQ Board

Figure 28 shows the region of the clock signal near the end of one period. It is clear that the clock's frequency during the cycle is not constant, mainly in the final nanoseconds.

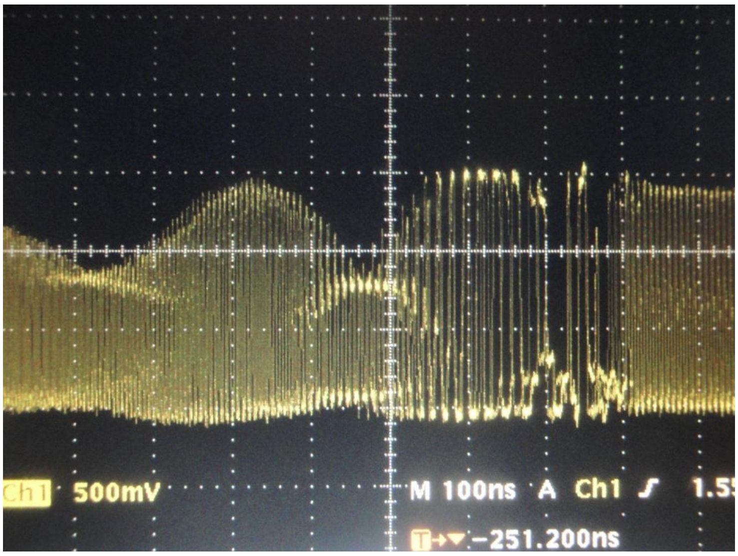

Figure 28 – *Axsun* clock signal at the end of the period

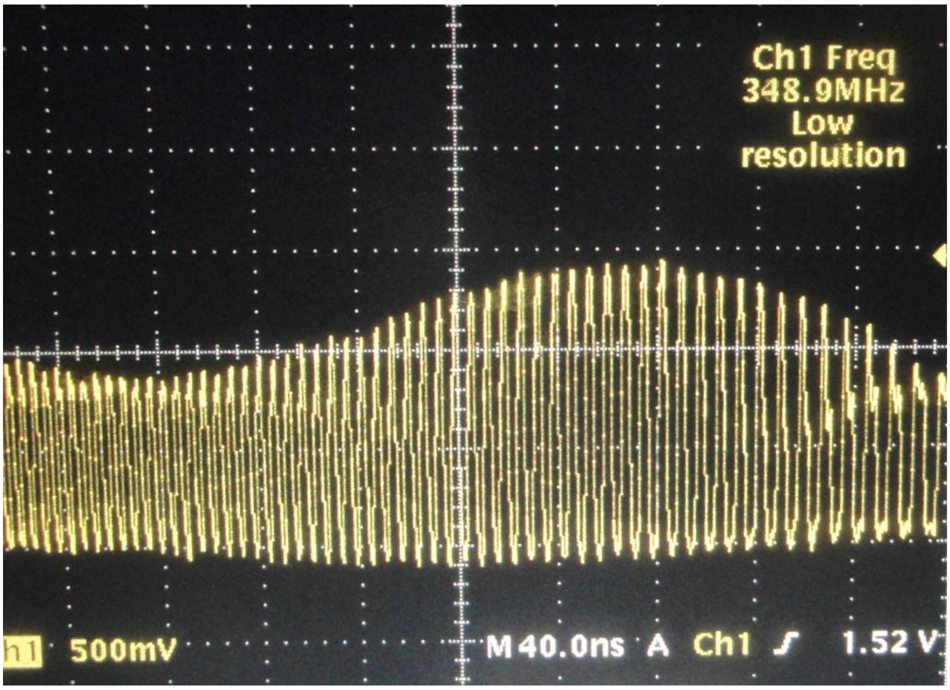

Figure 29 – *Axsun* clock signal where the laser is turned on

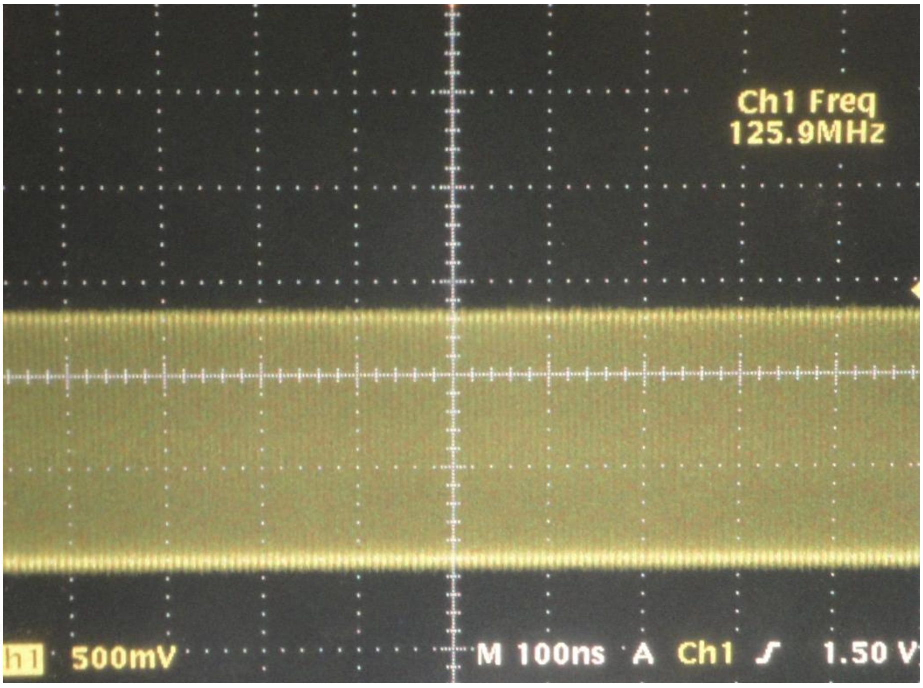

Figure 30 – *Axsun* clock signal where the laser is turned off

The two figures above show two regions of the clock signal. The first one, Figure 29, is a region of the duty cycle, where the clock reaches is maximum frequency, near 350 MHz. Unlike, Figure 30 is not from duty cycle, but from the region where the laser is turned off and the clock signal is constant with a frequency of 125 MHz.

To generate a B-scan, we acquired several consecutive A-scans, changing the beam incidence spot on the target along one direction, by using the corresponding micrometer, and then conjugated them, using a simple script on Matlab. We tried to rotate the micrometer screw only a few micrometers and to keep this value constant, but it proved to be a difficult task to perform manually.

Graphic 22 represents a B-scan of Spectralis test target. It is a conjugation of 28 consecutive A-scans (see appendix C). The depth information is visible along the x-axis. However the axes' scales do not represent any physical information. We just built this image in order to demonstrate the potential of our bench system to obtain a B-scan.

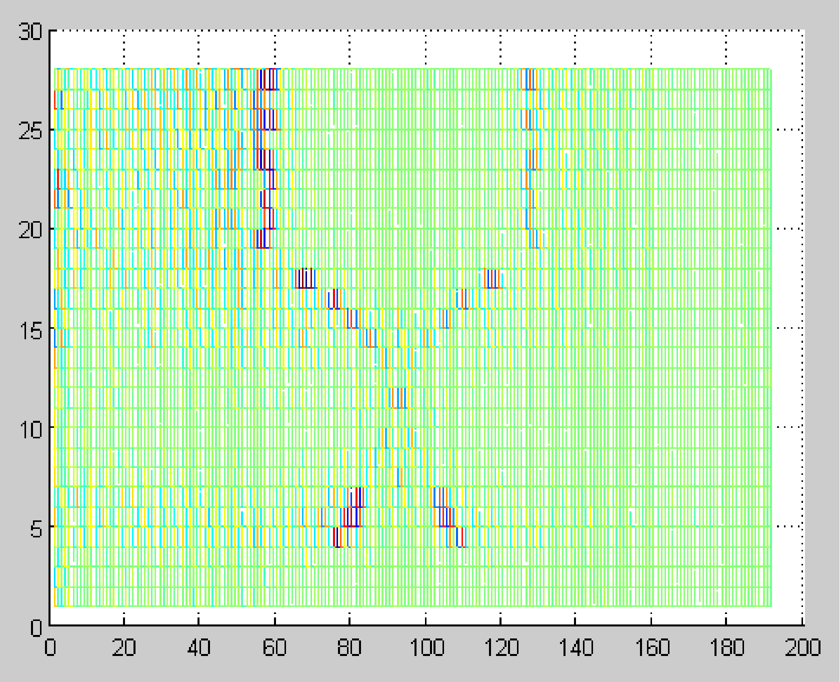

Graphic 22 – B-scan obtained using the Spectralis test target

5.1.2 Galvo System tests

We tested the position control of the galvo scanners using either square or sinusoidal waves. We also measured the maximum scanning angle.

First, we studied the frequency influence of both wave types. To perform this test we generated a wave with 10 V of amplitude and a frequency of 1 Hz. The scanning range is equal for both waves. However, while the transition between the up and down scanning limit using a sinusoidal wave is visible, for the square type we only see the laser spot at the up end and one second later the spot appears on the down limit. This phenomenon occurs because the form of the two wave types, represented in Graphic 23.

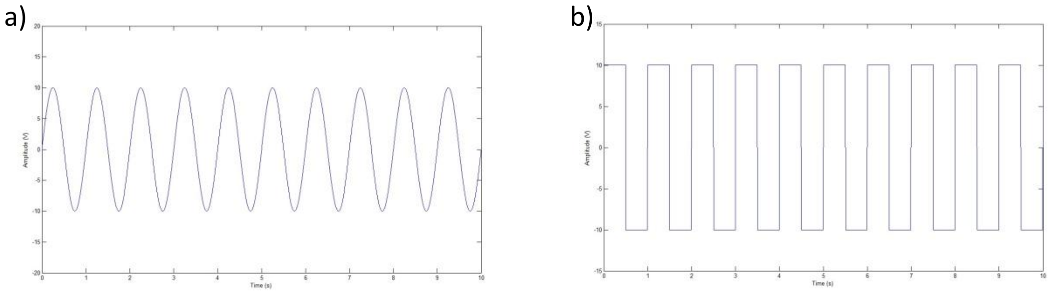

Graphic 23 – Sinusoidal (a) and square (b) waves

With the increase of wave frequency the transition between the extremes of the scanning range is faster. For frequencies higher than 40 Hz the sweep is imperceptible and we can only figure the scanning line (Y direction), clearly visible in Figure 31.

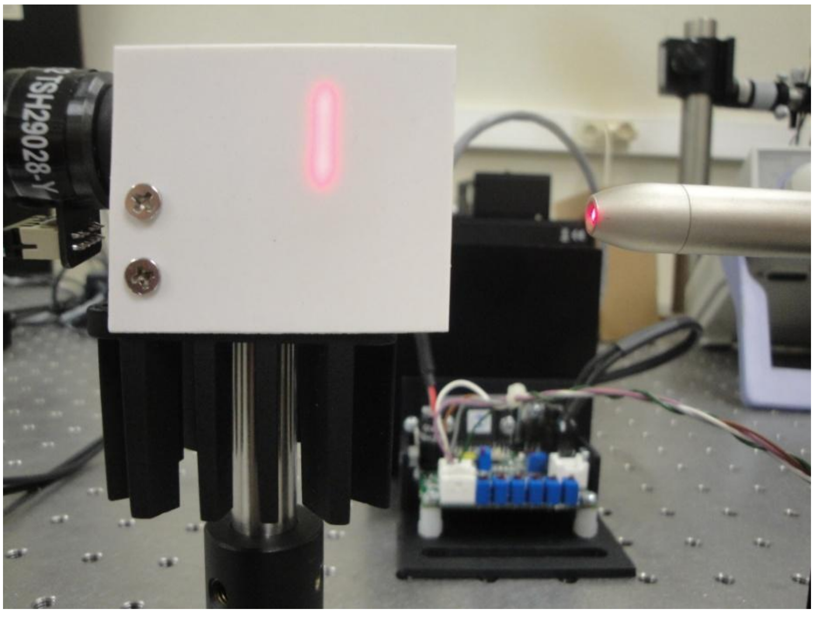

Figure 31 – Detailed of the scanning line in the Y direction

Second, we saw how wave amplitude governs the scanning position. We generated a wave with a constant frequency of 100 Hz and verified that the scanning range changes proportionally to wave's amplitude. It is wide for higher amplitudes, maximum for 10 V and narrow for smaller amplitude. Figure 32 and Figure 33 show the relation between the scanning range and wave's amplitude.

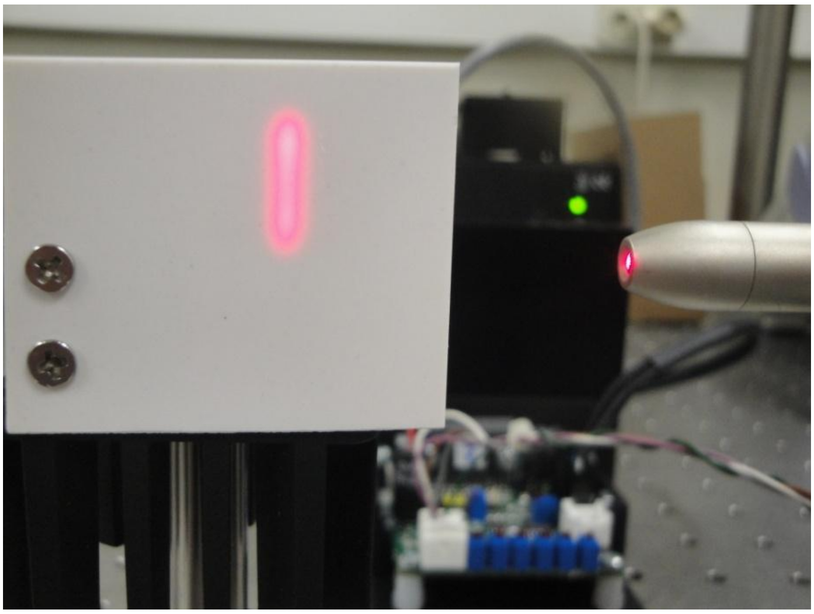

Figure 32 – Scanning line for an amplitude of 10 V

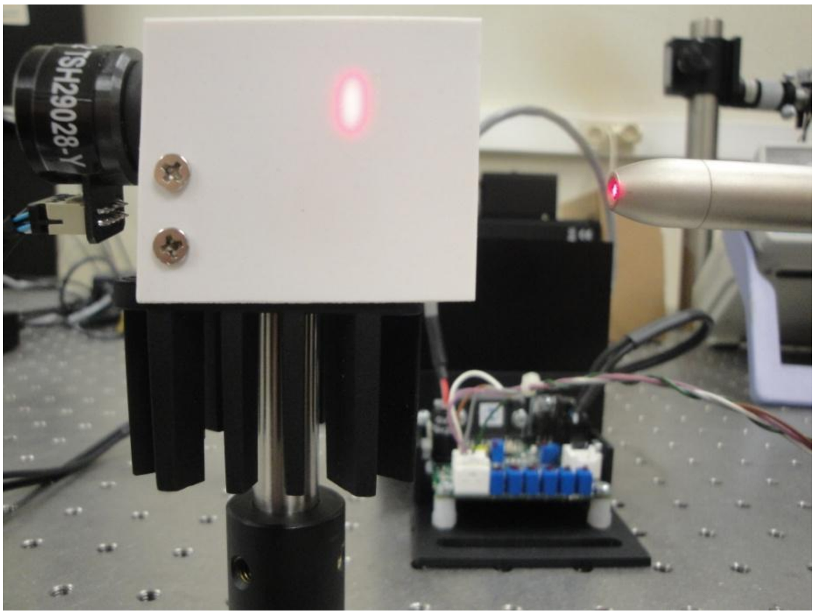

Figure 33 – Scanning line for an amplitude of 5 V

The scanning range is related to the scanning angle of the galvo system. We used the diagram represented in Figure 34 to calculate the scanning angle. The distance I is the laser projection after exiting the scanners (scanning range); d is the distance between the mirrors and the projection screen; and θ is the scanning angle.

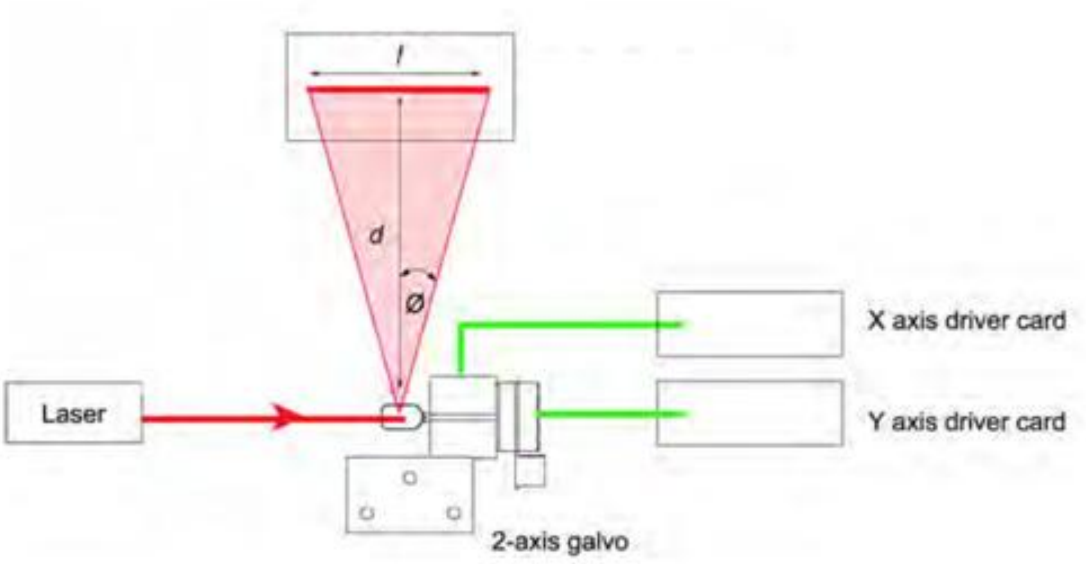

Figure 34 – Galvo system schematics

We tested the scanning angle for both waves' amplitude, 10V (maximum) and 5V. In Table 6 are listed the measurements of laser spot size and distance I for an amplitude of 10V and 5V.

Table 6 – Scanning range (I)

Laser spot size (mm)	10 V (mm)	5 V (mm)
4,48	7,71	4,49
4,27	7,80	4,76
4,39	7,73	4,10
4,23	8,14	4,43
4,16	8,06	4,29
4,59	7,70	4,44
4,21	7,33	3,80
4,14	7,26	4,96
	Mean	
4,31	7,72	4,41

Using basic trigonometry, the scanning angle is given by:

$$I = 2d \tan\theta \Leftrightarrow \theta = \tan^{-1}\left(\frac{I}{2d}\right)$$

Since the laser spot is very large and it is difficult to measure the right dimension of the scanning line, we assumed reasonable that the error associated corresponds to half of the spot size. Thus the scanning line for an amplitude of 10V is 7,72 ± 2,16 mm and 4,41 ± 2,16 mm with 5V. Therefore the scanning angle is 13,6 ± 3,9 degrees and 7,90 ± 3,9 degrees for 10V and 5V respectively. Unfortunately, we could not perform more rigorous measurements. Our results are confirmed by data sheet which indicates that the scaling factor corresponds to 1 °/V (see Appendix A, JP7 jumper).

Chapter Six

6.1 Future Work

At the end of the first year of the project, we had the main components, either electronic or optical. We also made some initial tests of the equipment. However, there is still much work to be done in order to obtain an operational OCT system useful in biomedical investigation with small animals.

Since this project is to be continued, it is necessary to make some improvements not only in instrumentation, but also on the DAQ board, mainly about its programming and data processing.

6.1.1 Instrument Optimization

Since the project time was limited, we did not perform bench trials to evaluate the system performance. So for future work it is crucial to test our bench system and assess the main parameters in order to create a data sheet for the final OCT system. Important details must be confirmed and specified, such as axial and lateral resolution, axial scan rate, average output power and sensitivity.

Regarding the scanning mirrors, we only checked the received equipment and made the early tests in order to get a better understand about its operation. So in the future it will be necessary to modify the sample arm to include the galvo system.

The sample arm will have to suffer modifications, since we only performed tests on an inanimate target and the project objective was to collect images from small animals' eyes. For this purpose, some kind of platform for small animals has to be mounted on the system to support small animals during the exams. The beam alignment should be also improved to get a better stability, in order to reduce the motion artifacts and allow a better control of the focus system.

6.1.2 Acquisition board programming and data processing

Since *Innovative Integration* DAQ board has two digital to analog and two analog to digital converters, it will play an important role in controlling the acquired data and the scanning mirrors. Both scanning and acquisition rates are closely related to the implemented programs on the acquisition board.

To acquire the detected signal we used an example program from *Innovative Integration* (Snap Example) which allows the acquisition of an A-scan at a time. Once it is desired to obtain an OCT image, for future work the DAQ board program must be modified. The program should allow the acquisition of an entire B-scan. To achieve this, a cycle has to be implemented on the acquisition board, Figure 35:

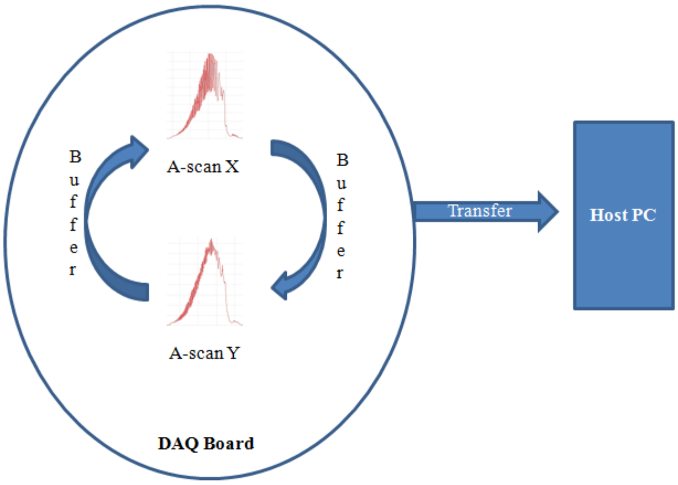

Figure 35 – Acquisition cycle of DAQ board

In order to synchronize the acquisition rate, the trigger for start the data acquisition comes from the swept source, so at each 10 µs (100 kHz swept rate) a new A-scan is acquired.

When the scanning system is implemented in the sample arm, the servo board from the galvo system will be controlled by the DAQ board also. To allow this communication it will be necessary to expand the program capabilities to generate a sine or a square wave. The resulting wave must have a specific form in order to move the beam to the desired position within the sample. The wave frequency is a crucial feature, because it will influence the scanning rate, which must be equal to the acquisition rate and swept rate.

After acquiring all scans, a Fourier Transform has to be applied, since the acquired signals are interferograms which need to be converted to space domain in order to get the depth information. At the end of this year a simple *MATLAB* script was developed to perform the post processing of data. For future work it is convenient to improve it. If possible, it will be very helpful to make processing automatically, at real time.

We admit that when *in vivo* studies begin more problems will appear. In order to resolve them, new equipment will have to be bought or it will be necessary to modify the actual system configuration. However, we expect that the final OCT configuration will be similar to the one represented on Figure 36.

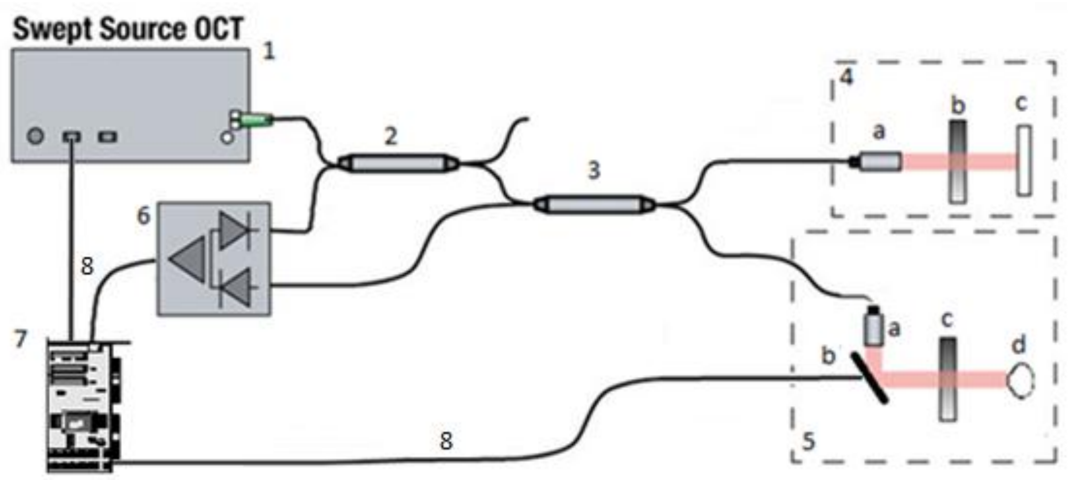

Figure 36 – Final OCT configuration

1. Swept Source
2. 90:10 Coupler
3. 50:50 Coupler
4. Reference Arm:
    a. Collimator
    b. Lens
    c. Gold Mirror
5. Sample Arm:
    a. Collimator
    b. Scanning System
    c. Lens
    d. Small animal's eye
6. Balanced Detector
7. DAQ Board
8. Electrical Wire

References

[1] A Gh Podoleanu, "Optical Coherence Tomography," *The British Journal of Radiology*, vol. 78, pp. 976–988, November 2005.

[2] C. Crosby Sean, "Optical Coherence Tomography," The University of Melbourne, Honours Report for Bachelor of Science degree 2003.

[3] James G. Fujimoto, , E. Bouma Brett and J. Tearney Guillermo, Eds.: Marcel Dekker, Inc., 2002, ch. one.

[4] Peter H. Tomlins and R. K. Wang, "Theory, developments and applications of optical coherence tomography," *Journal of Physics*, vol. 38, pp. 2519–2535, 2005.

[5] Hising Wen Wang, Joseph A. Izatt, and Manish D. Kulkarni, , Brett E. Bouma and Guillermo J. Tearney, Eds.: Marcel Dekker, Inc, 2002, ch. 10.

[6] Peter Van Osta. Basics of Microscopy. [Online]. http://www.vanosta.be/microscopy.htm

[7] A F Fercher, W Drexler, C K Hitzenberge, and T Lasser, "Optical coherence tomography—principles and applications," *Reports on Progress in Physics*, vol. 66, pp. 239–303, 2003.

[8] D. Merino, A. Bradu, C. Daintya, and A. Podoleanub, "Improvement of in-vivo en-face OCT retinal images using adaptive optics," in *5th International Workshop on Adaptive Optics for Industry and Medicine*, Beijing, China, 2005.

[9] Sergio Ortiz, Damian Siedlecki, Laura Remon, and Susana Marcos, "Optical coherence tomography for quantitative surface topography," *Appiled Optics*, vol. 48, pp. 6708-6715, December 2009.

[10] Sergio Ortiz et al., "Optical distortion correction in Optical Coherence Tomography for quantitative ocular anterior segment by three-dimensional imaging," *Optics Express*, vol. 18, pp. 2782-2796, February 2010.

[11] Alkhazur Manakov, Hans Peter Seidel, and Ivo Ihrke, "A Mathematical Model and Calibration Procedure for Galvanometric Laser Scanning Systems," in *Proceedings of the Vision, Modeling, and Visualization Workshop*, Berlim, Germany, 2011.

[12] Wolfgang Drexler and James G. Fujimoto, "State-of-the-art retinal optical coherence tomography," *Progress in Retinal and Eye Research*, vol. 27, pp. 45–88, 2008.

[13] Zahid Yaqoob, Jigang Wu, and Changhuei Yang, "Spectral domain optical coherence tomography: a better OCT imaging strategy," *BioTechniques*, vol. 39, pp. 6-13, December 2005.

[14] Michael A. Choma, Changhuei Yang, and Joseph A. Izatt, "Instantaneous quadrature low-

coherence interferometry with 3 x 3 fiber-optic couplers," *Optics Express*, vol. 28, pp. 2162-2164, November 2003.

[15] Michael A. Choma, Marinko V. Sarunic, Changhuei Yang, and Joseph A. Izatt, "Sensitivity advantage of swept source and Fourier domain optical coherence tomography," *Optics Express*, vol. 11, pp. 2183-2189, September 2003.

[16] Johannes F. de Boer et al., "Improved signal-to-noise ratio in spectral-domain compared with time-domain optical coherence tomograohy," *Optics Express*, vol. 28, pp. 2067-2069, November 2003.

[17] Peter H. Tomlins and R. K. Wang, "Theory, developments and applications of optical coherence tomography," *JOURNAL OF PHYSICS D: APPLIED PHYSICS*, vol. 38, pp. 2519–2535, 2005.

[18] Joel S. Schuman, "Spectral Domain Optical Coherence Tomography for Glaucoma," *Transactions of the American Ophthalmological Society*, vol. 106, pp. 426-458, December 2008.

[19] HrebeshMolly Subhash, "Full-Field and Single-Shot Full-Field Optical Coherence Tomography: A Novel Technique for Biomedical Imaging Applications," *Advances in Optical Technologies*, vol. 2012, pp. 1-26, December 2011.

[20] Yuuki Watanabe and Manabu Sato, "Three-dimensional wide-field optical coherence tomography using an ultrahigh-speed CMOS camera," *Optics Communications*, vol. 281, pp. 1889–1895, 2008.

[21] Victor XD Yang and I. Alex Vitkin, "Principles of Doppler OCT," in *Optical Coherence Tomography in Cardiovascular Research*, Evelyn Regar, Ton Leeuwen, and Patrick Serruys, Eds.: Taylor and Francis Medical, 2007, ch. 32.

[22] Thorlabs. Thorlabs - Polarization Sensitive OCT. [Online]. http://www.thorlabs.com/NewGroupPage9.cfm?ObjectGroup_ID=4406

[23] N. J. Kemp et al., "Polarization Sensitive OCT Imaging of the Primate Retinal Nerve Fiber Layer," in *Second Joint EMBSBMES Conference*, Houston, TX, USA, 2002, pp. 1204-1205.

[24] Erich Götzinger et al., "Three-dimensional polarization sensitive OCT imaging and interactive display of the human retina," *Optics Express*, vol. 17, pp. 4151-4165, March 2009.

[25] A.F Fercher, K. Mengedoht, and W. Werner, "Eye length measurement by interferometer with partially coherent light," *Optics Letters*, vol. 13, pp. 186-188, March 1988.

[26] A.F. Fercher, C. K. Hitzenberger, G. Kamp, and S. Y. El-Zaiat, "Measurement of intraocular distances by backscattering spectral interferometry," *Optics Communications*, vol. 117,

pp. 43-48, May 1995.

[27] S. H. Yun, G. J. Tearney, J. F. de Boer, N. Iftimia, and B. E. Bouma, "High-speed optical frequency-domain imaging," *Optics Express*, vol. 11, pp. 2953-2963, November 2003.

[28] Brian R. White et al., "In vivo dynamic human retinal blood flow imaging using ultra-high-speed spectral domain optical Doppler tomography," *Optics Express*, vol. 11, pp. 3490-3497, December 2003.

[29] Maciej Wojtkowski et al., "Ultrahigh-resolution, high-speed, Fourier domain optical coherence tomography and methods for dispersion compensation," *Optics Express*, vol. 12, pp. 2404-2422, May 2004.

[30] A. M. Kowalevicz, T. R. Schibli, F X. Kärtner, and J. G. Fujimoto, "Ultralow-threshold Kerr-lens mode-locked Ti:Al2O3 laser," *Optics Letters*, vol. 27, pp. 2037-2039, November 2002.

[31] A. Unterhuber et al., "Compact, low-cost Ti:Al2O3 laser for in vivo ultrahigh-resolution optical coherence tomography," *Optics Letters*, vol. 28, pp. 905-907, June 2003.

[32] Philipp C. Wagenblast, Tony H. Ko, James G. Fujimoto, and Franz X. Kaertner, "Ultrahigh-resolution optical coherence tomography with a diode-pumped broadband Cr3+:LiCAF laser," *Optics Express*, vol. 12, pp. 3257-3263, July 2004.

[33] Erdem Ergun et al., "Assessment of central visual function in Stargardt's disease/fundus flavimaculatus with ultrahigh-resolution optical coherence tomography," *Investigative Ophthalmology & Visual Science*, vol. 46, pp. 310-316, January 2005.

[34] Gadi Wollstein et al., "Ultrahigh-Resolution Optical Coherence Tomography in Glaucoma," *Ophthalmology*, vol. 112, pp. 229-237, February 2005.

[35] B. Považay et al., "Enhanced visualization of choroidal vessels using ultrahigh resolution ophthalmic OCT at 1050 nm," *Optics Express*, vol. 11, pp. 1980-1986, August 2003.

[36] A. Unterhuber et al., "In vivo retinal optical coherence tomography at 1040 nm - enhanced penetration into the choroid," *Optics Express*, vol. 13, pp. 3252-3258, May 2005.

[37] Christoph K. Hitzenberger, Peter Trost, Pak-Wai Lo, and Qienyuan Zhou, "Three-dimensional imaging of the human retina by high-speed optical coherence tomography," *Optics Express*, vol. 11, pp. 2753-2761, October 2003.

[38] Ursula Schmidt-Erfurth et al., "Three-Dimensional Ultrahigh-Resolution Optical Coherence Tomography of Macular Diseases," *Investigative Ophthalmology & Visual Science*, vol. 46, pp. 3393-3402, September 2005.

[39] B K Monson et al., "High-speed, ultra-high-resolution optical coherence tomography of acute macular neuroretinopathy," *British Journal of Ophthalmology*, vol. 91, pp. 119-120, January 2007.

[40] R. Huber, M. Wojtkowski, K. Taira, J. G. Fujimoto, and K. Hsu, "Amplified, frequency swept lasers for frequency domain reflectometry and OCT imaging: design and scaling principles," *Optics Express*, vol. 13, pp. 3513-3528, May 2005.

[41] V. J. Srinivasan et al., "High-speed, high-resolution optical coherence tomography retinal imaging with a frequency-swept laser at 850 nm," *Optics Letters*, vol. 32, pp. 361-363, February 2007.

[42] X. J. Wang, T. E. Milner, and J. S. Nelson, "Characterization of fluid flow velocity by optical Doppler tomography," *Optics Letters*, vol. 20, pp. 1337-1339, June 1995.

[43] R. A. Leitgeb et al., "Real-time assessment of retinal blood flow with ultrafast acquisition by color Doppler Fourier domain optical coherence tomography," *Optics Express*, vol. 11, pp. 3116-3121, November 2003.

[44] J.F. de Boer et al., "Determination of the depth resolved Stokes parameters of light backscattered from turbid media using tomography," in *Lasers and Electro-Optics Conference*, vol. 24, May 1999.

[45] Christoph K. Hitzenberger, Erich Götzinger, Markus Sticker, Michael Pircher, and Adolf F. Fercher, "Measurement and imaging of birefringence and optic axis orientation by phase resolved polarization sensitive optical coherence tomography," *Optics Express*, vol. 9, pp. 780-790, December 2001.

[46] Martin Gloesmann et al., "Histologic Correlation of Pig Retina Radial Stratification with Ultrahigh-Resolution Optical Coherence Tomography," *Investigative Ophthalmology & Visual Science*, vol. 44, pp. 1696-1703, April 2003.

[47] Elisabeth M. Anger et al., "Ultrahigh resolution optical coherence tomography of the monkey fovea. Identification of retinal sublayers by correlation with semithin histology sections," *Experimental Eye Research*, vol. 78, pp. 117-1125, 2004.

[48] Peter K. Ahnelt and Wolfgang Drexler, "Comment on 'Ultrahigh resolution optical coherence tomography of the monkey fovea. Identification of retinal sublayers by correlation with semithin histology sections' by E.M. Anger et al. [Exp. Eye Res. 78 (2004) 1117–1125]," *Experimental Eye Research*, vol. 80, pp. 447-448, 2005.

[49] Peter K. Ahnelt and Wolfgang Drexler, "Reply to 'Comment on: Ultrahigh resolution optical coherence tomography of the monkey fovea. Identification of retinal sublayers by correlation with semithin histology sections' by E.M. Anger et al. [Exp. Eye Res. 78 (2004) 1117–1125] by Velthoven et.al.," *Experimental Eye Research*, vol. 80, pp. 449-450, 2005.

[50] Vivek J. Srinivasan et al., "Noninvasive Volumetric Imaging and Morphometry of the Rodent Retina with High-Speed, Ultrahigh-Resolution Optical Coherence Tomography," *Investive Ophthalmology and Visual Science*, vol. 47, pp. 5522-5528, December 2006.

[51] Benjamin Potsaid et al., "Ultrahigh speed 1050nm swept source /Fourier domain OCT retinal and anterior segment imaging at 100,000 to 400,000 axial scans per second," *Optics Express*, vol. 18, pp. 20029-20048, September 2010.

[52] V. F. Duma and Gh. A. Podoleanub, "Theoretical approach on a galvanometric scanner with an enhanced duty cycle," in *1st Canterbury Workshop on Optical Coherence Tomography and Adaptive Optics*, Canterbury, 2008.

[53] John Munro, *Heroes of the Telegraph*.: Project Gutenberg, 1997.

[54] OBEL Introduction to Optical Coherence Tomography (OCT). [Online]. http://obel.ee.uwa.edu.au/research/oct/intro/

[55] Welcome to Warren Group: Introduction to Tissue Imaging. [Online]. http://www.chem.duke.edu/~wwarren/tissueimaging.php

[56] Retina - Wikipedia, the free encyclopedia. [Online]. http://en.wikipedia.org/wiki/File:Gray881.png

[57] Thorlabs, GVS002 Scanning Glavo System User Guide.

Appendix A

This appendix lists all the equipment necessary to the development of our OCT system. The information is adapted from user manuals from manufacturers.

Axsun Swept Source

Table 7 - *Axsun* Engine Features:

Wavelength Range(-10dB)	980 - 1100 nm
Wavelength Center	1040 - 1060 nm
Average Output Power	Min 15mW
Sweep Rep Rate	10 - 100 kHz
Coherence Length	Min 10 nm, Typical 12 nm
Output Connector	FC/APC
Sweep Trigger Output	TTL(0 - 3,3 V) SMA connector
Clock Output	0,2 - 0,8 V SMA connector
Laser Drive	Sine or Linear
Power Input	100 – 240 VAC, 50/60 Hz
Power Consumption (~25ºC)	12 W (Laser engine alone) 40 W (with *Axsun* supplied power supply)
Mechanical Dimensions	208 x 152 x 70 mm
Weight	0.6 Kg

Signals

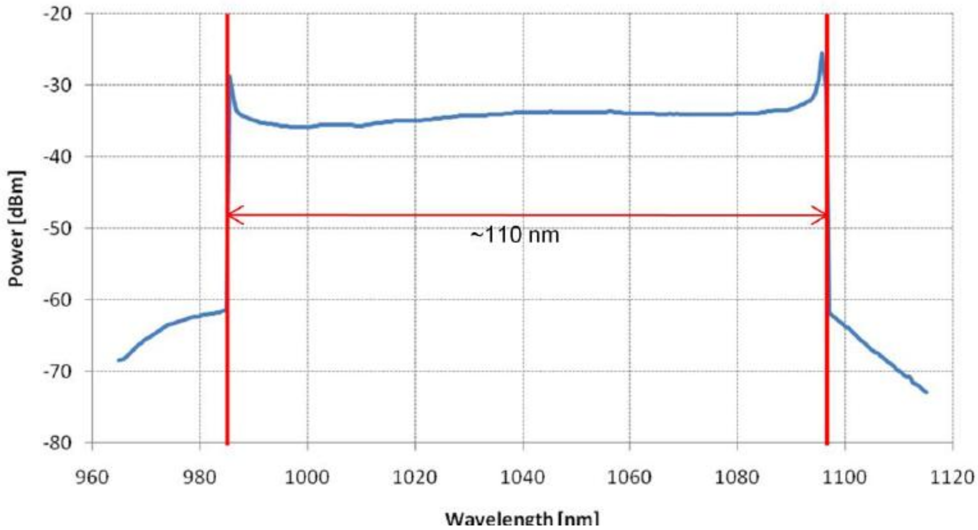

Graphic 24 – Power Spectrum of the Engine

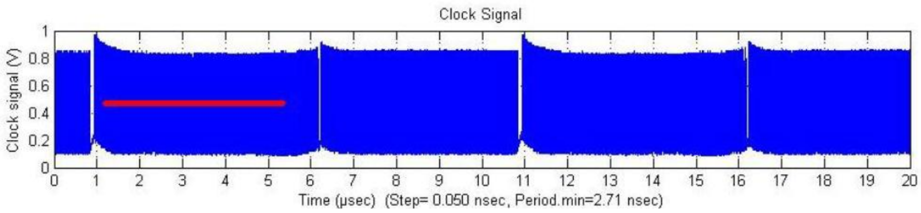

Graphic 25 - Clock output signal

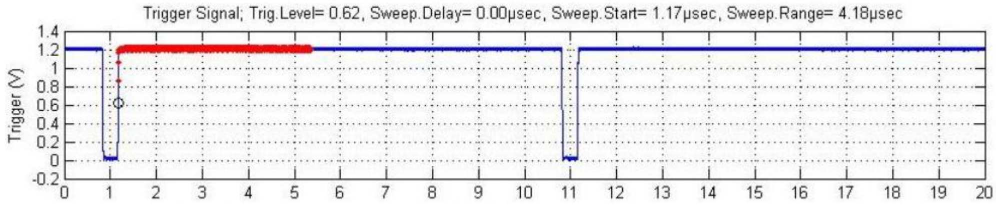

Graphic 26 - Trigger output signal

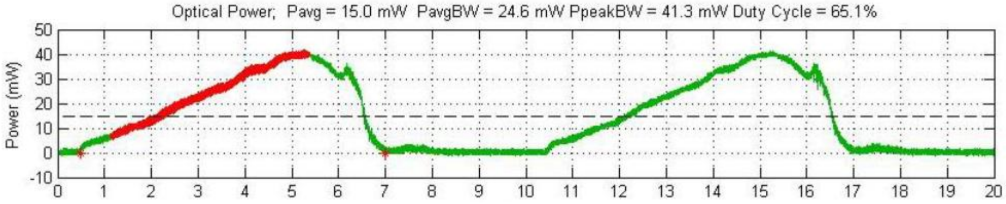

Graphic 27 - Optical power signal

Thorlabs Balanced Detector

Table 8 – PDB145C parameters

Detector Material/Type	InGaAs / PIN
Wavelength Range	800 nm - 1700 nm
Typical Max. Responsivity	1,0 A/W
Detector Diameter	0,3 mm
Bandwidth (3dB)	DC - 15 MHz
Common Mode Rejection Ratio	> 35 dB
Transimpedance Gain*	51 x 10^3 V/A
Conversion Gain RF-Output	51 x 10^3 V/W
Conversion Gain Monitor Outputs	100 V/mW @ 1550 nm
CW Saturation Power	70 µW @ 1550 nm
Optical Inputs	FC (Removable)
Max. Input Power (photodiode damage threshold))	20 mW
Electrical outputs	SMA
RF-Output Impedance	50Ω
NEP (DC-10MHz)	3,2 pW/√Hz
DC-offset RF Output	< ± 2 mV
Size	85x80x30mm
Power Supply	±12 V, 200 mA

* Transimpedance gain is reduced by factor 2 into 50 Ohm load.

(All accuracy data are given at 23 ± 5°C and 45 ±15% humidity)

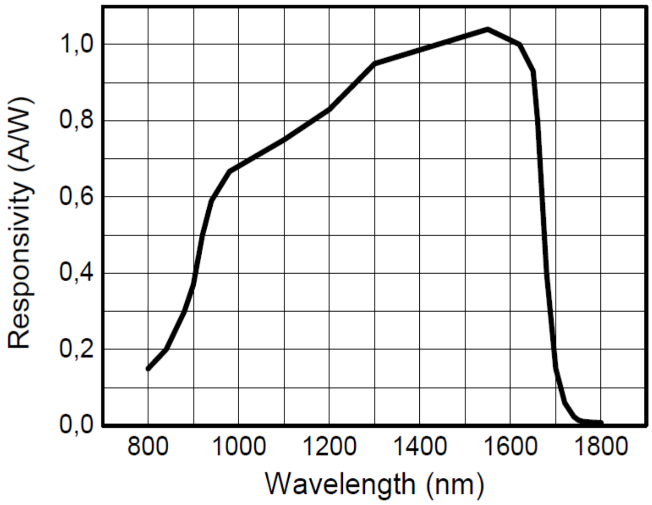

Graphic 28 – Detector responsitivity

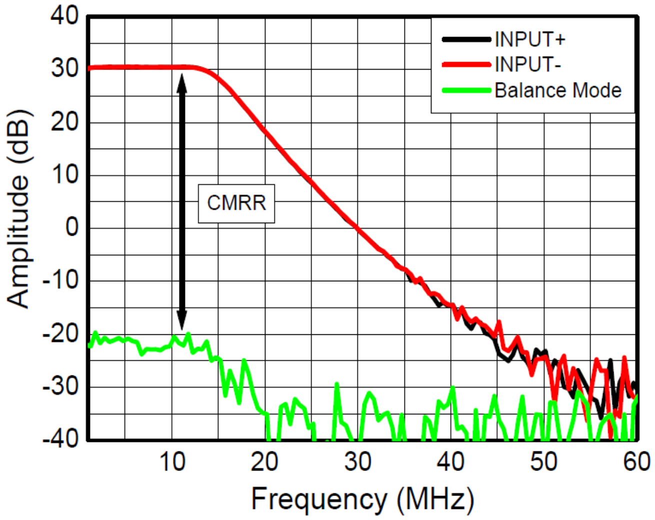

Graphic 29 – Detector frequency response

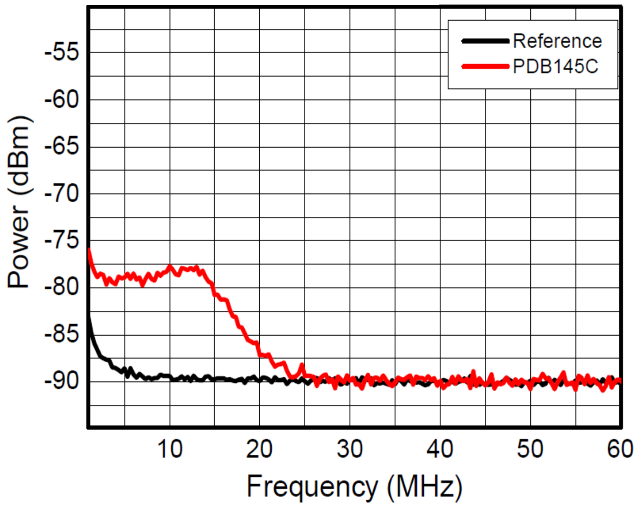

Graphic 30 – Detector spectral noise

Thorlabs Galvo System

Server Board Electric Connections

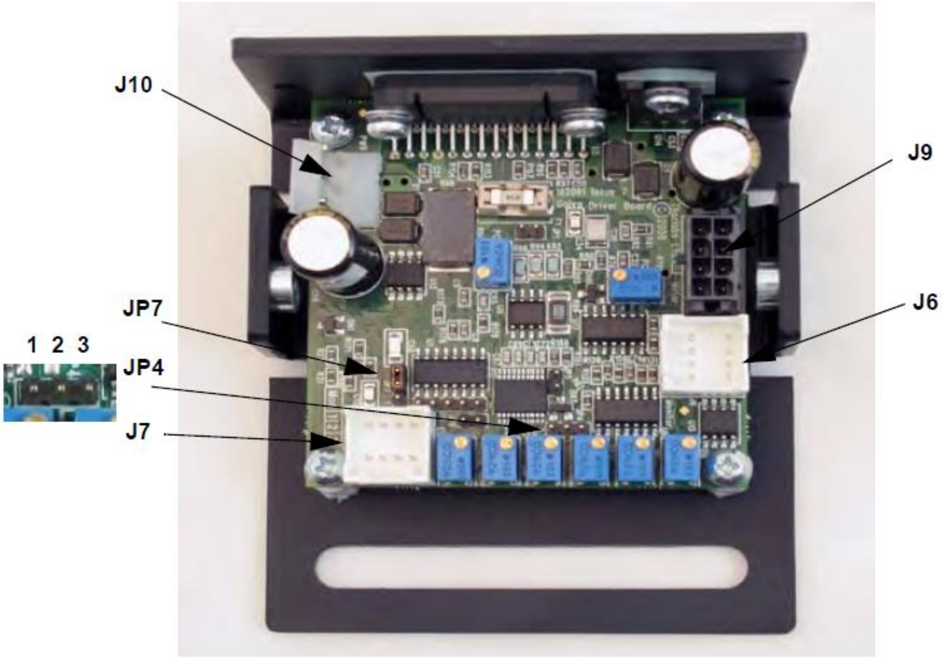

Figure 37 – Servo board

- Connector J10 is used for power supply

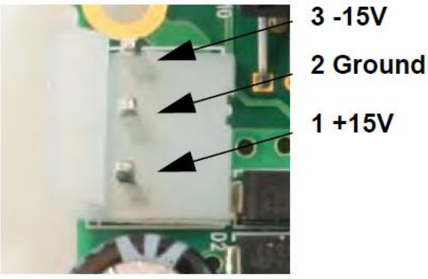

- J9 is to connect the servo board to the galvo motor. Each board has a serial number which must correspond to the motor serial number

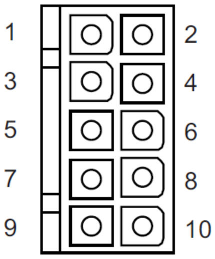

Pin 1 Motor + Coil
Pin 2
Pin 3 Motor -Coil
Pin 4 Position Sensor Cable Shield
Pin 5
Pin 6 Position Sensor Power
Pin 7
Pin 8 Position Sensor A Current
Pin 9 Position Sensor B Current
Pin 10 Position Sensor Ground

- J7 is the input connector

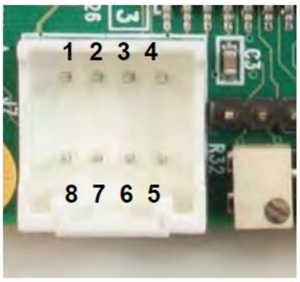

Pin 1 Command Input +ve
Pin 2 Command Input -ve
Pin 3 DRV OK
Pin 4 External Enable
Pin 5 -12V Output (low impedence O/P)
Pin 6 +12V Output (low impedence O/P)
Pin 7 Ground
Pin 8 Ground

- Connector J6 is used for diagnostic

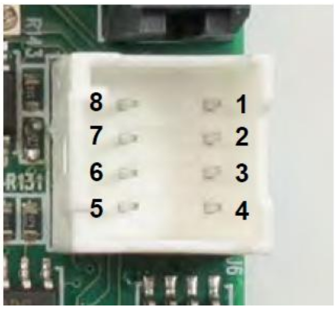

Pin 1 Scanner Position
Pin 2 Internal Command Signal
Pin 3 Positioning Error x 5
Pin 4 Motor Drive Current
Pin 5 Not Connected
Pin 6 Test Input (NC)
Pin 7 Motor + Coil Voltage / 2
Pin 8 Ground

- JP7 is a jumper to set the scaling factor

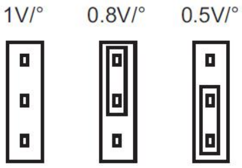

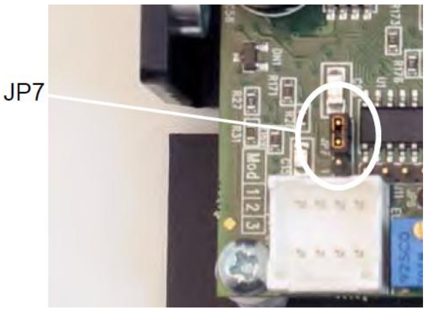

Table 9 – GVS002 Specifications

Mirror	**Maximum Beam Diameter**	5 mm
	Finish	Protected Silver Coated
	Damage Threshold	3 J/cm2at 1064 nm, 10 ns pulse
Motor and Position Sensor	**Linearity**	99.9%, range ±20°
	Scale Drift	40PPM/°C(Max)
	Zero Drift	10 µRad/°C(Max)
	Repeatability	15 µRad
	Resolution with GPS011 Linear PSU	0.0008° (15 µRad)
	Average Current	1 A
	Peak Current	5 A
	Load Mirror Aperture	5 mm
	Coil Resistance	2.2 Ω±10%
	Coil Inductance	150µH ±10%
	Rotor Inertia:	0.02gm per cm2
	Maximum Scan Angle	±12.5° (with 0.8V/° scaling factor)
	Motor Weight	50 g
	Optical Position Sensor Output Range	40 to 80 µA
Drive Electronics	**Full Scale Bandwidth**	100 Hz Square wave, 250 Hz Sinewave
	Small Angle (±0.2°) Bandwidth	1kHz
	Small Angle Step Response	300 µs
	Power Supply	+/-15V to +/-18V dc
	Analog Signal Input Resistance	20K±1%
	Position Signal Output Resistance:	1K±1%□
	Analog Position Signal Input Range	±10V
	Mechanical Position Signal Input Scale Factor	0.5V/°, 0.8V/° or 1.0V/°
	Mechanical Position Signal Output Scale Factor	0.5V/°
	Servo Board Size (L x W x H)	85 mm × 74 mm × 44 mm
Operating Temperature Range		0 ~ 40° C

Thorlabs Interferometer

Table 10 – Interferometer specifications

Wavelength Range	990 – 1100 nm
Free Spectral Range MZI Output	103,3 GHz ±5%
Fiber Type	980 - HP
Optical Input, Output	FC/APC pigtail, 50 cm
Insertion Loss*	< 1,5 dB typical 3 dB max.
Detector Material/Type	InGas/PIN
Power Monitor and MZI-Output Bandwidth (3dB)	DC – 200 MHz (3 dB)
Electrical Outputs, Impedance	SMA, 50Ω
Size	120x80x16 mm³
Power Supply	12V, 200 mA

Innovative Integration DAQ Board

Table 11 – A/D and D/A converter features

A/D		D/A	
Inputs	2	**Output**	2
Input Range	+1V to – 1V single ended for DC coupled version. +0,55V to - 0,55V for AC version	**Output Range**	+1V to -1V terminated into 50 Ω
Input Coupling	AC or DC	**Outpt type**	Single-ended DC coupled
Input Impedance	50 Ω	**Output Impedance**	50 Ω
A/D Devices	Texas Instruments ADS5474	**DAC Device**	Texas Instruments DAC5687
Sample Rate	20-400 MSPS	**DAC Resolution**	16 bit
Number of A/D Devices	2 simultaneously sampling	**DAC Sample Rate**	16MHz to 500MHz, depending on mode
Output Format	2’s complement, 14 bit	**DAC Interpolation**	Programmable 2-8x
		Data Format	2’s complement, 16 bit integer
Connectors			
SMA Female			
Calibration			
Factory calibrated. Gain and offset errors are digitally corrected in logic. Non-volatile EEPROM coefficient memory			

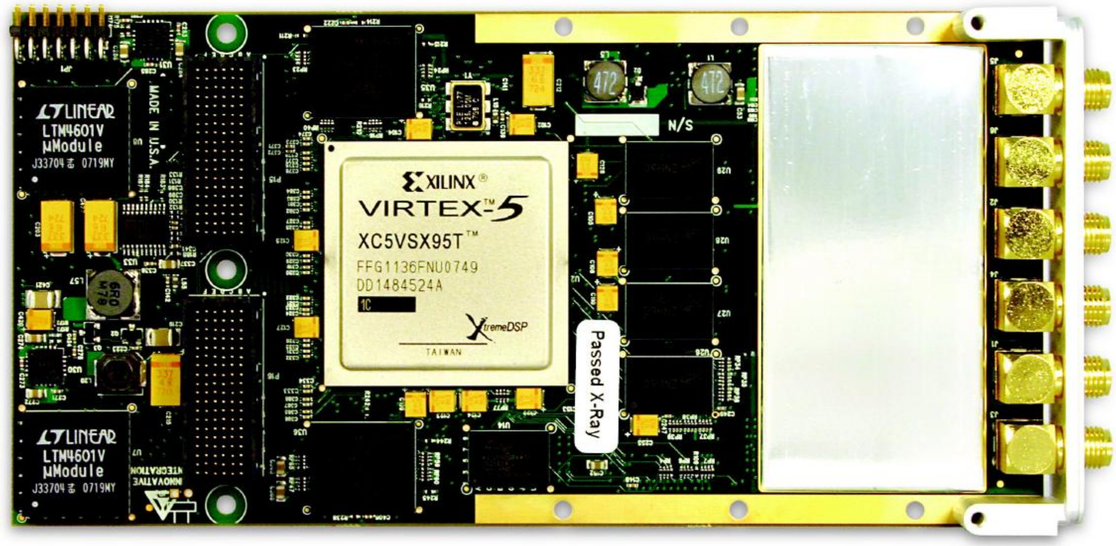

Figure 38 – X5-400M module

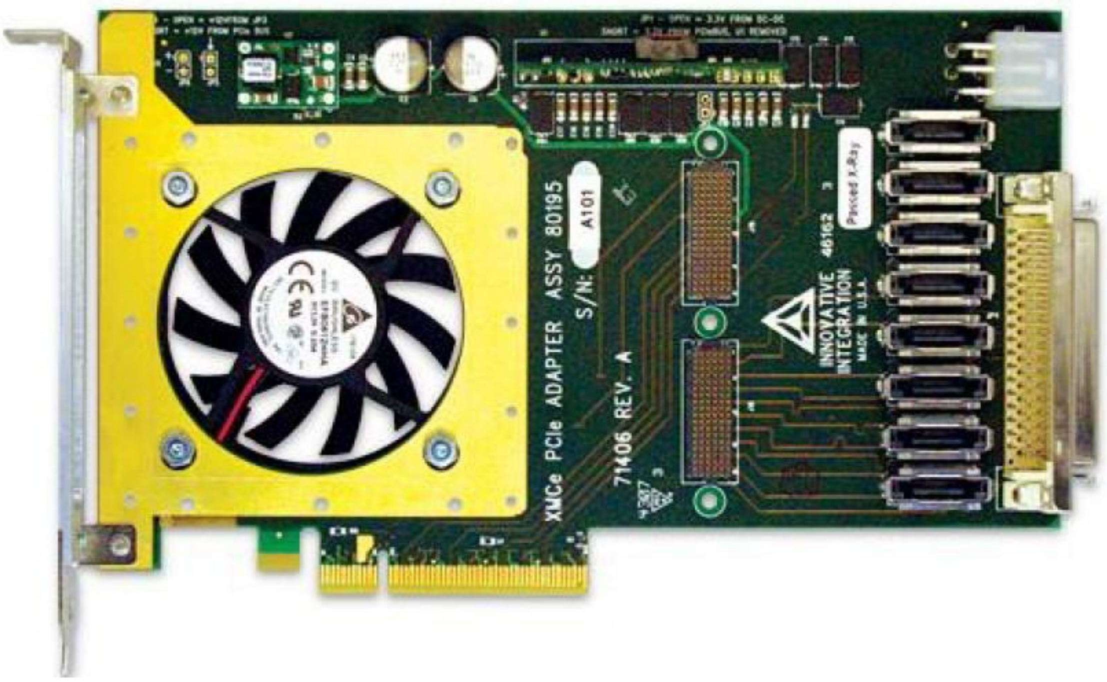

Figure 39 – Host board. Innovative x8 Lane PCI Express – XMC.3 (8x lanes) adapter card (P/N 80173-0)

Thorlabs Coupler

Fiber optic couplers are used to combine different light inputs. For example, the coupler receives two light inputs and the output beams are composed of a defined ratio of each input. A particularity of couplers is that they work in both directions.

Table 12 – Couplers features

Center Wavelength	1064 nm
Bandwidth	±15 nm
Coupling Ratio	50:50 9:10
Insertion Loss **(Coupling Ratio + Excess Loss)**	3,1 – 3,5/3,1 – 3,5 dB (50:50) 9,5 – 10,5/0,4 – 0,7 dB (90:10)
Excess Loss (Typical)	0,12 dB
PDL	<0,2 dB
Directivity	>55 dB
Operating Temperature	-40 to 85 °C

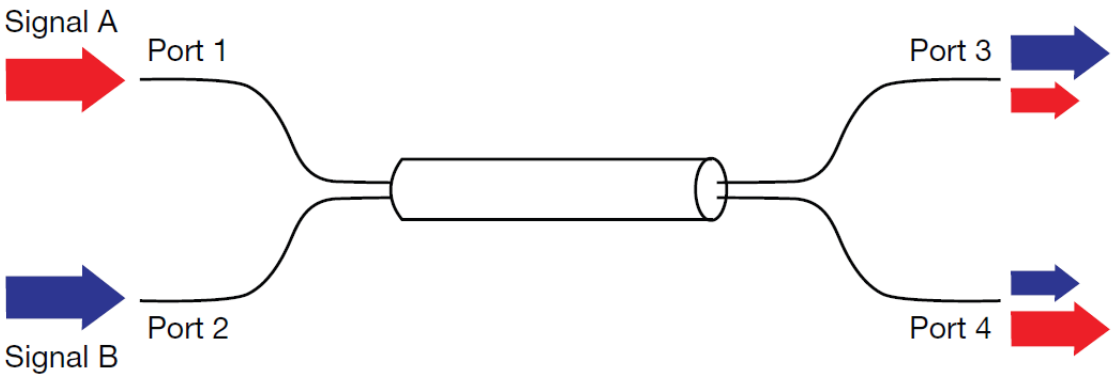

Figure 40 – 2x2 coupler schematic

Thorlabs Gold Mirror

Table 13 – Mirror Specifications

Substrate Material	Fused Silica
Clear Aperture	>90% of Diameter
Front Surface Flatness	λ/10 at 633 nm
Front Surface Quality	40-20 Scratch-Dig
Back Surface	Fine Ground
Damage Threshold	2 J/cm^2 (1064 nm, 10 ns Pulse, 10 Hz, Ø1,000 mm)
Diameter Tolerance	+0/-0,1 mm
Thickness Tolerance	±0,2 mm
Parallelism	≤3 arcmin
Chamfers	0,50 mm x 45° (Both Sides)
Coating	Protected Gold

Thorlabs Dispersion Compensators

Thorlabs' dispersion compensators are single glass compensation blocks whose glass type and thickness were chosen to match the dispersion of the scan lenses

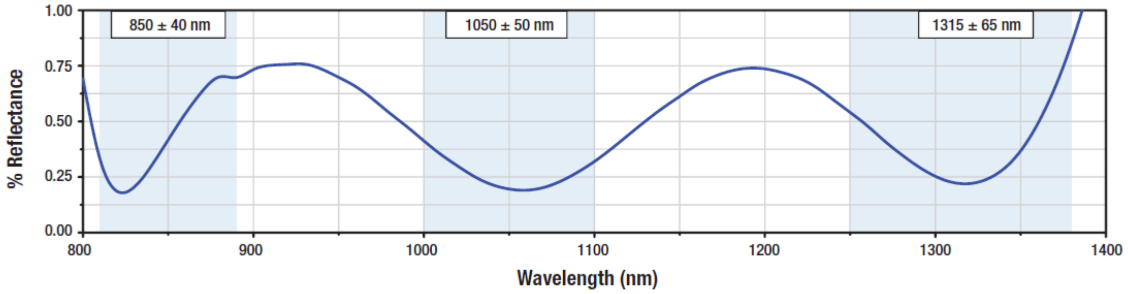

Graphic 31 – Reflectance of dispersion compensators

Table 14 – Dispersion compensators features

	LSM02DC	LSM03DC
Material	N-SF8	N-SK4
Wavelength Range	800 – 1400 nm	
Diameter	25,4 mm	
Clear Aperture	22,8 mm	
Surface Quality	40-20 Scratch-Dig	
Wavefront Error	$\lambda/4$	
Thickness Tolerance	±0,1 mm	
Diameter Tolerance	+0/-0,2 mm	

OZ Optics fiber optics

We assemble fiber optic from *OZ Optics* but it was not used on our project. It might be necessary for future work to adjust path lengths. The SMJ-3A3A-1060 - 3.6/125-3-2 single mode fiber features are shown next:

Table 15 – Fiber optic patch cord parameters

Operating Wavelength Range1 (nm)	980-1550
Cutoff Wavelength (nm)	<970
Core Diameter (µm)	6.0
Cladding Diameter (µm)	125 ± 0.5
Mode Field Diameter (µm)	5.9 ± 0.3 @980 nm 6.2± 0.3 @1060 nm
Attenuation (dB/km)	2.1 @ 980 nm 1.5 @ 1060 nm
Numerical Aperture (Manufacturer's Specs)	0.14
Effective Numerical Aperture ($1/e^2$)	0.11 @1060 nm
Connector Type	Angle PC (APC)
Jacket Diameter (mm) and Type	3mm PVC cable
Fiber Length	2 m

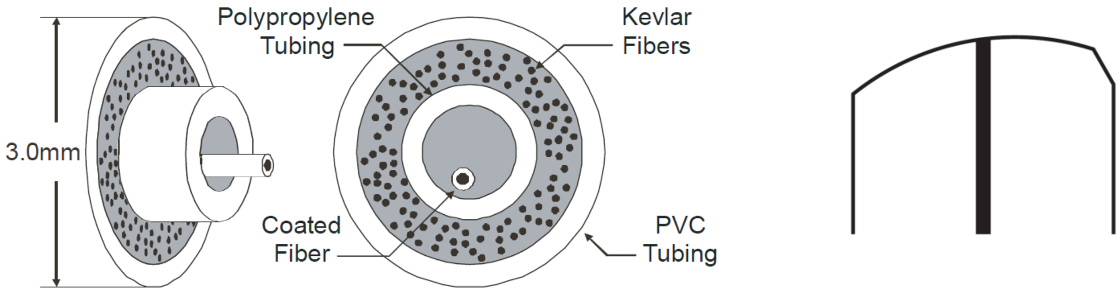

Figure 41 – Cable construction and connector finish

Appendix B

In this appendix are other photographs of our bench systems. Two photographs from OCT system and another two from galvo scanners.

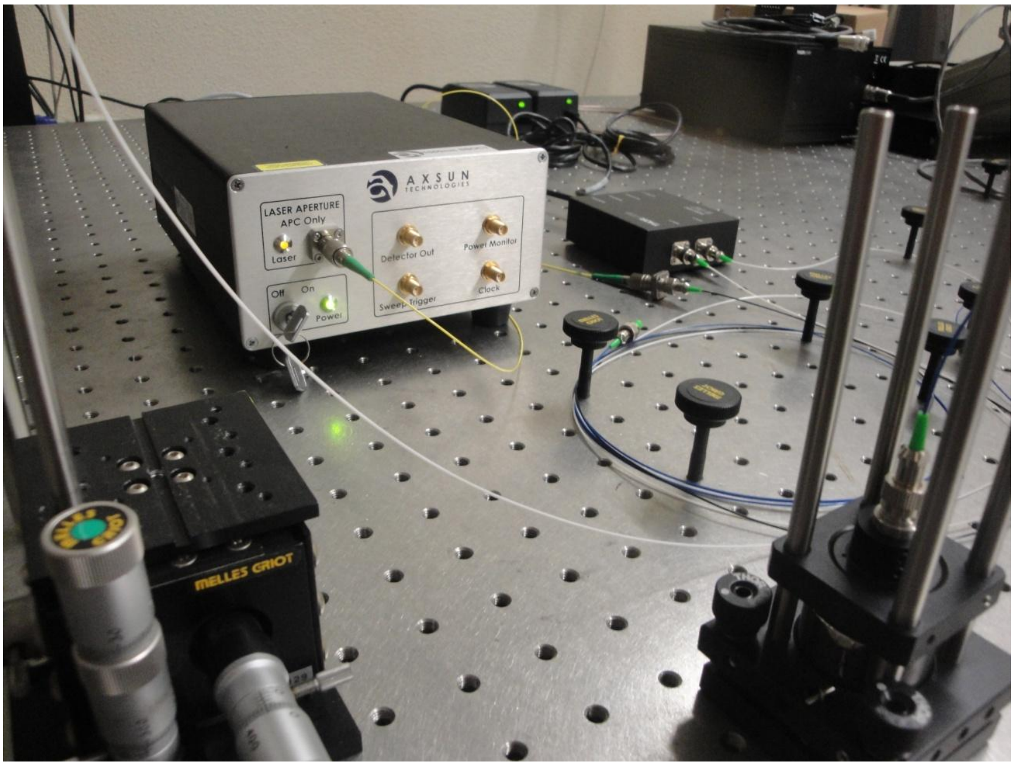

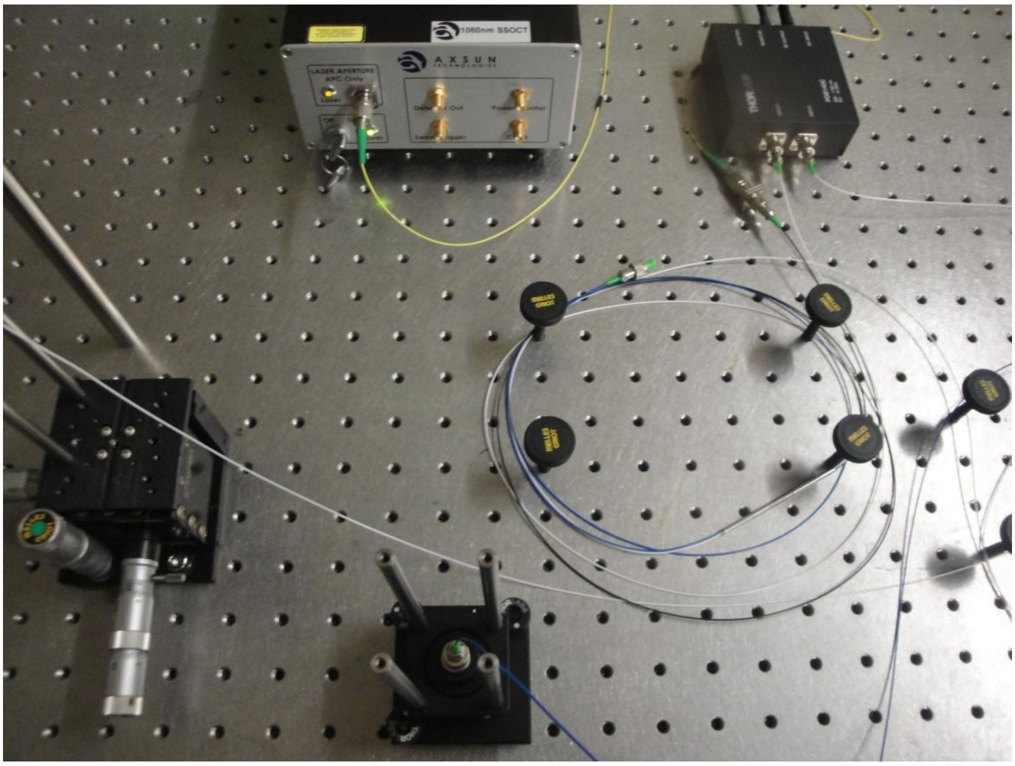

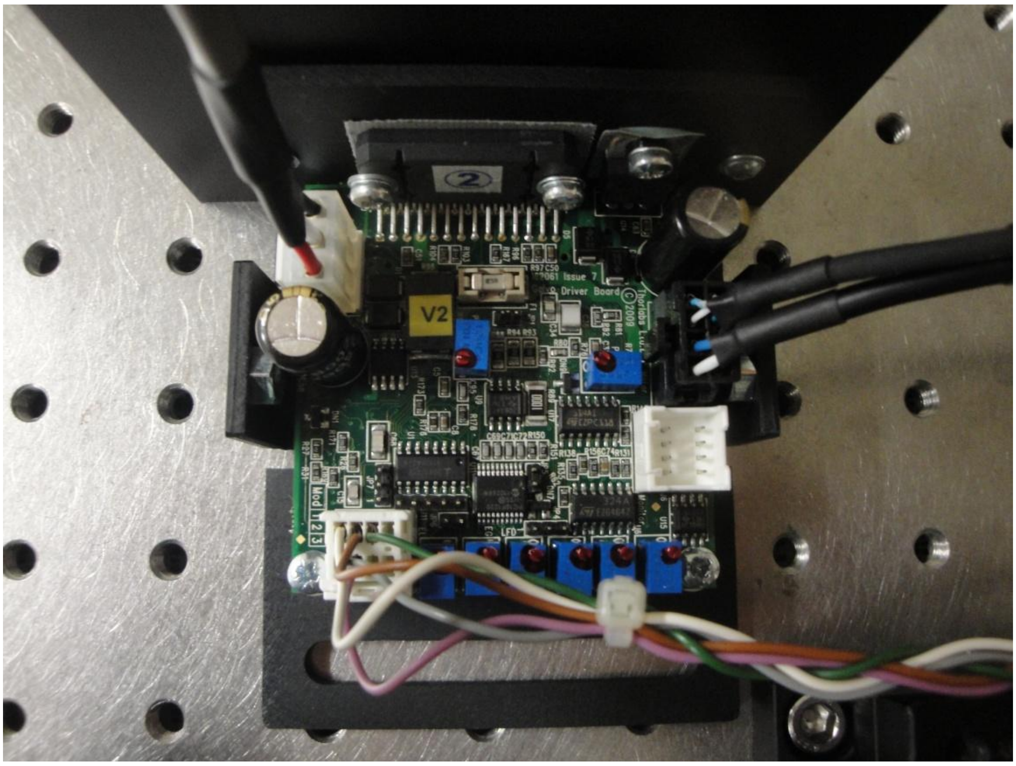

Appendix C

This appendix has all the A-scan acquired (28) and the corresponding Fourier transform in order to obtain the B-scan in Graphic 20, from chapter five.

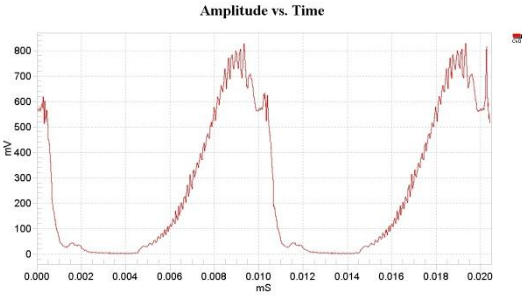

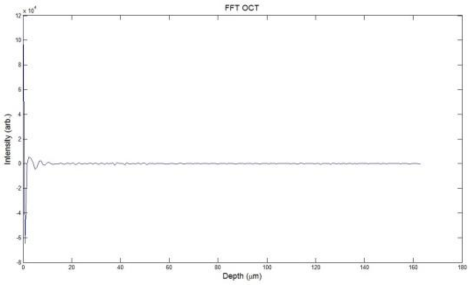

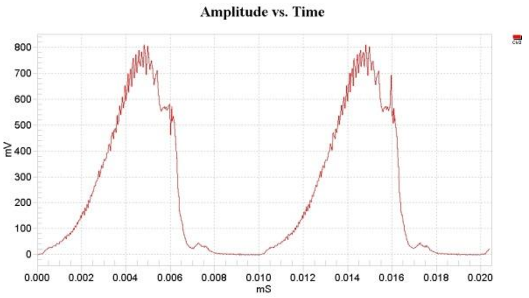

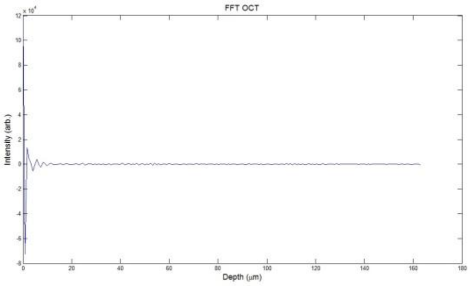

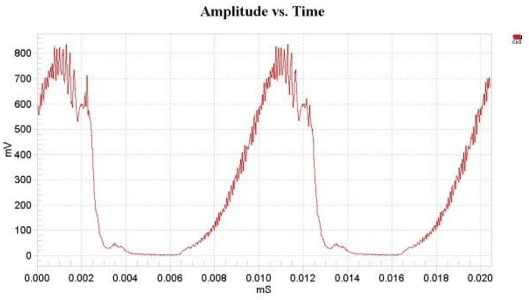

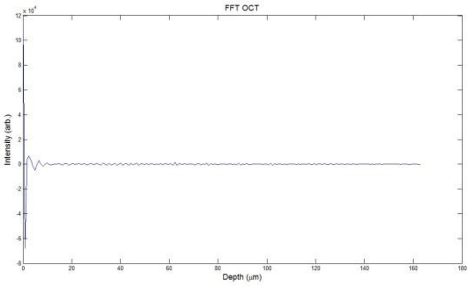

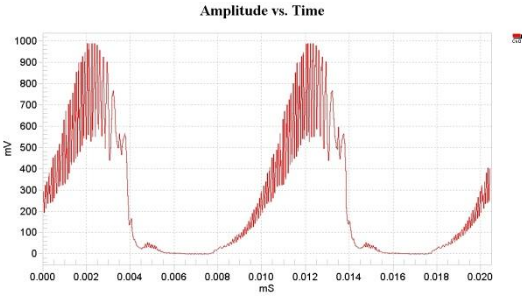

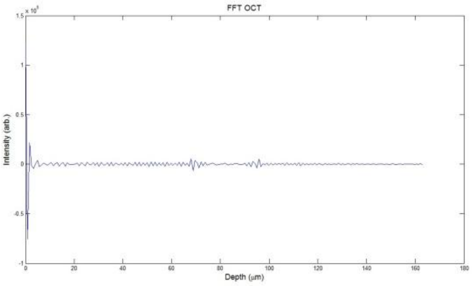

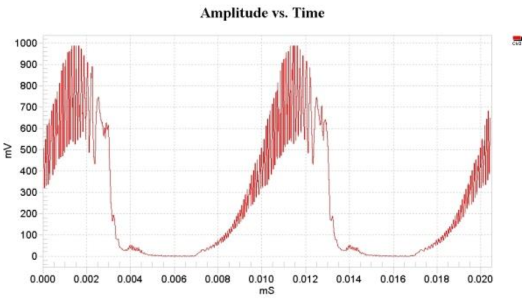
Amplitude vs. Time
mV
0
100
200
300
400
500
600
700
800
900
1000
mS
0.000
0.002
0.004
0.006
0.008
0.010
0.012
0.014
0.016
0.018
0.020

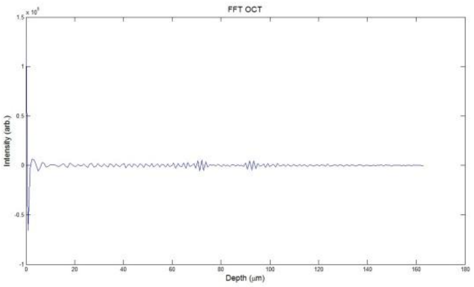
FFT OCT
x 10^5
Intensity (arb.)
1.5
1
0.5
0
-0.5
-1
Depth (μm)
0
20
40
60
80
100
120
140
160
180

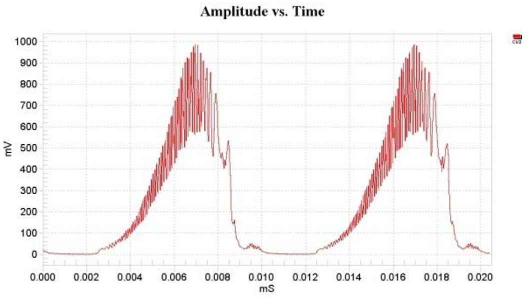
Amplitude vs. Time
mV
0
100
200
300
400
500
600
700
800
900
1000
mS
0.000
0.002
0.004
0.006
0.008
0.010
0.012
0.014
0.016
0.018
0.020

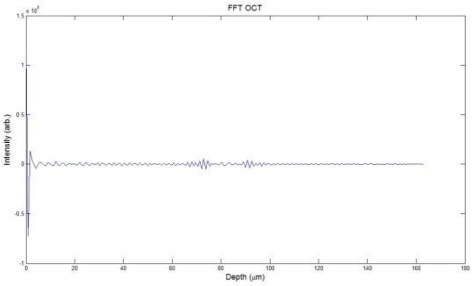
FFT OCT
x 10^5
Intensity (arb.)
1.5
1
0.5
0
-0.5
-1
Depth (μm)
0
20
40
60
80
100
120
140
160
180

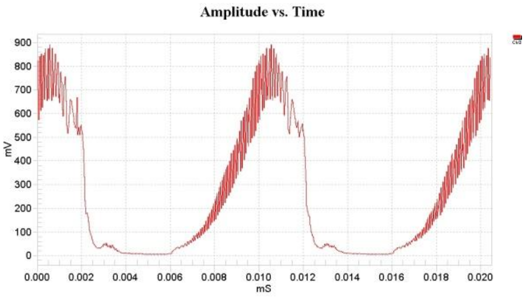
Amplitude vs. Time
mV
0
100
200
300
400
500
600
700
800
900
mS
0.000
0.002
0.004
0.006
0.008
0.010
0.012
0.014
0.016
0.018
0.020

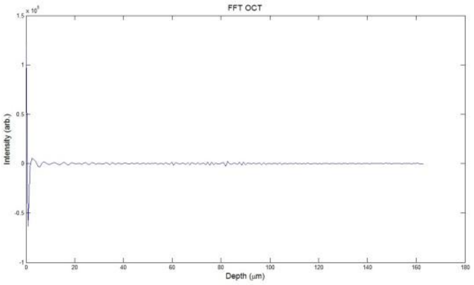
FFT OCT
x 10^5
Intensity (arb.)
1.5
1
0.5
0
-0.5
-1
Depth (μm)
0
20
40
60
80
100
120
140
160
180

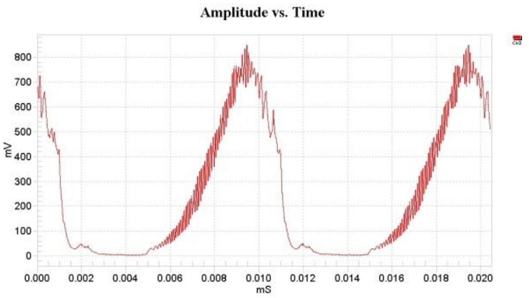
Amplitude vs. Time
mV
0
100
200
300
400
500
600
700
800
mS
0.000
0.002
0.004
0.006
0.008
0.010
0.012
0.014
0.016
0.018
0.020

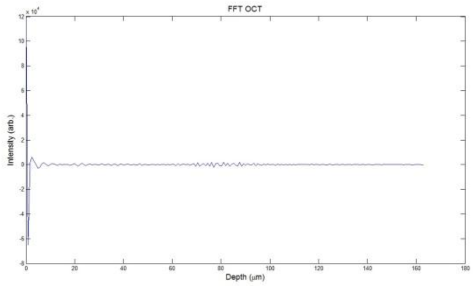
FFT OCT
x 10^4
Intensity (arb.)
12
10
8
6
4
2
0
-2
-4
-6
-8
Depth (μm)
0
20
40
60
80
100
120
140
160
180

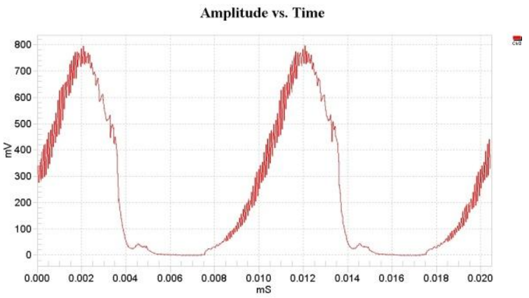
Amplitude vs. Time
mV
0
100
200
300
400
500
600
700
800
mS
0.000
0.002
0.004
0.006
0.008
0.010
0.012
0.014
0.016
0.018
0.020

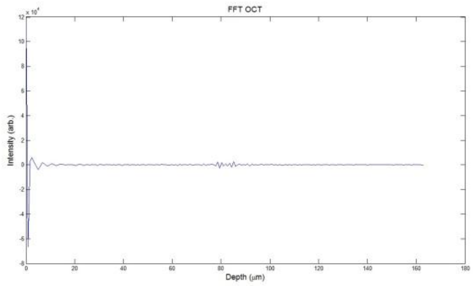
FFT OCT
x 10^4
Intensity (arb.)
12
10
8
6
4
2
0
-2
-4
-6
-8
Depth (μm)
0
20
40
60
80
100
120
140
160
180

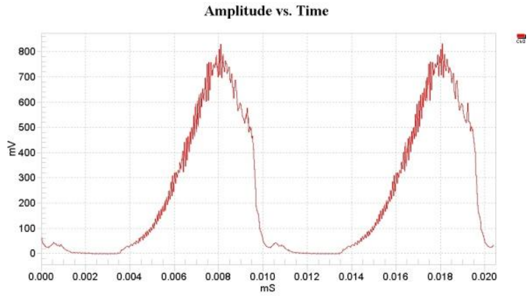
Amplitude vs. Time
mV
800
700
600
500
400
300
200
100
0
0.000 0.002 0.004 0.006 0.008 0.010 0.012 0.014 0.016 0.018 0.020
mS
ChD

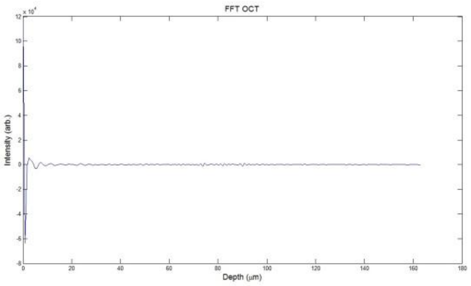
FFT OCT
x 10^4
Intensity (arb.)
12 10 8 6 4 2 0 -2 -4 -6 -8
0 20 40 60 80 100 120 140 160 180
Depth (μm)

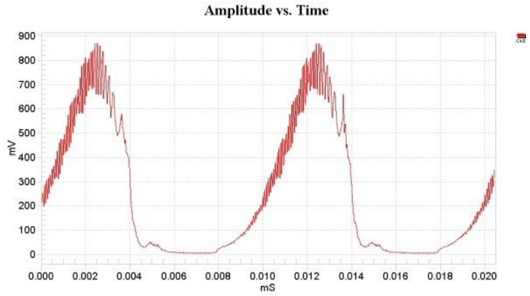
Amplitude vs. Time
mV
900
800
700
600
500
400
300
200
100
0
0.000 0.002 0.004 0.006 0.008 0.010 0.012 0.014 0.016 0.018 0.020
mS
ChD

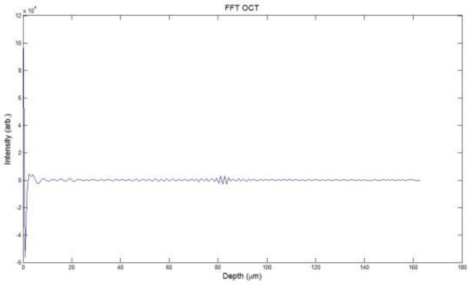
FFT OCT
x 10^4
Intensity (arb.)
12 10 8 6 4 2 0 -2 -4 -6
0 20 40 60 80 100 120 140 160 180
Depth (μm)

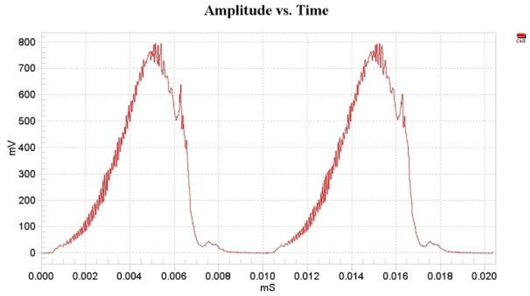
Amplitude vs. Time
mV
800
700
600
500
400
300
200
100
0
0.000 0.002 0.004 0.006 0.008 0.010 0.012 0.014 0.016 0.018 0.020
mS
ChD

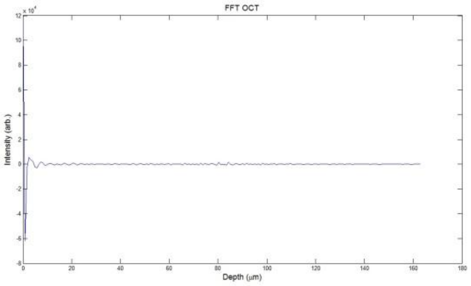
FFT OCT
x 10^4
Intensity (arb.)
12 10 8 6 4 2 0 -2 -4 -6 -8
0 20 40 60 80 100 120 140 160 180
Depth (μm)

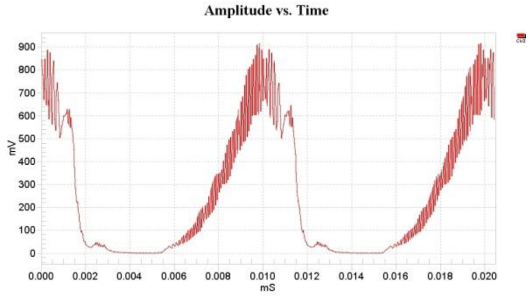
Amplitude vs. Time
mV
900
800
700
600
500
400
300
200
100
0
0.000 0.002 0.004 0.006 0.008 0.010 0.012 0.014 0.016 0.018 0.020
mS
ChD

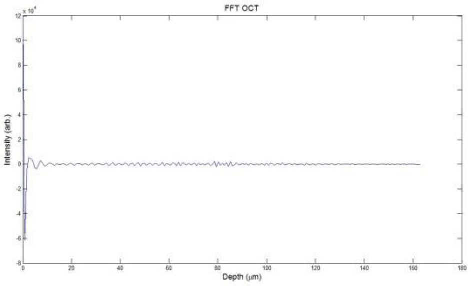
FFT OCT
x 10^4
Intensity (arb.)
12 10 8 6 4 2 0 -2 -4 -6 -8
0 20 40 60 80 100 120 140 160 180
Depth (μm)

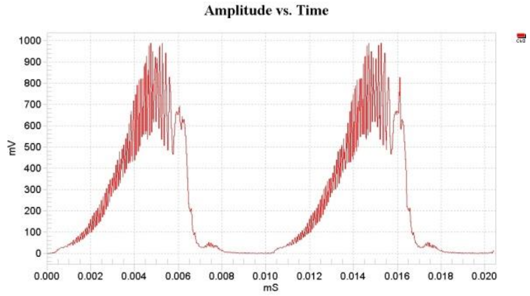
Amplitude vs. Time
mV
1000
900
800
700
600
500
400
300
200
100
0
0.000 0.002 0.004 0.006 0.008 0.010 0.012 0.014 0.016 0.018 0.020
mS
ChD

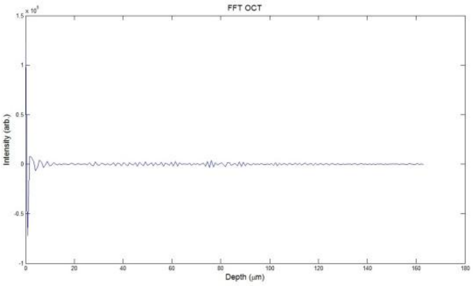
FFT OCT
x 10^5
Intensity (arb.)
1.5 1 0.5 0 -0.5 -1
0 20 40 60 80 100 120 140 160 180
Depth (μm)

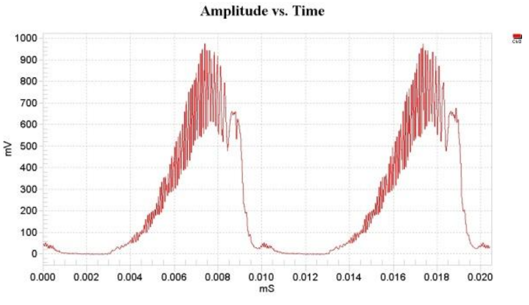
Amplitude vs. Time
mV
1000
900
800
700
600
500
400
300
200
100
0
0.000
0.002
0.004
0.006
0.008
0.010
0.012
0.014
0.016
0.018
0.020
mS

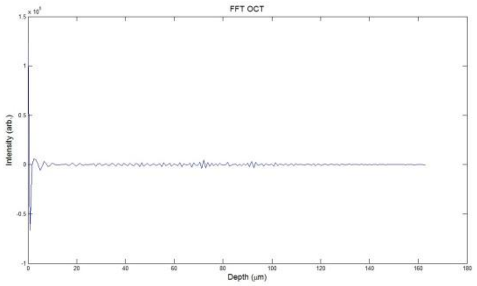
FFT OCT
x 10^5
Intensity (arb.)
1.5
1
0.5
0
-0.5
-1
0
20
40
60
80
100
120
140
160
180
Depth (μm)

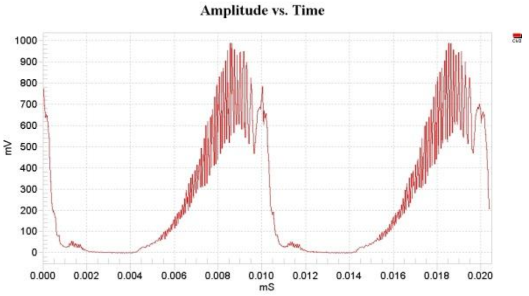
Amplitude vs. Time
mV
1000
900
800
700
600
500
400
300
200
100
0
0.000
0.002
0.004
0.006
0.008
0.010
0.012
0.014
0.016
0.018
0.020
mS

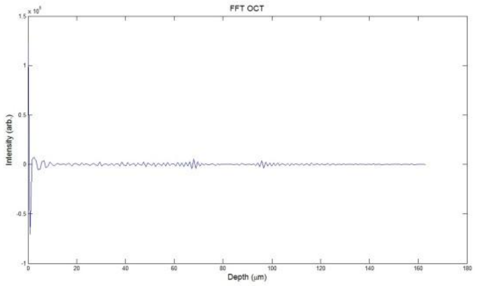
FFT OCT
x 10^5
Intensity (arb.)
1.5
1
0.5
0
-0.5
-1
0
20
40
60
80
100
120
140
160
180
Depth (μm)

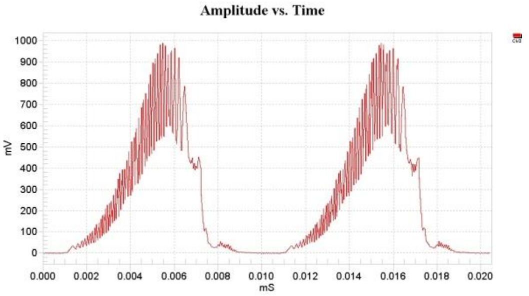
Amplitude vs. Time
mV
1000
900
800
700
600
500
400
300
200
100
0
0.000
0.002
0.004
0.006
0.008
0.010
0.012
0.014
0.016
0.018
0.020
mS

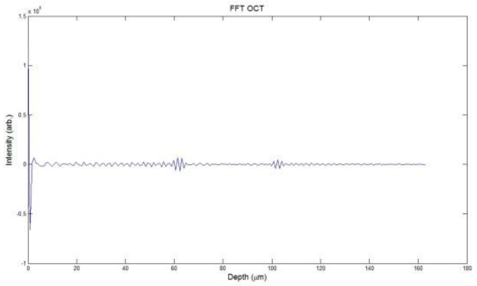
FFT OCT
x 10^5
Intensity (arb.)
1.5
1
0.5
0
-0.5
-1
0
20
40
60
80
100
120
140
160
180
Depth (μm)

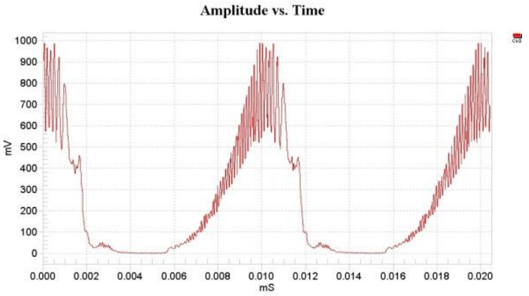
Amplitude vs. Time
mV
1000
900
800
700
600
500
400
300
200
100
0
0.000
0.002
0.004
0.006
0.008
0.010
0.012
0.014
0.016
0.018
0.020
mS

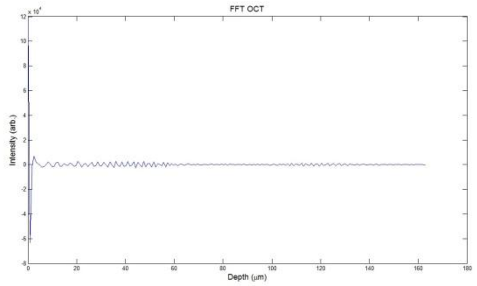
FFT OCT
x 10^4
Intensity (arb.)
12
10
8
6
4
2
0
-2
-4
-6
-8
0
20
40
60
80
100
120
140
160
180
Depth (μm)

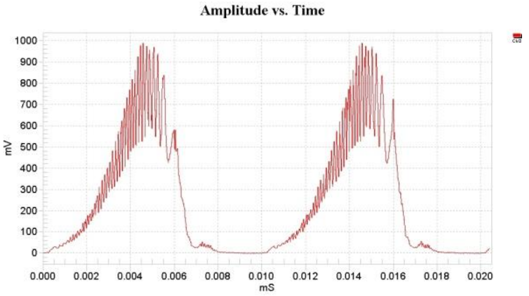
Amplitude vs. Time
mV
1000
900
800
700
600
500
400
300
200
100
0
0.000
0.002
0.004
0.006
0.008
0.010
0.012
0.014
0.016
0.018
0.020
mS

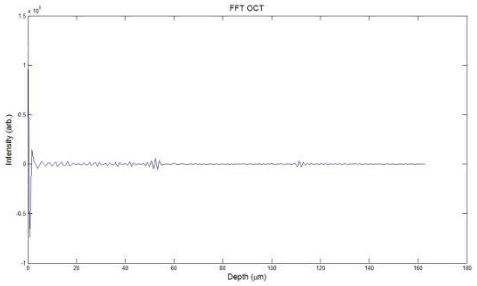
FFT OCT
x 10^5
Intensity (arb.)
1.5
1
0.5
0
-0.5
-1
0
20
40
60
80
100
120
140
160
180
Depth (μm)

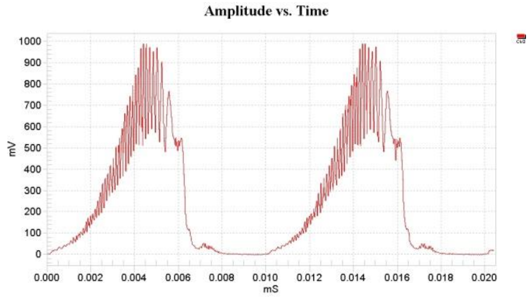
Amplitude vs. Time
mV
1000
900
800
700
600
500
400
300
200
100
0
0.000 0.002 0.004 0.006 0.008 0.010 0.012 0.014 0.016 0.018 0.020
mS

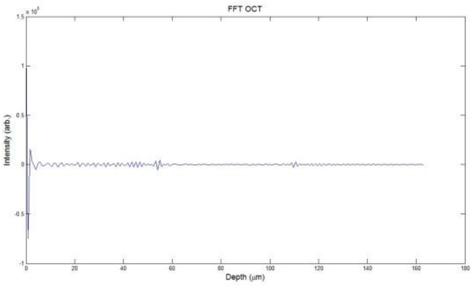
FFT OCT
x 10^5
1.5
1
0.5
0
-0.5
-1
Intensity (arb.)
0 20 40 60 80 100 120 140 160 180
Depth (μm)

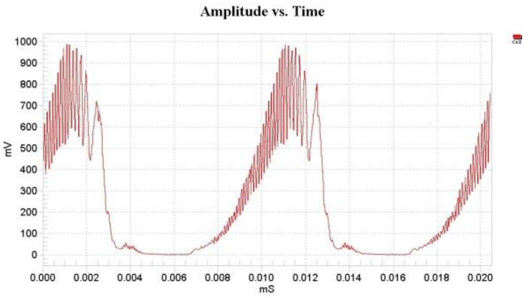
Amplitude vs. Time
mV
1000
900
800
700
600
500
400
300
200
100
0
0.000 0.002 0.004 0.006 0.008 0.010 0.012 0.014 0.016 0.018 0.020
mS

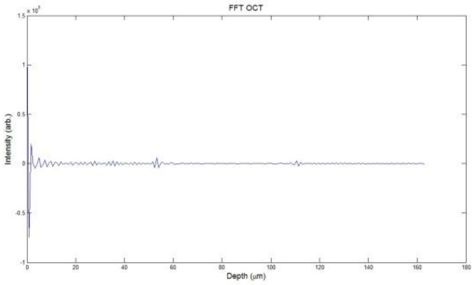
FFT OCT
x 10^5
1.5
1
0.5
0
-0.5
-1
Intensity (arb.)
0 20 40 60 80 100 120 140 160 180
Depth (μm)

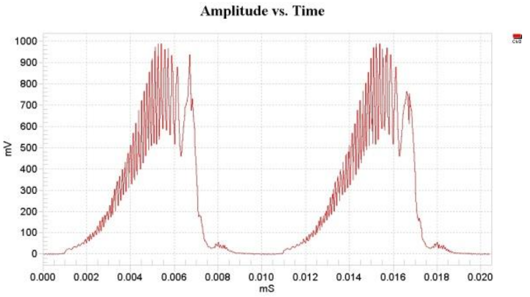
Amplitude vs. Time
mV
1000
900
800
700
600
500
400
300
200
100
0
0.000 0.002 0.004 0.006 0.008 0.010 0.012 0.014 0.016 0.018 0.020
mS

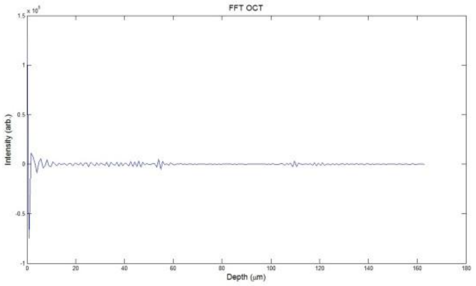
FFT OCT
x 10^5
1.5
1
0.5
0
-0.5
-1
Intensity (arb.)
0 20 40 60 80 100 120 140 160 180
Depth (μm)

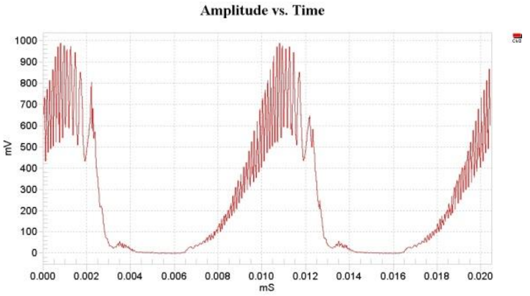
Amplitude vs. Time
mV
1000
900
800
700
600
500
400
300
200
100
0
0.000 0.002 0.004 0.006 0.008 0.010 0.012 0.014 0.016 0.018 0.020
mS

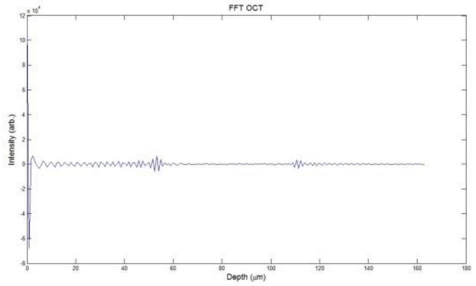
FFT OCT
x 10^4
12
10
8
6
4
2
0
-2
-4
-6
-8
Intensity (arb.)
0 20 40 60 80 100 120 140 160 180
Depth (μm)

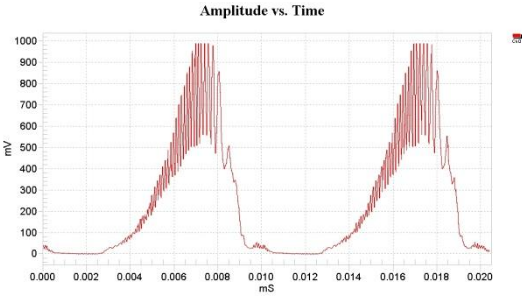
Amplitude vs. Time
mV
1000
900
800
700
600
500
400
300
200
100
0
0.000 0.002 0.004 0.006 0.008 0.010 0.012 0.014 0.016 0.018 0.020
mS

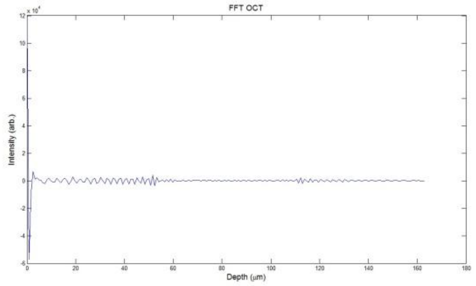
FFT OCT
x 10^4
12
10
8
6
4
2
0
-2
-4
-6
Intensity (arb.)
0 20 40 60 80 100 120 140 160 180
Depth (μm)

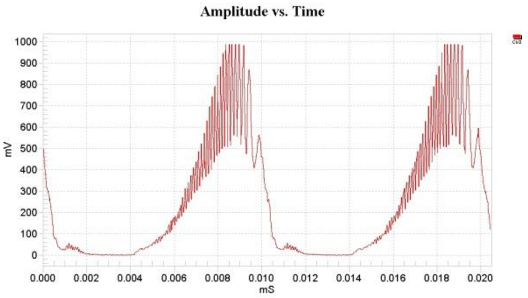
Amplitude vs. Time
mV
1000
900
800
700
600
500
400
300
200
100
0
0.000
0.002
0.004
0.006
0.008
0.010
0.012
0.014
0.016
0.018
0.020
mS

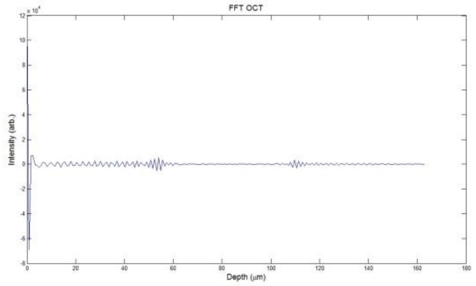
FFT OCT
x 10⁴
Intensity (arb.)
12
10
8
6
4
2
0
-2
-4
-6
-8
0
20
40
60
80
100
120
140
160
180
Depth (μm)

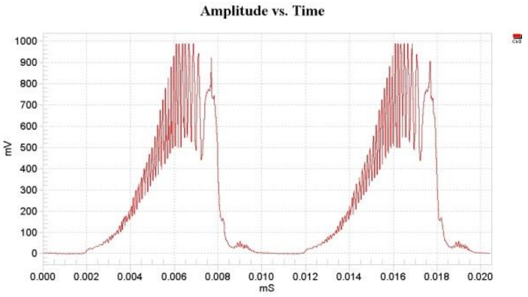
Amplitude vs. Time
mV
1000
900
800
700
600
500
400
300
200
100
0
0.000
0.002
0.004
0.006
0.008
0.010
0.012
0.014
0.016
0.018
0.020
mS

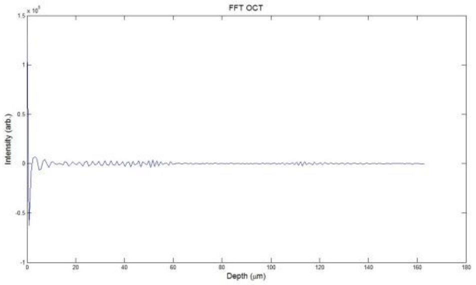
FFT OCT
x 10⁵
Intensity (arb.)
1.5
1
0.5
0
-0.5
-1
0
20
40
60
80
100
120
140
160
180
Depth (μm)

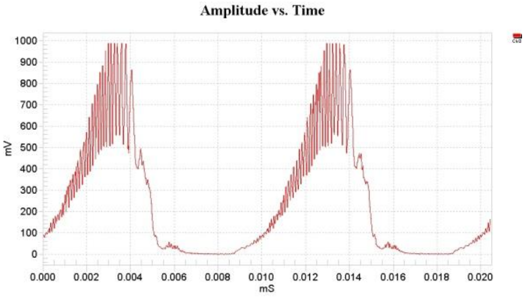
Amplitude vs. Time
mV
1000
900
800
700
600
500
400
300
200
100
0
0.000
0.002
0.004
0.006
0.008
0.010
0.012
0.014
0.016
0.018
0.020
mS

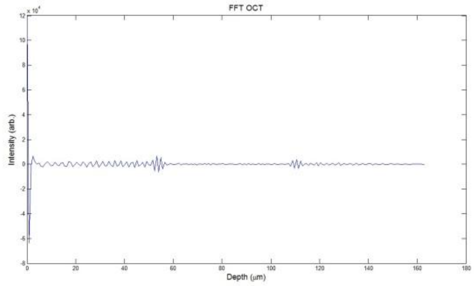
FFT OCT
x 10⁴
Intensity (arb.)
12
10
8
6
4
2
0
-2
-4
-6
-8
0
20
40
60
80
100
120
140
160
180
Depth (μm)

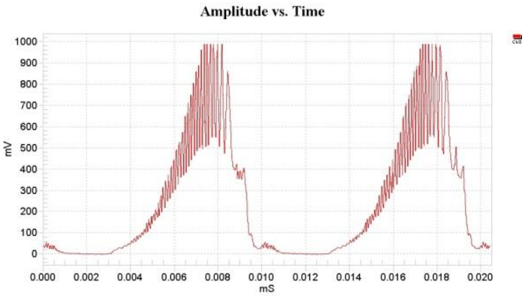
Amplitude vs. Time
mV
1000
900
800
700
600
500
400
300
200
100
0
0.000
0.002
0.004
0.006
0.008
0.010
0.012
0.014
0.016
0.018
0.020
mS

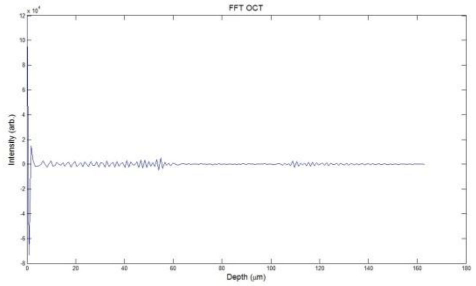
FFT OCT
x 10⁴
Intensity (arb.)
12
10
8
6
4
2
0
-2
-4
-6
-8
0
20
40
60
80
100
120
140
160
180
Depth (μm)